The two-dimensional Ising spin glass at zero temperature

Dissertation

zur Erlangung des Grades

"Doktor der Naturwissenschaften"

am Fachbereich Physik, Mathematik und Informatik

der Johannes Gutenberg-Universität Mainz

vorgelegt von

Hamid Khoshbakht

geboren in Isfahan, Iran

Mainz im February 2019

Parts of this thesis have already been published in:

M. Weigel and H. Khoshbakht
High-precision studies of domain-wall properties in the 2D Gaussian Ising spin glass
Submitted to Journal of Physics: Conference Series (2018).

H. Khoshbakht and M. Weigel
Domain-wall excitations in the two-dimensional Ising spin glass
Phys. Rev. B, **97**, 064410 (2018).
This paper has been selected by editors of PRB to be an "**Editors' Suggestion**".

To **Hazrat Salaheddin Dr. Hossein Assarian**
who encouraged me to study Physics

and

To the curiosity of the little boy
who wondered why huge ships don't sink
when they're made of Iron!

Declaration of authorship

I hereby declare that I wrote the dissertation submitted without any unauthorized external assistance and used only sources acknowledged in the work. All textual passages which are appropriated verbatim or paraphrased from published and unpublished texts as well as all information obtained from oral sources are duly indicated and listed in accordance with bibliographical rules. In carrying out this research, I complied with the rules of standard scientific practice as formulated in the statutes of Johannes Gutenberg University Mainz to insure standard scientific practice.

Hamid Khoshbakht

Abstract

This thesis reports on a study of the Ising spin glass in two dimensions. Since the critical temperature for this system in known to be zero, only ground-state calculations are considered. Ground states for the Ising spin glass in two dimensions can be determined in polynomial time by a recently proposed mapping to an auxiliary graph decorated with Kasteleyn cities, as long as periodic boundary conditions are applied at most in one direction. Using this method, ground states for systems with open-periodic boundary conditions for lattices of linear sizes up to $L = 10\,000$ have been determined, and defect energies as well as domain-wall lengths have been calculated. A new algorithm based on a combination of the matching approach and a windowing technique is proposed, and quasi-exact ground-states for lattices with periodic-periodic boundary conditions up to $L = 3000$ are determined. The run-time of this windowing algorithm is also polynomial. By using these techniques, high-precision estimates of the spin-stiffness exponent and the domain-wall fractal dimension for Gaussian couplings have been achieved.

The 2D Ising spin glass with bimodal couplings has a multitude of degenerate ground states, with the number of degenerate states growing exponentially with increasing system size. It is hence necessary to develop techniques for sampling the ground-state manifold uniformly. A new efficient algorithm serving this purpose is presented. The algorithm is based on an exact analysis of clusters of free spins in a disorder configuration and a subsequent sampling step based on parallel tempering Monte Carlo. Using this algorithm together with the mapping approach, high-precision estimates of the spin-stiffness exponent and the domain-wall fractal dimension for bimodal couplings are obtained. The estimates of the spin-stiffness exponent and the domain-wall fractal dimension for both Gaussian and bimodal couplings are the most accurate estimates which have been reported to date.

The geometry of the domain walls of both Gaussian and bimodal couplings is compared to the detailed predictions given for random curves in the plane in the framework of Schramm-Loewner Evolution (SLE). Different boundary conditions are considered, and for each case the fractal dimension and the SLE diffusion constant of the corresponding Brownian motion are calculated. Correlations

between different domain-wall segments are explicitly checked by testing for independence of the increments of the Loewner driving function.

Contents

Chapter 1

Introduction to spin-glass systems

1.1 Why do we study spin glasses?

Magnetic materials have been known since ancient times when people observed that a piece of lodestone could attract iron. Over the last two centuries, magnetic materials (and magnetism in general) have been widely studied. Nowadays magnetic materials have found very wide applications in electronics, computers, detectors, storage devices, etc. Despite the fact that the origin of magnetism is well understood, namely as a collective behavior of magnetic moments or *spins* of the atoms, many aspects of spin systems still remain a challenge for condensed-matter physics. We know that in a system of magnetic atoms the magnetic state depends on temperature. At high temperatures, spins have random orientations due to thermal fluctuations and the system is in a paramagnetic phase. By decreasing the temperature of the system, thermal fluctuations become less important and at a specific value called *critical temperature*, the interactions between spins overcome thermal fluctuations and long-range order will appear in the system. However many real-life spin systems do not only contain magnetic atoms, but both magnetic and non-magnetic atoms exist in the system in a random, disordered fashion. Sometimes the combination of magnetic atoms and the randomness of non-magnetic atoms (disorder) results in a new type of magnetic structure such as *spin glass*.

Spin glasses have many unique features. As an example, by cooling down a spin-glass system spin orientations start freezing below the critical temperature and a phase transition from paramagnetic to spin-glass phase will occur where the number of up and down spins is still the same (as in the paramagnetic phase), but there are some correlations in the spin-glass phase which do not exist in the paramagnetic one. Although suggested models for spin glasses are usually described by simple Hamiltonians, nevertheless the study of such systems is

challenging and sometimes there is no adequate description for the behavior of spin-glass systems.

The problem of an adequate description and understanding of the behavior of spin systems with disorder has been studied for at least forty years by a large number of scientists in statistical and condensed matter physics as well as, increasingly, researchers in adjacent fields such as computer science and mathematics [1]. Spin glasses can be described by simple Hamiltonians on simple lattice structures, where neighbors and the interactions between the neighbors do not change with time, and yet they can capture many aspects of non-trivial characteristics of the spin-glass phase [2]. In addition to that, understanding the physics behind the properties of spin-glass systems is related to fundamental questions in statistical mechanics [3] and helps us to understand the behavior of many magnetic and non-magnetic disordered systems such as ordinary and structural glasses, amorphous alloys, and even systems beyond the scope of physics, for instance error correcting codes, polymer chemistry, biophysics and neural networks [4].

1.2 What is a spin glass?

Spin glasses are systems in which the interaction between the magnetic moments of the system are "in contrast" with each other due to some "quenched" structural disorder [3]. The term *quenched* disorder means that the interactions between magnetic moments are frozen and do not change with time. The conflict between the interactions of the system results in *frustration* in spin glasses which means that when we try to minimize the energy of the system not all the interactions can be "satisfied" (to be in the lowest energy level), and hence some of them are "frustrated" (see Fig. 1.1). The term *spin glass* was first used by P. W. Anderson in 1970 in analogy with structural glasses to emphasize the existence of a new low-temperature phase with unidentified order [5]. The new phase does not have any long-range order of either ferromagnetic or antiferromagnetic type, but the system shows a freezing transition to a state with a new kind of order in which the spins are aligned in random directions [3]. In simple words, spin-glass phase refers to a phase where some form of magnetic order is present, but no long-range order as it is found in ferromagnets and antiferromagnets.

Soon after the discovery of spin glasses, it was realized that quenched disorder and frustration are two essential elements leading to the strange behavior of spin glasses. A simple mathematical model for spin glasses was introduced by S. F. Edwards and P. W. Anderson in 1975 [6] to describe the behavior of these systems, known as the Edwards-Anderson (EA) model. Although the EA model can be considered as one of the simplest models for spin glasses, yet, it is not fully

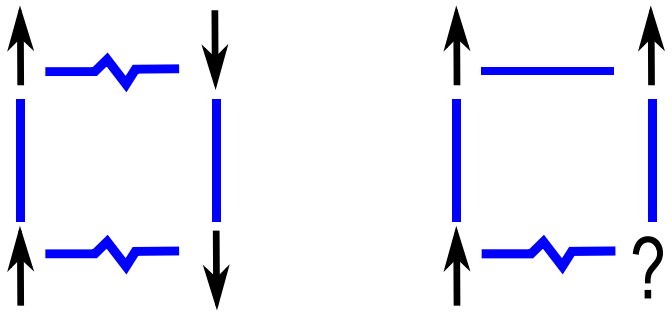

Figure 1.1: Schematic view of unfrustrated (left panel) and frustrated (right panel) systems. Arrows represent spins, straight lines are ferromagnetic interactions, and antiferromagnetic bonds are shown by broken lines. In frustrated systems not all the interactions can be satisfied.

understood. There is still no analytical solution for this model and the knowledge about the existence of a finite-temperature phase transition relies entirely on numerical simulations [7, 8, 9, 10, 11, 12, 13, 14, 15, 16, 17, 18, 19, 20, 21, 22, 23, 24, 25]. This thesis is also focused on studying the EA model numerically, and we try to answer some debated questions of this model by developing two new algorithms presented in subsequent chapters.

1.3 The Edwards-Anderson model

According to the Edwards and Anderson model [6], spin-glass systems are considered as a lattice (graph) which has N sites and each site i of the system contains a magnetic moment with spin S_i. The interaction (coupling) between S_i and S_j (spins at sites i and j) is J_{ij} and the Hamiltonian of the system in the presence of an external magnetic field H can be generally written as

$$\mathcal{H}(\{\boldsymbol{s}\},\{J_{ij}\}) = -\sum_{(i,j)} J_{ij} S_i S_j - H \sum S_i \tag{1.3.1}$$

where $\sum_{(i,j)}$ means the sum over all the interactions of the system, i.e., all edges of the graph and $\{\boldsymbol{s}\}$ represents the spin configuration of the system. The interactions J_{ij} are independent random variables and they can be both ferromagnetic (positive) and antiferromagnetic (negative). The two essential ingredients of spin glasses can be seen in this model:

- *Quenched disorder*: the disorder in spin glasses has been considered in the Hamiltonian of the EA model by means of constant random couplings J_{ij}. The value of any observable of the system $\mathcal{O}(J)$ depends on the distribution and the realization of J. Therefore in order to find the expectation value

of the observable, one needs to take an average over the distribution of the disorder J.

- *Frustration*: the frustration in spin-glass systems in the EA model is due to the fact that the couplings of the system can be both positive and negative. In this case, when we try to minimize the energy of a configuration, it is not possible to satisfy all the spins, thus some of them have to take the undesired orientations.

The variations of the EA model mainly differ in the form of the coupling distribution $P(J_{ij})$. For instance, the couplings J_{ij} can be continuous or discrete random variables. Two typical examples of $P(J_{ij})$ are the *Gaussian* distribution with

$$P(J_{ij}) = \frac{1}{\sqrt{2\pi J^2}} \exp\left(\frac{-(J_{ij}-J_0)^2}{2J^2}\right), \tag{1.3.2}$$

for continuous couplings and the *bimodal* distribution

$$P(J_{ij}) = p\delta(J_{ij}-J) + (1-p)\delta(J_{ij}+J), \tag{1.3.3}$$

resulting in discrete couplings. Equation (1.3.2) is a Gaussian distribution with mean J_0 and variance J^2, while J_{ij} in (1.3.3) can be either J with probability p or $-J$ with probability $1-p$. The value of p in the bimodal model determines the amount of frustration in the system. For example, $p = 1$ (0) refers to the pure ferromagnetic (antiferromagnetic) phase where there is no frustration in the system and when $p = 0.5$ the amount of frustration in the system is maximized. Since J_{ij} can be only $+J$ or $-J$ in the bimodal case, this is also known as $\pm J$ *model*.

The EA model is often considered in the context of Ising spin variables in which the value of S_i can be only $+1$ or -1, in other words the orientation of spins can be either up or down. The graph is usually considered as a d-dimensional cubic lattice, and only nearest-neighbor interactions are taken into account. There are, however, some other models with Hamiltonians similar to the one in the EA model (1.3.1) but with different choices of spins or the lattice structure. For example, the model with vector spin variables has a Hamiltonian of the form

$$\mathcal{H} = -\sum_{(i,j)} J_{ij} \boldsymbol{S}_i \cdot \boldsymbol{S}_j \tag{1.3.4}$$

in which $\boldsymbol{S}_i$ is a vector under the constraint $\boldsymbol{S}^2 = 1$ and $\boldsymbol{S}_i \cdot \boldsymbol{S}_j$ denotes the scalar product between the spins on different sites. The vector spin with two or three components are called the XY and Heisenberg Edwards-Anderson models, respectively, and in general the vector spin with n component is known as the $O(n)$ model. (see Refs. [26, 27, 28, 29, 30, 31, 32, 33] for example). There is another

special case of the EA model introduced by S. Kirkpatrick and D. Sherrington in 1975 [34] known as the SK model in which the underlying lattice is a complete graph and the couplings J_{ij} are defined for all possible pairs of sites [35]. Therefore the SK model may be regarded as the EA model in the limit of infinite spatial dimension. The SK model is the basis for mean-field theory of spin-glass systems. The mean-field model has been solved completely and its solution provides great insight into the nature of the spin-glass phase [36].

1.4 Statistical mechanics and phase transitions

The goal of statistical mechanics is to obtain macroscopic properties of many-particle systems by starting from the interactions between the microscopic elements of the system. One of the macroscopic properties of a system is the phase of the system which depends on internal interactions between the particles as well as external conditions such as temperature and pressure. As a simple example, the microscopic elements of vapor, water and ice are H_2O molecules but according to the interactions between the molecules and the temperature and pressure of the system, H_2O can be found in gas, liquid or solid phase. In this section, we want to review some of the methods of statistical mechanics to describe the common features of phase transitions, especially in magnetic systems.

Let us consider a magnetic system of N magnetic moments at different sites of a lattice where the spin of the particle at site i is S_i and the interaction between site i and j is described as J_{ij}. In the canonical ensemble, the probability of finding the system in a particular spin configuration depends on the energy of the configuration as

$$P(\boldsymbol{s}) \propto e^{-\beta \mathcal{H}(\boldsymbol{s})}, \tag{1.4.1}$$

where the Hamiltonian of the system $\mathcal{H}$ in the EA model is described by (1.3.1), $\boldsymbol{s} = \{S_i\}$ represents the spin configuration of the system, and $e^{-\beta\mathcal{H}}$ is known as the *Boltzmann factor*. The normalization constant can be written as

$$\mathcal{Z} = \sum_{S_1} \sum_{S_2} \cdots \sum_{S_N} e^{-\beta\mathcal{H}} = \sum_{\boldsymbol{s}} e^{-\beta\mathcal{H}}, \tag{1.4.2}$$

and it is called the *partition function* of the system. Thus, the probability distribution of the system will be

$$P(\boldsymbol{s}) = \frac{e^{-\beta\mathcal{H}}}{\mathcal{Z}}, \tag{1.4.3}$$

known as *Gibbs-Boltzmann distribution*, and the general prescription of statistical mechanics is to calculate the thermal average of a physical observable using $P(\boldsymbol{s})$ in (1.4.3).

The partition function $\mathcal{Z}$ plays an important role in statistical mechanics as a tool to calculate thermodynamic quantities. For instance, the internal energy U, the entropy S and the Helmholtz free energy F in thermodynamics can be calculated as

$$\begin{aligned} U &= \langle E \rangle_{\text{th}} = \frac{1}{\mathcal{Z}} \sum_i E_i e^{-\beta \mathcal{H}(\boldsymbol{s}_i)} = -\frac{\partial}{\partial \beta} \ln \mathcal{Z}, \\ S &= k_{\text{B}} \ln \mathcal{Z} + \frac{U}{T}, \\ F &= -k_{\text{B}} T \ln \mathcal{Z}, \end{aligned} \tag{1.4.4}$$

where the sum in the expression for the internal energy runs over all microstates of the system and E_i is the energy of each microstate. In order to identify the phase of the system we need to consider a measure of changes to characterize the macroscopic properties of the system, i.e., the *order parameter*. One of the common order parameters in magnetic systems is the *magnetization* defined by

$$m = \frac{1}{N} \left\langle \sum_{i=1}^{N} S_i \right\rangle_{\text{th}}, \tag{1.4.5}$$

where $\langle \cdots \rangle_{\text{th}}$ denotes the expectation value (thermal average). Note that at this point we do not consider any disorder average. To see how the order parameter can be used, let us consider an Ising ferromagnetic system as an example. The Gibbs-Boltzmann distribution suggests that at low temperatures ($\beta \gg 1$) the probability of finding the system in low-energy spin configurations is much higher than high-energy states, because the probability decreases exponentially by increasing the energy. Therefore almost all the spins are parallel and the magnetization m is very close to 1. By increasing the temperature, the value of β decreases and the states with different energies would have similar probabilities due to the value of β being small ($\beta \ll 1$). This allows some of the spins to have different orientations and as the result, the value of m starts decreasing from 1. At a certain temperature T_c (the critical temperature) the thermal fluctuations destroy the ordered state and the magnetization m vanishes. This example shows how the existence of a critical temperature T_c and a phase transition from the ferromagnetic state where $m \neq 0$ for $T < T_c$ to the paramagnetic phase with $m = 0$ for $T > T_c$ can be predicted using the distribution (1.4.3) together with the magnetization m as the order parameter.

Although the magnetization can be considered as an order parameter for the phase transition between paramagnetic and ferromagnetic states, it is not an order parameter for spin-glass systems as it almost vanishes for both paramagnetic and spin-glass phases. Therefore other order parameters must be defined for

spin-glass systems. For instance, the spin-glass order parameter can be taken as

$$q = \left\langle \langle S_i \rangle_{\text{th}}^2 \right\rangle_J, \tag{1.4.6}$$

known as the Edward-Anderson order parameter where, as usual, $\langle \cdots \rangle_{\text{th}}$ means thermal average and $\langle \cdots \rangle_J$ denotes an average over disorders. Since the spins at the same distance from S_i can be either ferromagnetically or antiferromagnetically correlated, then people often consider another order parameter called *susceptibility* defined as

$$\chi = \frac{1}{N} \sum_{<i,j>} \left\langle \langle S_i S_j \rangle_{\text{th}}^2 \right\rangle_J, \tag{1.4.7}$$

which diverges at the critical temperature. One can also investigate how individual terms in the sum in Eq. (1.4.7) vary with the distance r_{ij} between S_i and S_j by defining

$$\Gamma(r_{ij}) = \left\langle \langle S_i S_j \rangle_{\text{th}}^2 \right\rangle_J \tag{1.4.8}$$

and then if

$$\Gamma(r_{ij}) \propto e^{-r_{ij}/\xi}, \tag{1.4.9}$$

one can extract the correlation length ξ, which should also diverge at the critical temperature [37]. We will discuss the behavior of the spin-glass susceptibility and spin-glass correlation at the critical temperature later.

1.5 Critical exponents and finite-size scaling

The value of the order parameters above and below the critical temperature are usually known. For example, for paramagnetic materials we know that $m = 0$ at high temperatures ($T > T_c$) and when $T \to 0$ then $m \to \pm 1$. But how do the order parameters behave close to the critical temperature when $T \to T_c$?

In the context of critical phenomena, if the first derivative of the free energy shows a sudden change at the critical temperature this defines a *first-order phase transition*, while if the first derivative of the free energy changes continuously across the critical point then the system experiences a *second-order phase transition*. In the case of the second order phase transitions one can consider the observables of the system obey power laws known as the *scaling laws* such that

$$\begin{aligned} q &\propto |T - T_c|^{-\beta}, \\ \chi &\propto |T - T_c|^{-\gamma}, \\ \xi &\propto |T - T_c|^{-\nu}, \end{aligned} \tag{1.5.1}$$

in which β, γ and ν are *critical exponents* defined in the vicinity of a critical temperature T_c. The critical exponents for spin-glass systems have been determined both experimentally and numerically [38].

In the theory of phase transitions, scientists always consider the thermodynamic limit where $N \to \infty$, because only in this limit the boundaries of the system become meaningless and would have no effect on the behaviour of the system, i.e., only this limit actually has a phase transition. However in practice, especially in numerical simulations, the thermodynamic limit is not achievable, as in experimental studies $10^{23} \neq \infty$ and in simulations we usually consider a system of linear size L and the number of particles $N = L^d \neq \infty$ where d is the space dimension. Since the critical temperature T_c is defined in the thermodynamic limit, then the scaling laws (1.5.1) are not directly applicable to the finite-size systems. In a finite system, the correlation length ξ can not diverge to infinity as it is restricted to the dimensions of the system. As a rough estimate, let us assume that close to the critical temperature

$$\xi \approx \xi_0 |T - T_c|^{-2/3}, \tag{1.5.2}$$

where ξ_0 is the correlation length of the system very far from the critical temperature[1]. This choice of ξ is realistic for magnetic systems, and ξ_0 is usually of the order of the distance between the particles of the system, i.e., Å. If we imagine that $\xi_0 \approx 10\,\text{Å}$ (which is an overestimate almost in any case according to Ref. [40]) and we have a sample of size $L = 1$ cm in the lab, then we find $\xi \approx L$ when $|T - T_c| \approx 10^{-11}$. Therefore the finite-size effects are usually hard to observe in experiments [40]. However in numerical studies, where N is of the order of a few hundreds, the finite-size effects become more important. In order to consider these effects, imagine that we have a system of linear size L at a temperature T above the critical temperature. By decreasing the temperature, the correlation length of the system starts growing until it reaches a value like ξ^* of the order of L in which an apparent phase transition occurs at a temperature $T_c(L) \geq T_c(\infty) (= T_c)$. By considering $\xi = L$ in (1.5.1) we can find that

$$T_c(L) \propto T_c(\infty) + aL^{1/\nu}, \tag{1.5.3}$$

in which a is a constant that does not depend on the system size or the temperature[2]. Equation (1.5.3) indicates that the critical temperature in a finite-size system depends on the size of the system, and therefore to determine the actual critical temperature we need to take the limit $L \to \infty$.

[1] This estimate is based on the results of ν for some models in three dimensions. For instance, $\nu \approx 0.63$ for the 3D Ising model, $\nu \approx 0.66$ for the 3D XY model, and $\nu \approx 0.7$ for the 3D Heisenberg model. A complete review of the theoretical, numerical and experimental results for ν as well as other critical exponents for various models can be found in Ref. [39].

[2] ξ is the correlation length of the system while ξ^* is the value of the correlation length at the apparent critical temperature $T_c(L)$.

Now we can define the dimensionless correlation length $\xi(T,L)/L$ as a distance to the phase transition for a given system size L, and for any value of L when $T \to T_c(L)$ we can say that

$$\xi(T,L)/L \to \xi^*(T,L)/L. \tag{1.5.4}$$

Therefore according to (1.5.1), the dimensionless correlation length scales as

$$\frac{\xi(T,L)}{L} \propto \frac{1}{L|T-T_c|^\nu} = \frac{1}{[L^{1/\nu}|T-T_c|]^\nu}, \tag{1.5.5}$$

and one can conclude that for finite systems of size L the quantity $L^{1/\nu}|T-T_c|$ should be considered as the proper scaling variable instead of only $|T-T_c|$. Considering the scaling variable for the observables of the system to be $L^{1/\nu}|T-T_c|$ rather than $|T-T_c|$ in (1.5.1) we get

$$q(T,L) \propto L^{\beta/\nu} \frac{1}{[L^{1/\nu}|T-T_c|]^\beta}, \tag{1.5.6}$$

and

$$\chi(T,L) \propto L^{\gamma/\nu} \frac{1}{[L^{1/\nu}|T-T_c|]^\gamma}. \tag{1.5.7}$$

This type of analysis is known as *finite-size scaling technique* (FSS) and enables us to determine the properties of the finite systems if they were in the thermodynamic limit by using L as a scaling variable. Finite-size scaling was first proposed by M.E. Fisher and M. N. Barber in 1972 [41], then it was developed by K. Binder [42, 43] and it is widely used to investigate phase transitions in computational studies. The application of finite-size scaling in spin-glass systems can be found, for instance, in Refs. [3, 16, 22, 44, 45, 31, 46, 47, 48, 49, 50, 51, 52, 53].

Apart from the critical exponents β, γ and ν defined above, we can define three more critical exponents which are relevant in magnetic systems in general as follows: the specific heat at constant magnetic field $C_h(T)$ near the critical temperature diverges as

$$C_h(T) \propto |T-T_c|^\alpha, \tag{1.5.8}$$

the two-points correlation function $\langle S_{i+r}S_i\rangle$ decays as

$$\langle S_{i+r}S_i\rangle \sim |r|^{-(d-2+\eta)} \quad \text{when} \quad |r| \to \infty, \tag{1.5.9}$$

where η is known as *the anomalous dimension*, while the magnetization at the critical point $T = T_c$ for small magnetic field h behaves as

$$m(T=T_c,h) \sim |h|^{1/\delta}. \tag{1.5.10}$$

The six critical exponents can fully identify the type of phase transition and they are constrained by a set of four independent scaling relations

$$\begin{aligned} \alpha + 2\beta + \gamma &= 2, \\ \alpha + \beta(1+\delta) &= 2, \\ \nu(2-\eta) &= \gamma, \\ 2 - \alpha &= \nu d, \end{aligned} \tag{1.5.11}$$

where d is the dimension of the system [2]. Therefore there would be only two independent critical exponents. The fourth identity of Eq. (1.5.11) is called *hyperscaling relation*, and it is valid only below the upper critical dimension. According to the hyperscaling relation the critical exponents as well as the universality class depend on the dimension d of the system [2].

1.6 The two pictures

In oder to investigate the properties of spin glasses, different hypotheses and numerical techniques have been developed. These hypotheses are often called *pictures*. Most of the pictures are asymptotic theories which are supposed to be correct for large systems. Different pictures are known to be able to describe some properties of spin glasses but fail to explain some other properties of these systems. Among various pictures, the most frequently mentioned pictures in literature are *replica symmetry breaking* and the *droplet picture*. There has been an active debate over years concerning which picture can be applied for real spin-glass magnets, and the debate is still going on [54, 55]. Describing the two pictures in full technical detail would need much more space than we can afford here, and therefore in this section we will only intend to convey the main idea of each picture together with some physical aspects, without going deeply into mathematical calculations. The complete description of the two pictures can be found in a number of text books and articles, for instance in Refs. [56, 3, 55, 54, 1, 57, 4].

1.6.1 Replica Symmetry Breaking (RSB)

The replica symmetry breaking is known to be the exact solution of the mean-field spin glass [1] proposed by Parisi in 1979 [58]. In general, replica calculations are based on the following mathematical formula

$$\langle \ln \mathcal{Z} \rangle_J = \lim_{n \to 0} \frac{1}{n} \ln \langle \mathcal{Z}^n \rangle_J \,, \tag{1.6.1}$$

called the replica trick which simplifies the calculation of the free energy of the system. In order to understand the role of the above formula, let us consider the

SK model (in the absence of an external magnetic field) with Hamiltonian

$$\mathcal{H} = \mathcal{H}(\boldsymbol{s}, J) = -\sum_{(i,j)} S_i S_j J_{ij}, \tag{1.6.2}$$

where the sum $\sum_{(i,j)}$ runs over all pairs of spins, J_{ij} are random quenched couplings obeying (1.3.2), and $\boldsymbol{s}$ represents the spin configuration of the system. According to Eq. (1.4.4) the free energy can be written as

$$F = F(J) = -k_{\mathrm{B}} T \ln \mathcal{Z} = -k_{\mathrm{B}} T \ln \sum_{\boldsymbol{s}} e^{-\beta \mathcal{H}(\boldsymbol{s}, J)}. \tag{1.6.3}$$

This expression seems to have a fundamental problem because it suggests that the free energy of spin glasses depends on the disorder realization J, while we know that the free energy is a self-averaging quantity [59] and it should not depend on J for sufficiently large systems. Since the average over the disorder of self-averaging quantities is equal to their J-independent value, therefore what we actually need to do is to calculate the average of the free energy over the disorder. To do that, we should compute the following

$$F = -k_{\mathrm{B}} T \langle \ln \mathcal{Z} \rangle_J = -k_{\mathrm{B}} T \int dJ P(J) \ln \sum_{\boldsymbol{s}} e^{-\beta \mathcal{H}(\boldsymbol{s}, J)}, \tag{1.6.4}$$

which seems to be pretty hard, because we have to integrate logarithm over J. This is the place where the formula (1.6.1) comes in handy and helps us to calculate the average of the free energy by computing the right-hand side of (1.6.1) rather than the left-hand side. Computing the r.h.s. of Eq. (1.6.1) would be much simpler because if we consider n to be an integer, then we can write

$$\langle \mathcal{Z}^n \rangle_J = \sum_{\boldsymbol{s}_1} \cdots \sum_{\boldsymbol{s}_n} \langle e^{-\beta \mathcal{H}(\boldsymbol{s}_1, J) \cdots - \beta \mathcal{H}(\boldsymbol{s}_n, J)} \rangle_J, \tag{1.6.5}$$

where all the Hamiltonians have the same disorder realization. Therefore what we need to do is to consider n replicas of the system and calculate everything as a function of n. Then we have to take the limit $n \to 0$ [57]. Sherrington and Kirkpatrick used this method [34] in which the order parameter was taken as the overlap between two replicas identified with indices α and β defined as

$$q_{\alpha\beta} = \frac{1}{N} \sum_{i=1}^{N} S_i^{\alpha} S_i^{\beta}. \tag{1.6.6}$$

They found that the SK model shows a spin-glass transition from the paramagnetic phase with $q_{\alpha\beta} = 0$ to a spin-glass phase with non-zero $q_{\alpha\beta}$ as the temperature is reduced. Although the replica symmetric solution correctly predicted the

existence of a spin-glass transition, however this solution had some unphysical properties such as an instability of the spin-glass phase and a negative value for the entropy below the critical temperature!

To overcome the problems of the replica symmetric solution, it was clear that the symmetry had to be broken, but the way that it needed to be broken was not trivial. A very clever solution was introduced by Parisi [58] based on the metric structure of the replica-index space. In the Parisi solution, the mutual overlap q between two replicas with indices α and β is defined by (1.6.6), and the probability distribution of the overlap q for a given J is defined as

$$P_J(q) = \sum_{\sigma\tau} P_\sigma P_\tau \delta(q - q_{\sigma\tau}) \tag{1.6.7}$$

in which P_σ is the probability for the system to be in the pure state σ and it is proportional to the Gibbs factor (1.4.3) for that pure state[3]. If there is only one pure state, then $q_{\alpha\beta}$ will be the same as the EA order parameter, i.e., $q_{\text{EA}} = \left\langle \langle S_i \rangle_{\text{th}}^2 \right\rangle_J$. But if there is more than one pure state, then $P_J(q)$ is not a single delta function, i.e.,

$$P_J(q) \neq \delta(q - q_{\text{EA}}), \tag{1.6.8}$$

and we say that the replica symmetry is broken, since the two identical replicas of the system may happen to be in very different pure states [60]. In this case, the mutual overlap q does not have only a single value (as q_{EA}) and it can be defined as a function $q(x)$ where x represents the distance between two replica indices and $0 \leq x \leq 1$. The function $P_J(q)$ is known to be non-trivial and it depends on the disorder realization J even in the thermodynamic limit [61] which is not very promising because it means there is no unique function for $P_J(q)$ in the thermodynamic limit, and as a result, $q(x)$ is not self-averaging [1]. In order to eliminate the dependency of $P_J(q)$ on J, we can define

$$P(q) = \langle P_J(q) \rangle_J, \tag{1.6.9}$$

as the average of $P_J(q)$ over disorder. Figure 1.2 shows the function $P(q)$ for a system with the EA Hamiltonian (1.3.1) on a lattice of the linear size L and dimension $d = 4$ ($N = L^4$ spins) with nearest-neighbor interactions J obeying (1.3.2), averaged over many realizations of J. As we can see, $P(q)$ has two peaks which become sharper by increasing L, and it has a continuous part between the two peaks [60]. The peaks tend toward delta functions in the limit of $L \to \infty$, however the continuous part will remain between them at this limit, i.e., $P(0) \neq 0$

[3] A pure state is a sub-component (valley) of the phase space of the system separated by energy barriers at equilibrium [60].

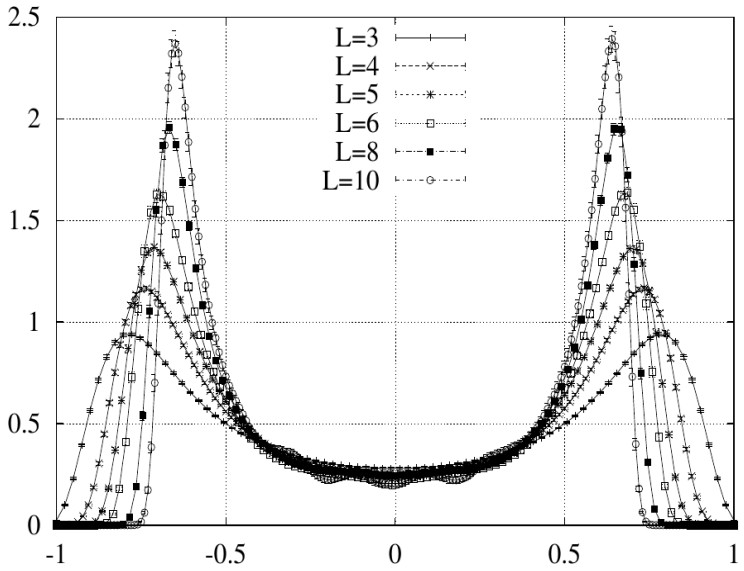

Figure 1.2: The function $P(q)$ in the RSB picture for systems with the EA Hamiltonian (1.3.1) and Gaussian bond distribution with $N = L^4$ spins for $3 \leq L \leq 10$. The figure is taken from Ref. [60].

even in the thermodynamic limit[4]. The continuity of $P(q)$ is an important feature of the RSB picture because, as we will see in the next section, it is one of the main disagreements between the RSB and the droplet picture.

1.6.2 Droplet picture

Fisher and Huse in 1988 [10] proposed a new picture for the ordered phase in spin glasses called the droplet picture which is based on a scaling hypothesis relating to local excitations of the spin-glass phase. To be specific, a droplet is a domain of coherent spins around a particular point which can only be flipped together. According to the droplet picture, the typical excitation energy of a droplet of linear size l is

$$F(L) \sim l^{\vartheta}, \tag{1.6.10}$$

where ϑ is called the *droplet exponent*. Fisher and Huse in [10] argued that $\vartheta \leq (d-1)/2$ where d is the space dimension of the system. The boundaries of the droplets are not fixed, they move around due to the disorder of the system exploiting unsatisfied bonds and avoiding the strong satisfied ones. The energy distribution of droplets of linear size l is broad, but according to Eq. (1.6.10) one can conclude that for $d > 1$ and $\vartheta > 0$ an infinite energy would be needed to excite a finite fraction of the total number of spins in the thermodynamic limit, therefore only small excitations are considered in the droplet picture.

[4]This is what the authors of Ref. [60] have claimed from Fig. 1.2, however it is still not perfectly clear whether the link between the peaks survives in the thermodynamic limits for $d = 4$.

Another type of excitations can be activated by a particular change in the boundary conditions of the system. The energy difference between the two boundary conditions is called the *stiffness*. A common way to determine the stiffness of the system was proposed by Banavar in 1982 [62]. He used the difference between the energies of the system with periodic (E_{P}) and antiperiodic (E_{AP}) boundary conditions. Changing the boundary conditions induces a domain wall across the system which is responsible for the difference between the energies of the two boundary conditions, i.e., $\Delta E = E_{\mathrm{P}} - E_{\mathrm{AP}}$. The energy excitation for the domain walls scales with the linear size of the system as

$$|\Delta E(L)| \sim L^{\theta}, \tag{1.6.11}$$

in which θ is known as the *stiffness exponent*. It plays an important role in phase transitions of spin glass systems in the droplet picture. According to Ref. [63] the sign of the stiffness exponent determines whether or not a phase transition takes place at a finite temperature. If $\theta > 0$ the phase of the system at zero temperature is strongly ordered and it is stable against thermal fluctuations, leading to a finite-temperature phase transition. However when $\theta < 0$ the ordered phase is fragile at zero temperature and any thermal fluctuations will destroy it, leading to criticality at zero temperature. The situation with $\theta = 0$ would be the marginal case. Ising spin glasses for $d \geq 3$ are examples of systems where the spin-glass phase persists to finite temperature and thus $\theta > 0$. On the other hand in $d = 2$, a spin-glass state of Ising spin glasses with Gaussian bond distribution exists only at $T = 0$ so $\theta < 0$, but for systems with $\pm J$ couplings the value of the stiffness exponent is much closer to the marginal value $\theta \approx 0$ [64]. Since criticality is at zero temperature for the 2D models, the correlation length exponent ν is expected to follow from $\nu = -1/\theta$ [63] and as $\eta = 0$ (at least for Gaussian couplings) then the stiffness exponent becomes the only relevant critical exponent for these systems [65].

Both the droplet exponent ϑ and the stiffness exponent θ relate the energy of excitations to the length of the system in a similar way. The droplet picture makes the plausible assumption that ϑ can be identified with θ [1, 64]. In addition to the similarity in scaling the excitation energy of the droplets and the domain walls, the droplet interfaces and the domain-wall boundaries are found to be fractal curves with a non-trivial fractal dimension d_{f} where $d - 1 < d_{\mathrm{f}} < d$, so both of them are not space filling [10].

Among various results of the droplet picture, the form of $P(q)$ is quite important. Considering $P(q;L)$ as the probability distribution of the overlap q for a system of linear size L, then according to the droplet picture the variance of $P(q;L)$ scales

with the system size as

$$(\Delta q)^2 = \left\langle \langle q^2 \rangle_{\text{th}} \right\rangle_J - \left\langle \langle q \rangle_{\text{th}}^2 \right\rangle_J \sim L^{-\theta}, \tag{1.6.12}$$

where θ is a positive stiffness exponent [66]. Therefore, in the thermodynamic limit where $P(q;L)$ tends to $P(q)$, the width of the distribution tends to zero and the function $P(q)$ is consisted of two delta functions located at $q = \pm q_{\text{EA}}$ [67], in which the two states with $q = +q_{\text{EA}}$ and $q = -q_{\text{EA}}$ are related to each other by the inversion of all spins. Therefore $P(q)$ is a discrete trivial function in the droplet picture while it is a continuous non-trivial function in the RSB picture.

Over the last decades, there has been a vast number of studies trying to clarify the dichotomy between the RSB and the droplet picture, but they have found different results mainly due to the different temperature ranges, different system sizes and different dimensions in the studies. Some of the studies of 3D spin glasses (see Refs. [68, 69, 70, 71], for instance) have concluded that these systems actually show properties of both of the two pictures, and therefore they proposed a new picture called TNT which stands for "trivial, non-trivial" [72]. However, one thing which has been mathematically proven is that the RSB picture works for higher dimensions than the upper-critical dimension, i.e., for $d > d_u = 6$, while the droplet picture is exact for $d = 1$ [2], and the debate for the intermediate dimensions is still going on.

1.7 Why do we study 2D spin glasses?

In this thesis, we study the properties of Ising spin glasses in two dimensions. The physics of these systems is in fact rather interesting in its own right [53]. One intriguing aspect is that for asymmetric coupling distributions a long-range ferromagnetic phase does exist at non-zero temperatures, and it is found that the phase boundary at low temperatures shows re-entrance or inverse melting, that is, on further cooling a system in the ferromagnetic phase, order is lost in favor of a paramagnetic state [73, 74]. Another facet is the question of universality regarding the distribution of exchange couplings: at zero temperature, the bimodal model has extensive ground-state degeneracies leading to behavior rather different from the case of continuous coupling distributions [75]. The resulting entropy of volatile spin clusters was long believed to lead to power-law correlations at zero temperature, but there is now evidence of true long-range spin-glass order [46, 25]. The behavior of this model at low temperatures is determined by a delicate interplay of the distinct fixed points of the universality classes of discrete and continuous coupling distributions, respectively [76, 77, 78, 79], and universality at finite temperature could only very recently be demonstrated [80]. It is the

subtle role played by entropic fluctuations which makes this model relevant to the finite-temperature transitions observed in three dimensions [76].

Apart from such theoretical considerations, interest in the 2D models has been fueled by their relative advantage in numerical tractability as compared to higher-dimensional systems. This goes beyond the general advantage of systems in low dimensions of providing larger linear system sizes at the same number of sites: 2D systems in zero external field are an exception to the *NP* hardness of ground-state problems found in systems of higher dimensions [81]. Ground states on planar graphs can be determined in polynomial time from the mapping to a minimum-weight perfect matching problem [82]. This allows to treat significantly larger lattice sizes than those accessible to simulation methods. The restriction to planar graphs, and hence periodic boundary conditions in at most one direction, has been rather inconvenient for certain types of studies [64] and, in general, leads to relatively larger finite-size corrections. Polynomial-time algorithms also exist for the more general problem of determining the partition function [83, 84, 85]. These techniques, based on the evaluation of Pfaffians, have the advantage of allowing for periodic boundary conditions, but they are technically more demanding than the ground-state computations and thus restricted to smaller system sizes. Only recent advances have allowed the extension of these approaches to system sizes $L \gtrsim 100$ [86]. In parallel, exact sampling techniques for Ising spin glasses based on the application of "coupling-from-the-past" [87], or sampling of dimer coverings, [88] have recently been suggested, that are either restricted to or only efficient in 2D [89, 86]. In addition to all these, the possibility of describing the domain walls of Ising spin glasses in 2D, at least with Gaussian bonds and under certain conditions, in terms of stochastic Loewner evolution (SLE) makes the 2D systems even more interesting [90, 91, 92]. Such consistency with SLE together with further assumptions would suggest a relation between stiffness exponent and fractal dimension, $d_f = 1 + 3/[4(3+\theta)]$ [90], where investigating the validity of this conjecture is one the goals of this thesis.

Chapter 2

Schramm-Loewner evolution and its properties

2.1 Introduction

Growth processes can be observed everywhere in nature at all scales, from crystals and plants to dunes and galaxies. Many such processes involve the growth of domains (i.e. correlated regions), for instance the domains in a magnetic material or percolation. At criticality a very small change in an environmental parameter, such as the external magnetic field or the temperature, can result in macroscopic changes in the physical properties of a system. Therefore understanding such processes is usually very difficult, even in low dimensions. But specifically in two dimensions, a powerful method of complex analysis allows us to study the growing shapes more easily. This method is known as *Schramm-Loewner evolution* (SLE) and it was introduced by Oded Schramm in 1999 [93] to characterize a family of one-parameter random curves in two dimensions. The corresponding parameter is usually denoted by κ, so SLE is often written as SLE_κ. Different physical models are connected to SLE_κ with different but specific values of κ. For example, it is known that critical percolation is related to SLE_6 [94].

SLE processes are very important because they are among the very few growth processes that can be studied analytically in great detail. In addition to that, another striking feature of SLE is that, in fact, it has turned many questions concerning interfaces of physical systems that seemed just out of reach into solvable problems of stochastic calculus [95].

In this chapter we study the Schramm-Lowener evolution by starting from some basic complex analysis. We then define two-dimensional conformal maps. A precise definition of SLE_κ is given next, and its basic properties are discussed after that. At the end, we demonstrate two important but rather simple calculations

with SLE and present some special values of κ connected to different physical models. We deliberately avoid going through all the complex mathematical details. Those readers who are interested in more mathematical background are referred to Refs. [96, 95, 97, 98, 99].

2.2 Conformal maps

Conformal mapping is a powerful method of analysis with many successful applications. In the present context, we introduce it as a foundation of Schramm-Loewner evolution. Conformal mapping uses functions of complex variables to transform complicated boundaries into simpler, more readily analyzed configurations. Therefore we start from the basic complex analysis behind conformal mapping, and we will define it according to our analysis.

2.2.1 Basic properties

As the simplest case of complex analysis, consider a point in the complex plane. The point can be shown by $z = x + iy$, in which x is the position of the point on the real axis and y shows its position on the imaginary axis. Both x and y are real variables, while z is a complex variable. By considering $x = \cos(\theta)$ and $y = \sin(\theta)$ in which $0 \leq \theta \leq 2\pi$, we will have $z = \cos(\theta) + i\sin(\theta) = e^{i\theta}$ which is a circle in the complex plane. We can also have a function of a complex variable, i.e., $w(z)$. It is known that functions of a complex variable obey Laplace's equation, $\nabla^2 w = \partial_x^2 + \partial_y^2 = 0$, everywhere except at singular points [96]. For instance, if $w(z) = 1/z$, then $w(z) = 1/(x+iy) = (x-iy)/(x^2+y^2)$ and we have

$$[\partial_x^2 + \partial_y^2][(x-iy)/(x^2+y^2)] = 0, \tag{2.2.1}$$

except at $z = 0$.

As the second example, consider the function $w(z) = \frac{1}{2}(z + 1/z)$. First of all we have:

$$[(\partial_x)^2 + \partial_y^2][(x+iy) + \frac{1}{x+iy}] = \frac{2x+2iy}{(x+iy)^4} + \frac{-2iy-2x}{(x+iy)^4} = 0 \quad (z \neq 0). \tag{2.2.2}$$

Now consider

$$z(r,\theta) = \begin{cases} e^{i\theta} & 0 \leq \theta \leq \pi \\ \pm e^{r} & 0 < r \end{cases} \tag{2.2.3}$$

in which θ and r are real variables. The curve sits in the z-plane and the region above the curve is shown by the domain $\mathbb{D}$ which is in the upper-half plane[1] in Figure 2.1.

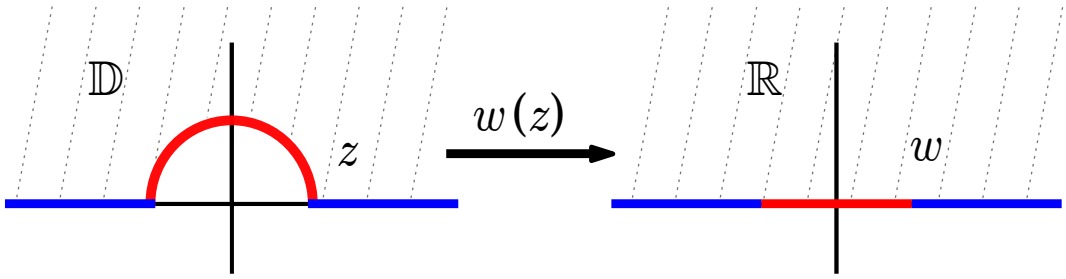

Figure 2.1: Schematic view of the function $w(z) = \frac{1}{2}(z + 1/z)$ which maps the curve $z = e^{i\theta}$ $(0 \leq \theta \leq \pi)$ from the upper-half plane of the z-plane into a line in the w-plane.

Plugging z into the function $w(z)$ yields

$$w(r,\theta) = \begin{cases} \cos(\theta) & 0 \leq \theta \leq \pi \\ \pm\cosh(r) & 0 < r. \end{cases} \tag{2.2.4}$$

Therefore the function $w(z)$, or we can call it the *map*, takes the curve in the z-plane into a curve in the w-plane. The map also takes the region $\mathbb{D}$ above the curve in the z-plane into the region $\mathbb{R}$ above the line in the w-plane in a one to one manner. This map is a simple example of a *"conformal map"*.

We may also go backwards. Consider $w(z) = \frac{1}{2}(z + \frac{1}{z})$ and solve if for z:

$$w(z) = \frac{1}{2}(z + \frac{1}{z}) \implies z^2 - 2wz + 1 = 0 \implies z = w \pm \sqrt{w^2 - 1}, \tag{2.2.5}$$

and consider $z = g(w) = w + \sqrt{w^2 - 1}$. By plugging w into the function $g(z)$, we will have $g(w) = \cos(\theta) + \sqrt{\cos^2(\theta) - 1} = \cos(\theta) + i\sin(\theta) = e^{i\theta}$ when $0 \leq \theta \leq \pi$ and $g(w) = \cosh(r) + \sqrt{\cosh^2(r) - 1} = e^r$ in which $0 \leq r$. Therefore the map $g(w)$ takes the region $\mathbb{R}$ to the region $\mathbb{D}$ and the line in the w-plane into the curve in the z-plane (see Figure 2.2).

[1] A *domain* is an open connected subset of the complex plane. A subset is *connected* if any two points in the subset can be connected by a curve lying entirely within the subset.

2.2.2 Definition

A *conformal map* is an analytic function $w = f(z)$ within a simply connected[2] region $\mathbb{D}$ in the complex z-plane [97]. The derivative of the function $\partial f/\partial z$ must be non-zero everywhere in the region. It then provides a one-to-one mapping of the interior of the domain $\mathbb{D}$ into the interior of another simply connected region $\mathbb{D}'$. The function maps the curves which bound these regions into one another as well. Riemann's theorem in conformal mapping ensures that for any two simply connected domains $\mathbb{D}$ and $\mathbb{D}'$ in the complex plane there is always an analytic function $w = f(z)$ which maps the interior of the domain $\mathbb{D}$ to that of the domain $\mathbb{D}'$ [97]. It does not matter how irregular the boundary of $\mathbb{D}$ is, because $f(z)$ is not necessarily analytic on the boundary. Riemann's theorem provides that for finite regions the mapping is unique. A conformal map preserves the angles between the two mapped regions (Fig. 2.3), so it is often called *angle-preserving* map as well. To go backwards from $\mathbb{D}'$ to $\mathbb{D}$, we can simply use the inverse function $g(w)$ which obeys $g(w) = g(f(z)) = z$. The inverse map is also unique [97].

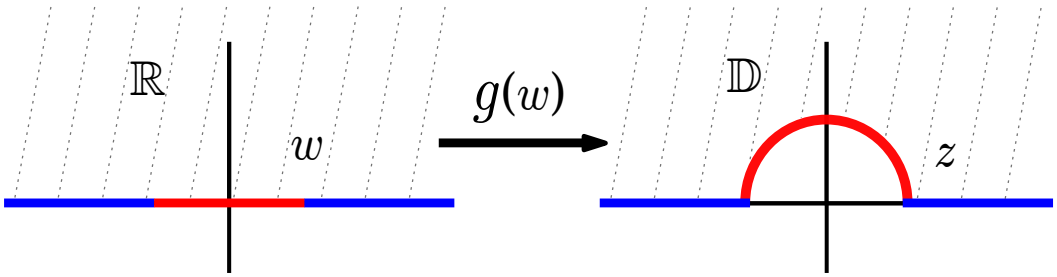

Figure 2.2: Schematic view of the function $z = g(w) = w + \sqrt{w^2 - 1}$ which takes the line from the w-plane into a curve in the z-plane.

2.3 Loewner's equation

Loewner was looking at a random curve γ in the complex z-plane and considered a conformal function $f(z)$, which maps the curve from domain $\mathbb{D}$ into another domain $\mathbb{D}'$. He then asked himself how he could impose a small deformation of this curve. Or generally speaking, what happens if we have a growing curve in the domain $\mathbb{D}$? Since the curve is growing, we can characterize it by a parameter, imagined as "*time*", and therefore we will have γ_t in which t is a real parameter and γ_t is a complex variable. In this case, the map $f(z)$ will be also changing in time and therefore we will have $f_t(z)$. Domains $\mathbb{D}$ and $\mathbb{D}'$ are usually considered as

[2] A simply connected domain is a domain in which every closed curve in the domain can be shrunk to a point of the domain continuously.

$\mathbb{H}\backslash\gamma_t$ and $\mathbb{H}$ respectively[3]. Therefore $f_t(z) : \mathbb{H}\backslash\gamma_t \longrightarrow \mathbb{H}$ maps the growing process (the random curve) to the upper-half of the z-plane. He then turned to considering the following partial differential equation[4]:

$$\frac{\partial f_t(z)}{\partial t} = \frac{2}{f_t(z) - u(t)} \tag{2.3.1}$$

in which $f_t(z)$ and z are complex, t and $u(t)$ are real, and the initial conditions are as follows:

$$f_0(z) = z, \quad 0 < f'(z). \tag{2.3.2}$$

Now the function $f_t(z)$ is not unique, but can be made so by imposing the following behavior at infinity:

$$\lim_{z\to\infty} f(z) \sim z. \tag{2.3.3}$$

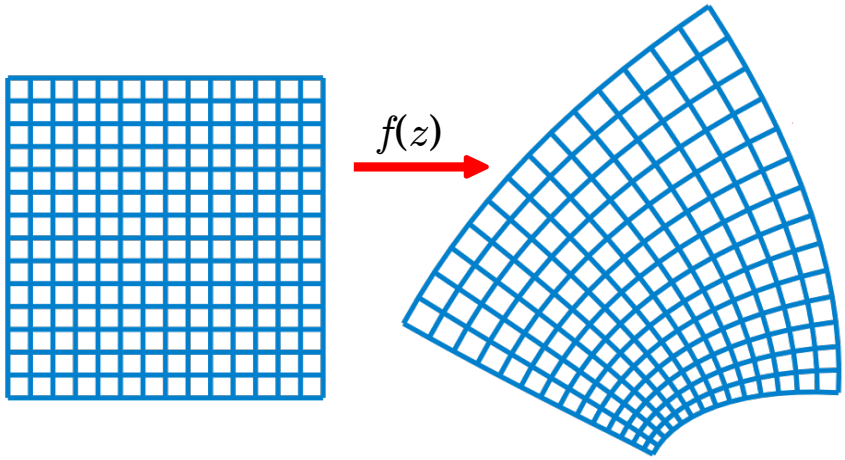

Figure 2.3: A rectangular grid (left) and its image under a conformal map $f(z)$ (right). It is seen that the conformal map preserves the angles (f maps pairs of lines intersecting at 90 to pairs of curves still intersecting at 90).

The function $u(t)$ is called the *driving function*, Eq. (2.3.1) is known as *Loewner's equation*, and the time development of the function $f_t(z)$, as generated by Eq.(2.3.1), is called *Loewner evolution* [96]. The Loewner equation can be seen as a machine for producing a curve which depends upon the driving function $u(t)$. Thus we have reduced the problem of characterizing random curves in the upper-half plane $\mathbb{H}$ to a similar problem of random continuous real functions, and putting a measure on such curves is equivalent to putting a measure on such functions. Therefore if we want to study how the curve γ_t grows, we can rather think of how the mapping $f_t(z)$ changes as γ_t grows. This is often easier, because for any point

[3] $\mathbb{H}\backslash\gamma_t$ is the complement of γ_t in the upper-half plane.
[4] The origin of this equation as well as its mathematical proof can be found in Ref. [96]

not on the boundary of the domain, the mapping f_t changes much more smoothly than the original γ_t [97].

2.3.1 A simple example

Let us consider the very simple case that the driving function is just a constant, i.e., $u(t) = u(0) = u_0$. Therefore γ_t will be a straight line which is growing vertically. According to Loewner's equation (2.3.1) we will have:

$$\frac{\partial f_t(z)}{\partial t} = \frac{2}{f_t(z) - u_0} \implies \frac{\partial}{\partial t}(f_t(z) - u_0)^2 = 4,$$

and therefore $(f_t(z) - u_0)^2 = 4t + c$, where c is the constant of integration. Taking the initial condition $f_0(z) = z$ into account, it is implied that $f_t(z) = u_0 + \sqrt{4t + (z - u_0)^2}$. At the point where the square root changes sign, i.e., $z = u_0 + 2i\sqrt{t}$, this solution has a branch cut which is running up at the point $\mathrm{Re}(z) = u_0$ up to $\mathrm{Im}(z) = 2\sqrt{t}$. So the conformal map takes the tip of the curve to the real axis (Fig. 2.4).

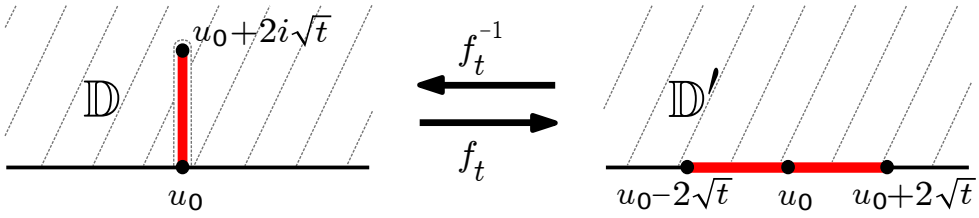

Figure 2.4: Schematic view of Loewner evolution with a constant driving function $u(t) = u_0$. The domain $\mathbb{D}$ is the upper-half plane less the brunch cut, and the domain $\mathbb{D}'$ is the upper-half plane.

2.4 Schramm-Loewner Evolution

In the case that we are interested in, γ_t is a random curve and the driving function $u(t)$ is a random continuous function. Schramm's idea was to consider the driving function as:

$$u(t) = \sqrt{\kappa} B_t, \tag{2.4.1}$$

in which B_t is simply one-dimensional Brownian motion, and κ is the diffusion constant of the relative Brownian motion. Thus $\langle u(t) \rangle = 0$ and $\langle [u(t_1) - u(t_2)]^2 \rangle = \kappa |t_1 - t_2|$. SLE_κ in the upper-half plane is known as the collection of such conformal maps $f_t(z)$ obtained by solving the Loewner equation (2.3.1) when $u(t) = \sqrt{\kappa} B_t$ and B_t is the standard one-dimensional Brownian motion. It will turn out that while changing the diffusion constant, κ, does not qualitatively change the behavior of

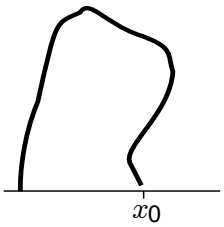

Figure 2.5: The random curve is about to hit the real axis and enclose a region. The whole region will be mapped to one point by f_t.

the Brownian motion, it will drastically alter the behavior of SLE_κ and so different values of κ will correspond to different universality classes of critical behavior [96]. SLE_κ can be defined in different variations corresponding to different boundary conditions. The most common variations of SLE are *chordal* and *radial* SLEs. Chordal SLE refers to the situation where the random curve connects two points on the boundary of a simply connected domain, while in radial SLE the random curve connects one point on the boundary to an interior point of the domain [100]. For more description about different variations of SLE, their properties and applications see, e.g., Ref. [101].

2.4.1 Phases of SLE

As the first assumption, imagine $\kappa = 0$. Therefore we have no driving force and γ_t would present as a vertical straight line. If we increase κ slightly, the tip of the curve starts going to the left or right frequently. By keeping increasing κ, the tip will move more frequently and depending on the value of κ it may even intersect the real axis as well as itself.

To see this behavior, consider a random process on the real axis. Let $x_t = f_t(x_0) - u_t$ be the distance between the image at time t of a point which starts at x_0 and the image u_t of the tip. Now we can ask how x_t changes as time increases. Such processes are interpreted in the 'Itô sense' [102], that is, as the limit as $\delta t \to 0$ of the forward difference equation:

$$x_{t+\delta t} \approx x_t + \frac{2\delta t}{x_t} - \int_t^{t+\delta t} \sqrt{\kappa} dB_{t'} dt'. \tag{2.4.2}$$

As $\delta t \to 0$ we will have

$$dx_t = \frac{2dt}{x_t} - \sqrt{\kappa} dB_t, \tag{2.4.3}$$

which shows the point x_t is subject to a random force but it is also repelled from the origin. Now if we forget the term of the random force ($\sqrt{\kappa} dB_t$), we will have $\langle x_t^2 \rangle \sim 4t$, and if we neglect the term of the repulsive force, we would have $\langle x_t^2 \rangle \sim \kappa t$.

Therefore if $\kappa < 4$ the repulsive force is stronger and thus the tip of the curve will go to infinity. In this case the curve is simple, i.e., there are no double points. However as the value of κ becomes larger than 4, the random force wins and the curve can hit itself and the real axis. Fig. 2.5 shows the curve about to hit the real axis. In this case, the right and the left side of the curve as well as the real axis get mapped to a very small segment of the real axis, which gets smaller as the tip approaches x_0. When the tips gets very close to x_0, the entire region enclosed by the curve as well as the tip and x_0 will be mapped into a single point. Therefore $x \to 0$ which means the curve hits the origin.
For large κ, there are no finite regions enclosed by the curve which are not on the trace itself. It means that γ_t is a space filling curve, i.e., γ_t intersects every neighborhood of every point in the upper-half plane $\mathbb{H}$ (Fig. 2.6).

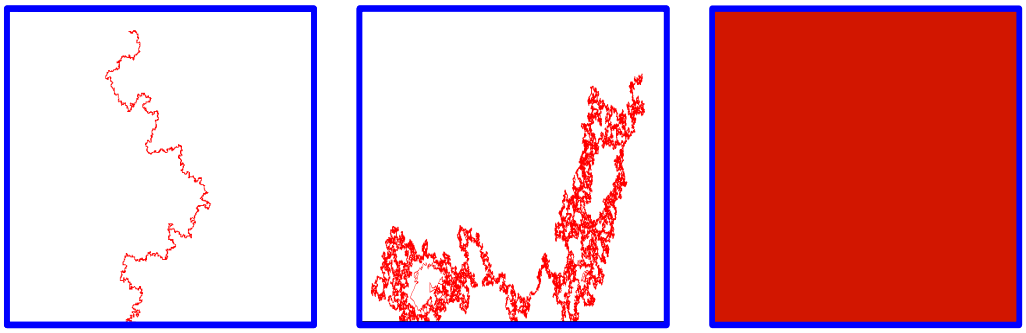

Figure 2.6: Schematic view of SLE_κ for different values of κ. The left snapshot corresponds to $\kappa \leq 4$ in which γ_t is a simple curve avoiding the real axis. When $4 \leq \kappa \leq 8$, γ_t hits itself as well as the real axis (the middle snapshot), and for $8 \leq \kappa$ the curve is space filling (the right snapshot). The figure is taken from Ref. [103].

2.4.2 The postulates of SLE

SLE has two basic properties which must be assumed to hold for a particular random process to be compatible with SLE[5]. The first property is as follows:

Property 1: Domain Markov Property

Consider a curve γ which connects the points z_1 and z_2 in the domain $\mathbb{D}$. If we divide the path into two disjoint parts: γ_1 from z_1 to an arbitrary point z_a and γ_2 from z_a to z_2, then the conditional probability distribution of γ_1 is the same as the unconditional distribution of the whole curve starting from z_a and ending at z_2 but in the domain $\mathbb{D}\backslash\gamma_1$, i.e.

$$p(\gamma_2|\gamma_1;\mathbb{D},z_1,z_2) = p(\gamma_2;\mathbb{D}\backslash\gamma_1,z_a,z_2) \tag{2.4.4}$$

[5]These properties can be also proven. For the mathematical proof we refer to Ref. [101].

Property 2: Conformal Invariance

Imagine a conformal map f which maps the interior of the domain $\mathbb{D}$ to the interior of the domain $\mathbb{R}$ as well as the boundaries of the two domains. Therefore the points (z_1, z_2) on the boundary of the domain $\mathbb{D}$ are mapped to the points (w_1, w_2) on the boundary of the domain $\mathbb{R}$. According to the conformal invariant property of SLE a measure μ on the curve in $\mathbb{D}$ is the same as the measure $f * \mu$ on the image of the curve in $\mathbb{R}$, i.e.,

$$(f * \mu)(\gamma; \mathbb{D}, z_1, z_2) = \mu(f(\gamma); \mathbb{R}, w_1, w_2). \tag{2.4.5}$$

We will later use these properties to calculate two interesting quantities by SLE.

2.5 Consequences of SLE

We have already seen that SLE characterizes a random curve γ_t in two dimensions by only one parameter which is, indeed, the diffusion constant of the Brownian motion κ. In addition to that, instead of studying the random curve γ we will consider a set of conformal maps that change much more smoothly than the original curve. Now we want to turn our attention to two interesting but relatively simple calculations which can be carried out due to SLE.

2.5.1 Left passage probability

Imagine we have a curve γ_t which connects two points z_1 and z_2 on the boundaries of a domain $\mathbb{D}$. As usual, we consider the domain to be the upper-half plane $\mathbb{H}$, z_1 to be fixed at the point a_0, and z_2 to be at infinity. Now we can ask what is the probability that the curve passes to the left of a given point z? This probability is known as *left-passage probability* and it is not a quantity which is natural in conventional approaches to critical behavior, but can be quite straightforwardly computed within SLE [104].

We denote the probability that the curve γ passes to the left of the point z by $P(z, \bar{z}; a_0)$. Now consider the infinitesimal time evolution of SLE. So $a_{dt} = a_0 + \sqrt{\kappa} dB_t$, and at the same time, the point z will be mapped to $f_{dt}(z) = z + \frac{2dt}{z - a_0}$. In addition to that, γ' will lie to the left of z' if γ lies to the left of z. Therefore we can write:

$$P(z, \bar{z}; a_0) = \left\langle P(z + \frac{2dt}{z - a_0}, \bar{z} + \frac{2dt}{\bar{z} - a_0}, a_0 + \sqrt{\kappa} dB_t) \right\rangle, \tag{2.5.1}$$

in which the average $\langle \dots \rangle$ is taken over all realisations of Brownian motion dB_t up to time dt. Taylor expansion, using $\langle dB_t \rangle = 0$ and $\langle (dB_t)^2 \rangle = dt$, and putting the coefficient of dt equal to zero gives

$$\Big(\frac{2}{z-a_0}\frac{\partial}{\partial z} + \frac{2}{\bar{z}-a_0}\frac{\partial}{\partial \bar{z}} + \frac{\kappa}{2}\frac{\partial^2}{\partial a_0^2} \Big) P(z,\bar{z};a_0) = 0. \tag{2.5.2}$$

Therefore $P(z,\bar{z};a_0)$ satisfies a linear second-order partial differential equation which is typical of conditional probabilities in stochastic differential equations [96].

The trivial solution of the above equation is $P = \text{const}$. For the non-trivial solution, assume $z = x + iy$ and by the scale invariance property of SLE, the probability that the curve γ of SLE_κ passes to the left of z can depend only on the ratio $u = \frac{x}{y}$. Therefore Eq. (2.5.2) will be reduced to an ordinary second-order linear differential equation which is in fact hypergeometric. The boundary conditions $P(\infty) = 1$ and $P(-\infty) = 0$ imply that the left passage probability P has the following form:

$$P_{\text{LP}}^{\kappa}(x,y) = \frac{1}{2} + \frac{\Gamma(4/\kappa)}{\sqrt{\pi}\,\Gamma\left(\frac{8-\kappa}{2\kappa}\right)} \frac{x}{y} {}_2F_1\left(\frac{1}{2}, \frac{4}{\kappa}; \frac{3}{2}; -\left(\frac{x}{y}\right)^2 \right) \tag{2.5.3}$$

where ${}_2F_1$ is Gauss' hypergeometric function:

$${}_2F_1(a_1,a_2;b;z) = \sum_{k=0}^{\infty} \frac{\Gamma(k+a_1)}{\Gamma(a_1)} \frac{\Gamma(k+a_2)}{\Gamma(a_2)} \frac{\Gamma(b)}{\Gamma(k+b)} \frac{z^k}{k!}. \tag{2.5.4}$$

This formula holds for the SLE process in which the curve starts from the origin of the upper-half plane and ends at infinity. Eq. (2.5.3) can be used to determine the appropriate value of κ for the ensemble of random curves in the upper-half plane. To do so, one can calculate the left passage probability (LPP) for those set of curves and look at the deviation of the computed left passage probability from the exact result of Eq. (2.5.3) for different values of κ and take the spatial average over the whole domain. The relevant value of κ will be the value which minimizes the averaged deviation [96]. Later on, we will use this formula to calculate the value of κ for the domain walls of the 2D Ising spin glasses.

2.5.2 Fractal dimension

Another quantity that can be calculated by SLE through a relatively simple calculation is the fractal dimension d_{f}. To show how the fractal dimension is related to SLE, we first start from the definition of the fractal dimension, and then we derive a relation between the fractal dimension d_{f} and κ of SLE_κ.
To explain the concept of fractal dimension, it is necessary to understand what we

mean by dimension in the first place. A line has dimension 1, a plane dimension 2 and a cube dimension 3. But why is a line one-dimensional and the plane two-dimensional? One answer is that a line has only one linearly independent direction, while in the plane there are 2 linearly independent directions. This is true, but how we can express that in particularly rigorous mathematical language? Note that all of these objects are *self-similar*. We may break a line segment into 2 self-similar intervals, each with the same length, and each of which can be magnified by a factor of 2 to yield the original segment. In general, we can break a line segment into N self-similar pieces, each with magnification factor N. However, the square is different. We can decompose a square into 4 self-similar sub-squares, and the magnification factor here is 2. Clearly, the square may be broken into N^2 self-similar copies of itself, each of which must be magnified by a factor of N to yield the original figure (Fig. 2.7). Finally, we can decompose a cube into N^3 self-similar pieces, each of which has magnification factor N.

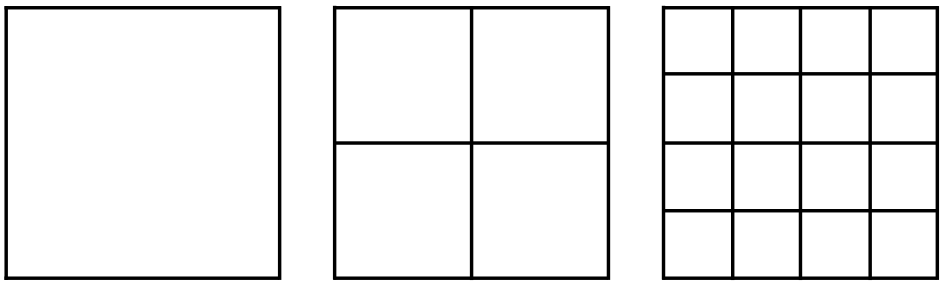

Figure 2.7: A square may be broken into N^2 self-similar pieces, each with magnification factor N.

Now we see an alternative way to specify the dimension of a self-similar object: the dimension is simply the exponent of the number of self-similar pieces with magnification factor N into which the figure may be broken. So we can say:

$$dimension: \quad d = \frac{\log[\text{number of self-similar pieces}]}{\log[\text{magnification factor}]}. \tag{2.5.5}$$

Therefore the dimension of a line is: $\log(N)/\log(N) = 1$, the dimension of a square is $\log(N^2)/\log(N) = 2$ and similarly $\log(N^3)/\log(N) = 3$ for the dimension of a cube.
Thus, we take as the definition of the fractal dimension of a self-similar object as follow:

$$fractal\ dimension: \quad d_{\mathrm{f}} = \frac{\log[\text{number of self-similar pieces}]}{\log[\text{magnification factor}]}. \tag{2.5.6}$$

Fig. 2.8 shows a Sierpinski triangle which is a famous example of a self-similar object (fractal). The triangle breaks into 3^N self-similar pieces with magnification factors 2^N, therefore the fractal dimension is: $d_f = \log(3^N)/\log(2^N) = \log_2 3 \approx 1.58$.

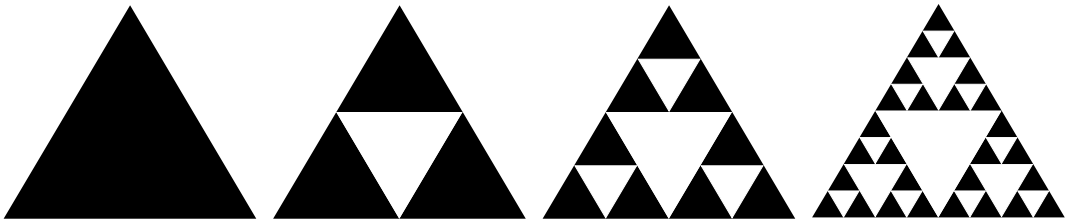

Figure 2.8: Sierpinski triangle. Every edge of the black triangle will be divided into two parts at each step. At the first step the edge is divided into 2 and will have 3 black triangles. At the next step we have 9 triangles while the edges is divided into 4 parts. Therefore $d_f = (\log 9/\log 4) = (\log 3/\log 2) \approx 1.58$.

Physicists usually define the fractal dimension roughly as follows: imagine we want to cover an object with some discs of radius ε, and $N(\varepsilon)$ be the minimum number of discs we need. Now if $N(\varepsilon) \sim \varepsilon^{-d_f}$ as $\varepsilon \to 0$, then d_f is the fractal dimension. An equivalent definition, for random fractals, is to ask about the probability $P(x,y,\varepsilon)$ that the fractal intersects a disc of radius ε centered on $z = x+iy$. If $P(x,y,\varepsilon) \sim \varepsilon^{D-d_f} f(z)$ as $\varepsilon \to 0$, in which D is the embedding dimension, then d_f is the fractal dimension [96]. In our case $D = 2$.

Now consider one of such discs with radius ε and suppose that we have a random curve γ where the curve intersects the disc. As we show in Fig. 2.9, the function f_t maps the first short segment of γ to the real axis. The rest of the curve is also moved as well as the disc. The center of the disc, z, will be mapped to $f_{\delta t}(z)$ and the radius of the disc will change slightly to $|f'_{\delta t}(z)|\varepsilon$. Since f_t is a conformal map, the measure on the image is the same as that on the original curve. Therefore we can write

$$P(x,y,\varepsilon) = \left\langle P\left(x + \frac{2x\delta t}{x^2+y^2} - \sqrt{\kappa}\delta B_t,\ y - \frac{2y\delta t}{x^2+y^2},\ (1 - \frac{2(x^2-y^2)\delta t}{(x^2+y^2)^2})\varepsilon\right)\right\rangle, \qquad (2.5.7)$$

where the average is taken over the Brownian motion δB_t, i.e., the possible configurations of the first segment of the curve which has been erased by $f_{\delta t}$. We then expand the equation to first order in δt, and this yields

$$\left(\frac{2x}{x^2+y^2}\frac{\partial}{\partial x} - \frac{2y}{x^2+y^2}\frac{\partial}{\partial y} + \frac{\kappa}{2}\frac{\partial^2}{\partial x^2} - \frac{2(x^2-y^2)}{(x^2+y^2)^2}\varepsilon\frac{\partial}{\partial \varepsilon}\right)P = 0. \qquad (2.5.8)$$

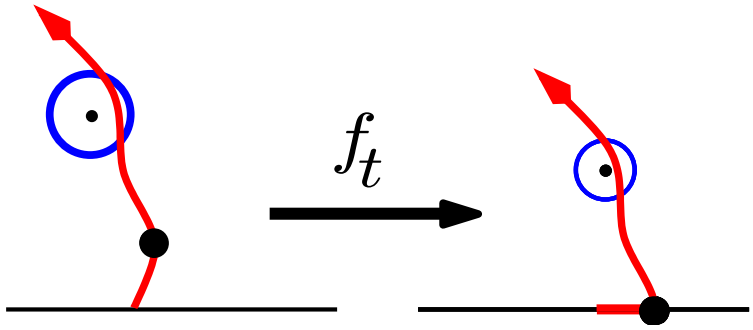

Figure 2.9: Schematic representation of how a conformal map f_t acts on a random curve going through a disc. The first segment of the curve will be mapped to the real axis, and as a result, both the centre and the radius of the disc will be changed.

Note that since $\langle(\delta B_t)^2\rangle = \delta t$ we need to expand this term up to the second order. Now P is dimensionless and thus should have the form $(\frac{\varepsilon}{r})^{2-d_f}$ times a function of the polar angle θ in which $r^2 = |z|^2 = (x^2 + y^2)$ and $\cot(\theta) = \frac{x}{y}$. In fact, the simple ansatz $P = \varepsilon^{2-d_f} y^\alpha (x^2 + y^2)^\beta$ with $\alpha + 2\beta = d_f - 2$ satisfies the equation. This gives us $\alpha = \frac{(\kappa-8)^2}{8\kappa}$, $\beta = \frac{(\kappa-8)}{2\kappa}$ and

$$d_f = 1 + \frac{\kappa}{8}, \tag{2.5.9}$$

which is valid for $\kappa \leq 8$. For larger κ we have another solution with $\alpha = \beta = 0$ and $d_f = 2$ [96].
For the straight line we have $\kappa = 0$ and therefore the fractal dimension is $d_f = 1$, which is, in fact, the dimension of a straight line. By increasing the value of κ, the fractal dimension increases steadily until $\kappa = 8$ that results in $d_f = 2$, which is indeed the dimension of the domain (and the maximum possible value for fractal dimension). Beyond this value, the curve becomes space-filling and every point in the upper-half plane lies on the curve.

Equation (2.5.9) can be used as another method to check whether an ensemble of random curves in the upper-half plane can be considered as SLE or not. In this way we need to calculate d_f and κ (using other methods) for those random curves and check whether they satisfy Eq. (2.5.9) or not. We will also use this equation for studying the domain walls of the 2D Ising spin glasses.

2.6 SLE and critical phenomena

The macroscopic behavior of systems studied in statistical physics mainly falls in two categories. In the first category, the macroscopic behavior of the system can be studied by phenomenological theories such as thermodynamics and hydrodynamics [105]. In the other case, however, the macroscopic state of the system shows

some sort of unusual bevaior, for instance, a slight change in temperature can cause a sudden massive change in the macroscopic state of the system. Random walks, percolation and spin glasses near criticality are some examples of the latter case. A bunch of different methods such as scaling analysis and renormalization group have been developed to study these systems, and statistical physicists are still seeking for new techniques and ideas to give them a deeper understanding [100]. Among different techniques, SLE is a very powerful mathematical tool which can gives us new insights of critical curves, clusters and random shapes in 2D critical phenomena [100].

In order to understand the relation between SLE and critical phenomena, let us mention a characteristic example. Consider the usual Ising model described by Hamiltonian (1.3.1) on a lattice subject to short-range interactions. According to Eq. (1.5.1), the correlation length of the system diverges as $\xi \propto |T - T_c|^{-\nu}$ when temperature approaches T_c. This means at the critical point the system becomes scale invariant, i.e., it is spatially self-similar on all scales, and thus the domain wall of the system becomes a fractal curve with a particular fractal dimension [100]. Here SLE comes into play and presents a direct analytical method to generate such a random curve. The fact that a random curve in 2D can be characterized fully by a real function in 1D is itself an interesting result. In addition to that, SLE also provides the fractal dimension d_f of the domain wall by linking it to the diffusion constant κ of the Brownian motion driving the SLE, i.e., $d_f = 1 + \frac{\kappa}{8}$ (Eq. (2.5.9)), and therefore determines the universality classes by a single parameter κ [100]. Moreover, SLE connects the central charge c in the conformal field theory (CFT) to κ by means of the expression $c = (3\kappa - 8)(6 - \kappa)/2\kappa$ and thus allows us to determine new scaling exponents [102].

It is known that many of the random paths defined in the two-dimensional critical models can be describe by SLE_κ. Different models are characterized by different values of κ. Here we show some examples of these models as well as the specific value of κ associated with those models:

- $\kappa = 2$: loop-erased random walk [106],
- $\kappa = \frac{8}{3}$: self-avoiding walk [107],
- $\kappa = 3$: boundaries of Ising spin clusters [96],
- $\kappa = 6$: percolation [94],
- $\kappa = 8$: uniform spanning trees [108],

and no lattice candidates for $\kappa > 8$ or for $\kappa < 2$ have been reported. This possibly has to do with the fact that, for $\kappa > 8$, the SLE process is not reversible, i.e., the rule

on curves obtained from z_1 to z_2 is not the same as the rule when we interchange the points, while we know that curves in equilibrium lattice models should satisfy reversibility [96]. It should be noted that some of these associations are proven and some of them are, to date, conjectured.

Chapter 3

Domain-wall excitations in the two-dimensional Ising spin glass

3.1 Introduction

Studying the low-temperature behavior of disordered systems such as spin glasses is quite difficult due to the glassy dynamics and multiple metastable states which are the essential properties of those systems [109]. Scaling arguments [110, 7, 10] indicate that many properties of the glassy state, including the scaling of the energy of excitations and correlation functions, can be found by studying the ground state and its response to perturbations. Therefore finding the ground state is the crucial key for studying those systems. Monte Carlo simulations, parallel tempering, genetic algorithms and extremal optimization are examples of heuristic algorithms to find close approximations of the ground state [111]. There are also some algorithms which enable us to calculate the exact ground state such as branch-and-cut [112] and transfer matrix methods [7]. These algorithms require times that are exponential in powers of the system size.

It is known that finding the ground state of Ising spin glasses in three (and higher) dimensions is an NP-hard problem [81], which means that very likely there cannot be an algorithm to calculate the ground state in polynomial time. However the ground state of the two-dimensional Ising spin glass can be found in polynomial time by mapping the problem of finding the ground state onto different well-known mathematical problems which polynomial algorithms exist for solving them [81]. One of these algorithms in 2D was introduced by Bieche *et al.* in 1980 [82]. This method uses a complete graph where the vertex set V contains the frustrated plaquettes and the edges connect all the vertices in V to each other. The shortest path between the vertices of that complete graph is then calculated. The

answer of the shortest path problem is equivalent to the minimum energy of the system, i.e., the ground state.

Another efficient method for calculating the exact ground state of the two-dimensional Ising spin glass systems was recently introduced. The algorithm is based on the well-known mathematical problem of *minimum-weight perfect matching* (MWPM) on an auxiliary graph where the nodes are replaced by Kasteleyn cities [113, 21]. This algorithm is faster than Bieche's algorithm and needs less memory to implement. Therefore larger system sizes can be studied by using this algorithm. Both of the algorithms are based on planar graphs, and they fail when fully periodic boundary conditions are applied, as finite size corrections vanish much more quickly than planar geometries[1]. Therefore it would be very useful to have a fast algorithm for calculating the ground states for the two-dimensional Ising spin glasses when we have periodic boundary conditions in both directions.

In the following we discuss a new quasi-exact algorithm which allows the ground state of systems with periodic-periodic boundary conditions to be found in polynomial time. Our algorithm is based on the combination of the windowing technique and the minimum-weight perfect matching problem. An introduction to the matching problem and Thomas' algorithm is presented in the first section of this chapter (sec. 3.2). We then introduce the main idea of our algorithm in section 3.3. Using this algorithm, quasi-exact ground states for lattices sizes up to $L = 3000$ were calculated. The results show that both exact and quasi-exact algorithms are in a very good agreement. Finally, by using the combination of these algorithms, high precision estimates of the spin stiffness exponent θ and domain wall fractal dimension d_f for Gaussian bond distribution are obtained.
Note that the bulk of the present chapter has been previously published in Ref. [53].

[1] It should be mentioned that systems with periodic boundary conditions have been studied using other methods but they are restricted to only small system sizes due to the exponential growth of computational time with the system size. See, e.g., Ref. [113].

3.2 Matching Kasteleyn cities for spin-glass ground states

In this section, we are going to explain the main idea of how we can find the ground state of two-dimensional Ising spin-glass systems by mapping them to a matching problem. We will first introduce matchings in mathematics, and some of their properties. We then show how one can construct a dual graph for a given Ising spin glass system and solve the matching problem on this dual graph in order to find the ground state of the original system.

3.2.1 Matching problem

Consider a graph G with a set of vertices V and a set of edges E, i.e. $G = (V, E)$. A *matching* M on graph G is a subset of edges in which no two edges share a common vertex (Fig. 3.1). A vertex is *matched* if it is an endpoint of one of the edges in the matching. Otherwise the vertex is *unmatched*.

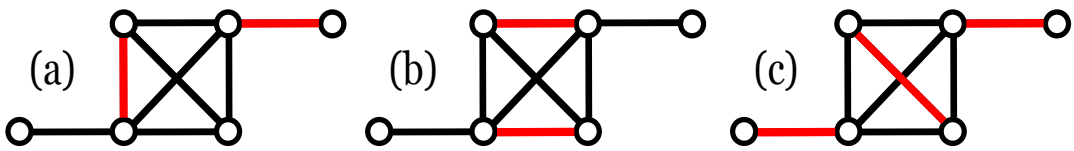

Figure 3.1: Schematic sketch of the matching problem. (a) a matching on a graph G, (b) a maximal matching and (c) a perfect matching on the same graph.

In this context, we can define some special cases for matching:

Maximal matching: A maximal matching is a matching M of a graph G with the property that if any edge not in M is added to M, it is no longer a matching. Figure 3.1 (b) shows an example of a maximal matching.

Perfect matching: A perfect matching M on a graph G is a matching in which all the vertices in V contribute to the matching. In other words, a matching M is perfect if every vertex of a graph G is connected to exactly one other vertex by the matching. Figure 3.1 (c) shows an example of a perfect matching.

Maximum (minimum) weight matching: If a graph G is weighted then a matching M is maximum (minimum) weight if the sum of the values of the edges in the matching have a maximal (minimal) value.

Maximum (minimum) weight perfect matching: A matching M on a weighted graph G is a maximum (minimum) weight perfect matching if it matches all vertices in the graph in such a way that the sum of the edges in the matching

have a maximal (minimal) value. In the next subsection we will see that the minimum energy of a two-dimensional Ising spin glass system can be related to a minimum-weight perfect matching problem on a dual graph.

3.2.2 Combination of Kasteleyn cities with the minimum-weight perfect matching

We are now going to introduce a fast algorithm for determining the ground state of the two-dimensional Ising spin glass systems which is based on the combination of Kasteleyn cities (a Kasteleyn city is a complete graph with four nodes[2] [114]) with the minimum-weight perfect matching problem [113, 21]. The main idea of this algorithm is as follows:

We consider an Ising spin glass in the Edwards-Anderson (EA) model. The Hamiltonian of the system is given by

$$H = -\sum_{\langle i,j \rangle} J_{ij} S_i S_j \tag{3.2.1}$$

where the sum runs over all nearest-neighbor sites of a lattice, the spins, S_i are $+1$ or -1 (up or down), and the coupling J_{ij} is a random variable chosen from a Gaussian or bimodal distribution. Imagine we have already calculated the ground state of the system. If we look at the ground state spin configuration, we will see that the ground state can be considered as a sea of up spins ($\uparrow$) in which there are some islands of down spins ($\downarrow$), or vice versa (Fig. 3.2). The summation over all nearest neighbors can then be divided into a sum over all parallel spins ($s_i \parallel s_j$), and a sum over all antiparallel spins at the boundaries of the islands ($s_i \nparallel s_j$). Now the energy can be written as:

$$\begin{aligned} E &= -\sum_{<i,j>} J_{ij} s_i s_j = -\sum_{s_i \parallel s_j} J_{ij} + \sum_{s_i \nparallel s_j} J_{ij} \\ &= -\sum_{s_i \parallel s_j} J_{ij} + \sum_{s_i \nparallel s_j} J_{ij} + \sum_{s_i \nparallel s_j} J_{ij} - \sum_{s_i \nparallel s_j} J_{ij} \\ &= -\sum_{<i,j>} J_{ij} + 2 \sum_{s_i \nparallel s_j} J_{ij}, \end{aligned} \tag{3.2.2}$$

which means the energy of the system is just a constant (sum over all bonds) plus two times the sum of the bonds at the boundaries of those islands. Indeed finding the ground state of the system is equivalent to finding such boundaries in which

[2] A complete graph is a simple undirected graph in which every pair of distinct vertices is connected by a unique edge

the second term of the above equation becomes minimum. Now we only need to find a way to actually determine those boundaries!

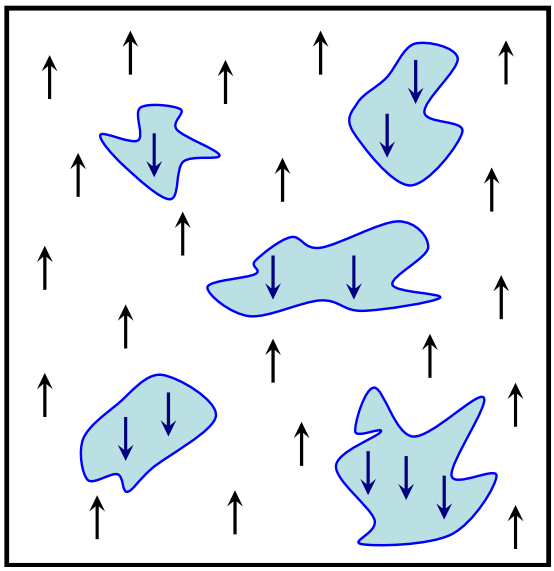

Figure 3.2: Schematic view of the ground state of a two-dimensional Ising spin glass. The ground state can be considered as a sea of up spins (↑) in which there are some islands of down spins (↓).

Thomas and Middleton suggested in [113] that for a given spin-glass system of size $L \times L$ and bond configuration $\{J_{ij}\}$ with open boundary conditions in both directions, we construct a dual lattice. The dual lattice $D = (V, E)$ has $(L+1)\times(L+1)$ nodes. The edge e_{ij} of the dual lattice crosses the bond (i, j) of the original lattice and has the weight $w(e_{ij}) = J_{ij}$. The outer edges which do not cross the original bonds have zero weight. We then replace every node in D by one Kasteleyn city with zero weight edges. Therefore the new graph G with Kasteleyn cities has $4 \times (L+1) \times (L+1)$ nodes and $6(L+1)^2 + 2L(L+1) = 8L^2 + 14L + 6$ edges. Then a minimum-weight perfect matching problem is solved on this graph[3]. We use a new implementation for calculation of the minimum-weight perfect matchings (MWPM), Blossom V as introduced in [115], in our calculations. After the solution of MWPM on graph G is found, all the Kasteleyn cities are shrunk to one node. The result will be a set of negative weight loops (boundaries of spin down islands) in D with the most negative total weight, which indeed results in the minimum energy of the system. The ground state energy is then the sum of all bonds plus the sum of all these negative loops. Finally the ground state spin configuration of the system can be found easily by scanning across the system: since these loops are the boundaries of antiparallel spins, we can start from one of the spins of the system

[3] It is known that the solution of the minimum-weight perfect matching can be obtained in a polynomial time [115].

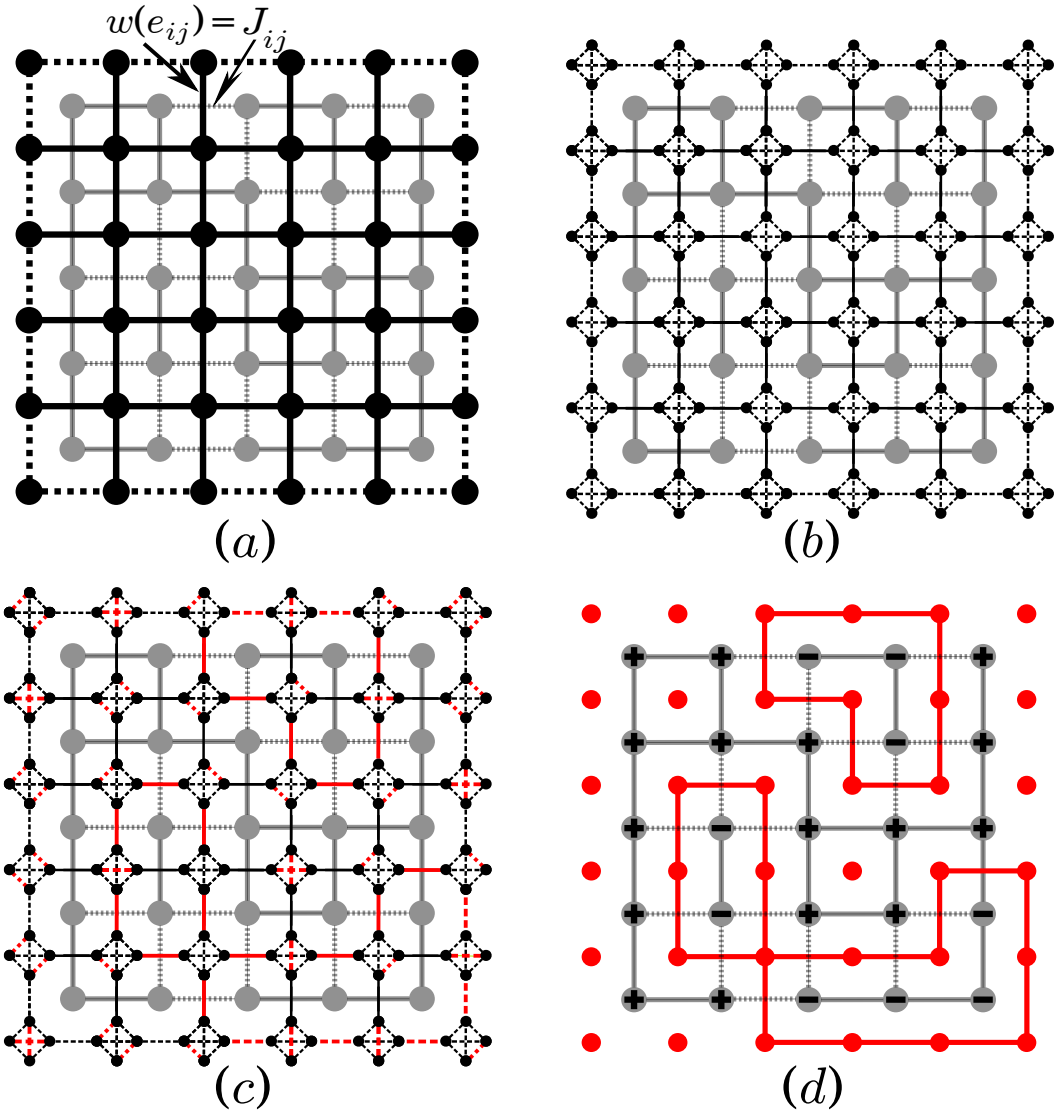

Figure 3.3: An outline of the steps that convert a spin glass system first to the dual weighted lattice D and then to the weighted graph G with Kasteleyn cities, in order to compute the ground state of the original lattice. (a) The original spin glass system is shown by gray dots and lines. Gray solid lines correspond to ferromagnetic bonds of the original sytem $J_{ij} > 0$, while gray dashed lines to antiferromagnetic ones, $J_{ij} < 0$. Black dots and line show the dual lattice D. The edge e_{ij} of the dual lattice crosses the bond (i, j) of the original lattice and has the weight $w(e_{ij}) = J_{ij}$. The black dashed lines represent the edges with zero weight. (b) The vertices in D are replaced by Kasteleyn cities (dashed lines have zero weight in G). (c) The minimum-weight perfect matching M on graph G is shown. Red lines indicate the edges of M. (d) The the Kasteleyn cities will be shrunk to a single node and loops of negative weights appear. Red dots show the vertices of D and red lines indicate the edges of M. In this example, we set the orientation of the most left top spin as +1 and go through the original lattice to set other site's spin value. Every time we cross a red line the spin will be flipped.

and choose an orientation for that. Then we go through the sites of the original lattice one by one and associate them with the same orientation until we cross one of boundaries of antiparallel spins (solutions of MWPM) on the dual lattice where we need to flip the spins because we are in the island of the opposite spins. We keep doing that until the orientation of all the spins becomes determined. A schematic view of the whole procedure for this algorithm is shown in Fig. 3.3. This method can be easily generalized to other planar graphs, for instance $L \times L$ graphs with periodic boundaries in one direction. In this case, one additional line of external nodes in either the horizontal or vertical direction can be removed, otherwise the algorithm proceeds in the same way.

This is a very efficient algorithm to determine the ground state energy of the two-dimensional Ising spin glass (2DISG) system with at least one open boundary. It is faster than Bieche's algorithm [82] and needs less memory to implement. This is due to the fact that here the number of nodes as well as the number of edges of the graph G are the same order as L^2, while in Bieche's algorithm we need to consider a complete graph of the order L^2 and the number of edges is of the order L^4. However as soon as periodic boundary conditions are applied in both directions the algorithm fails. Because sometimes MWPM gives us a loop wrapping around the system and makes an inconsistency between the right and the left side of the loop. Since finite size effects are much smaller in those systems it is very important to have an algorithm which enables us to calculate the ground state of systems with fully periodic boundary conditions. In the next section we will present a new algorithm for calculating the ground state of the 2DISG with periodic-periodic boundary conditions which is based on the combination of MWPMP and windowing technique.

3.3 Windowing technique (WT) for toroidal systems

3.3.1 WT algorithm

Although the matching approach does not work for periodic-periodic boundaries, where finite size corrections are expected to be smaller, using a windowing technique allows us to determine quasi-exact ground states for systems with fully periodic boundary conditions. In this technique, for a given spin glass system in two dimensions of size L with fully periodic boundary conditions, an initial random spin configuration $\{s_i\}$ is chosen. A window of size $L'(L' < L)$ is considered with open boundary conditions in both directions and the exact ground state for the spins inside the window is found (using the MWPM technique), with the added constraint that the spins near the boundaries of the window have the correct orientation with respect to the exact ground state spin configuration, so they

remain unchanged. This technique locally minimizes the energy of the window, as well as decreasing the total energy of the system. By moving this window over the full $L \times L$ lattice, the exact ground state is typically found after a moderate number of iterations.

The above constraint is imposed by changing the couplings between all of the lattice sites at the two sides of the boundaries of the window such that the orientations of their spins remains unchanged when MWPM is implemented on the dual lattice. This can be done by placing very strong bonds with couplings J_{strong} between them that cannot be broken in the solution of the MWPM, for instance by choosing $|J_{\text{strong}}| > \sum_{\langle ij \rangle} |J_{ij}|$. We choose $J_{ij} = +|J_{\text{strong}}|$ for parallel spins along the boundary of the window and $J_{ij} = -|J_{\text{strong}}|$ for antiparallel ones to ensure that these spins do not change their relative orientation as a result of the MWPM run. This setup is illustrated in Fig. 3.4. A new position for the window is then chosen at random, and the procedure is repeated. As the spins at window boundaries are fixed and the resulting constraint optimization problem is solved exactly, each iteration of the windowing method decreases the total energy of the system or leaves it invariant. We expect that after some iterations of this technique, the total energy would no longer change; at which point that the ground state of the system has been found. We observe convergence of the method after a moderate number n of iterations. The process is shown in Fig. 3.5, where we display the overlap $s_i s_i^0$ with the exact ground state s_i^0 for an example disorder configuration of size $L = 200$ with Gaussian couplings starting from a random initial spin configuration. It is seen how even the first optimization with a window of size $L' = L - 2$ leaves only a single (large) cluster excitation over the ground state. As is seen from the following panels, such excitations can only be fully relaxed if the window does not intersect them. Hence the time until convergence is a random variable.

Before using this technique, firstly the size of the window, L', must be chosen. The number of iterations n also plays an important role in this technique. To determine a good set of parameters we performed test runs for different sizes L and L' of the system and the window, respectively, and with a varying number of iterations. The results show that the necessary number of iterations depend on both L' and the initial spin configuration such that a larger L' value needs a smaller n value, and if the initial spin configuration is changed, n will also change. Since the ground state of the whole system needs to be found, it seems to be clear that a larger L' would find the ground state more easily. As is intuitively plausible, we find best results for the largest windows, and so we fixed the window size to its maximum $L' = L - 2$ for all runs.

According to our results, although the initial spin configurations are chosen randomly, for some configurations the final state is found more quickly than for

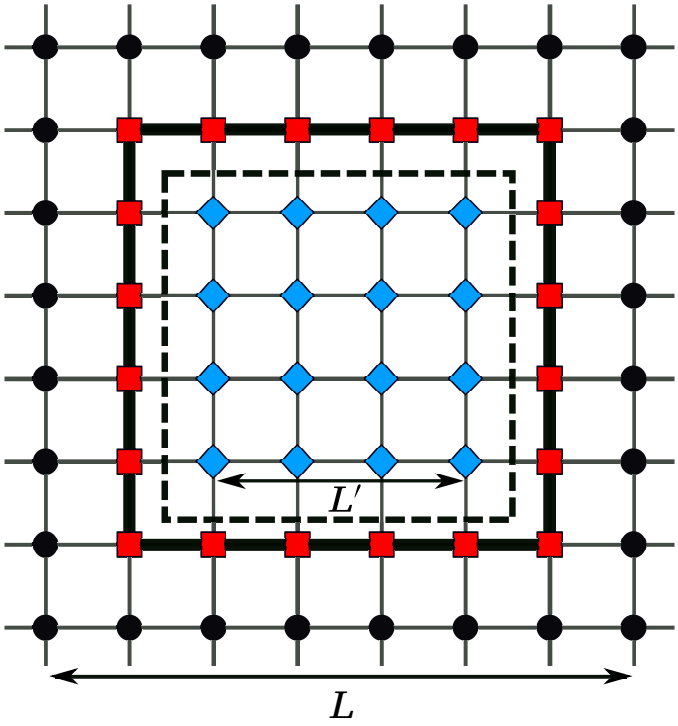

Figure 3.4: Schematic representation of the windowing technique to determine ground states for toroidal systems. The dashed square shows the window and the blue diamonds represent the sites whose spins will be updated next by the windowing technique, as they are contained within the current window. Red squares indicate sites whose spins are fixed in their current orientation with strong bonds, indicated by the thick black lines. As a result, the MWPM problem will be solved for the system of red and blue spins with using free boundary conditions.

others, whilst for some of them the correct ground state is never reached. To decide whether a given run arrives in the correct ground state, we compared our results against exact results for system sizes $L \leq 100$ produced by the branch-and-cut method implemented in the spin-glass server at the University of Cologne [116]. Therefore we are able to find out that for a fixed n, how many different initial spin configurations considered in the WT technique have ended up yielding the exact ground state. For $L \geq 150$ it is not possible to find the exact ground state in a reasonable time using the spin-glass server. Therefore instead of comparing to the exact ground states, we have considered more (independent) initial spin configurations and the quasi-exact ground state energy is calculated for each of them; the minimum quasi-exact ground state energy is then considered as the correct ground state energy, and it is enumerated how many times this minimum energy has been found.

Table 3.1 shows the success probability $P_n(\{J_{ij}\})$ of reaching the ground state for different numbers of iterations for $20 \leq L \leq 1000$ and averaged over 100 different

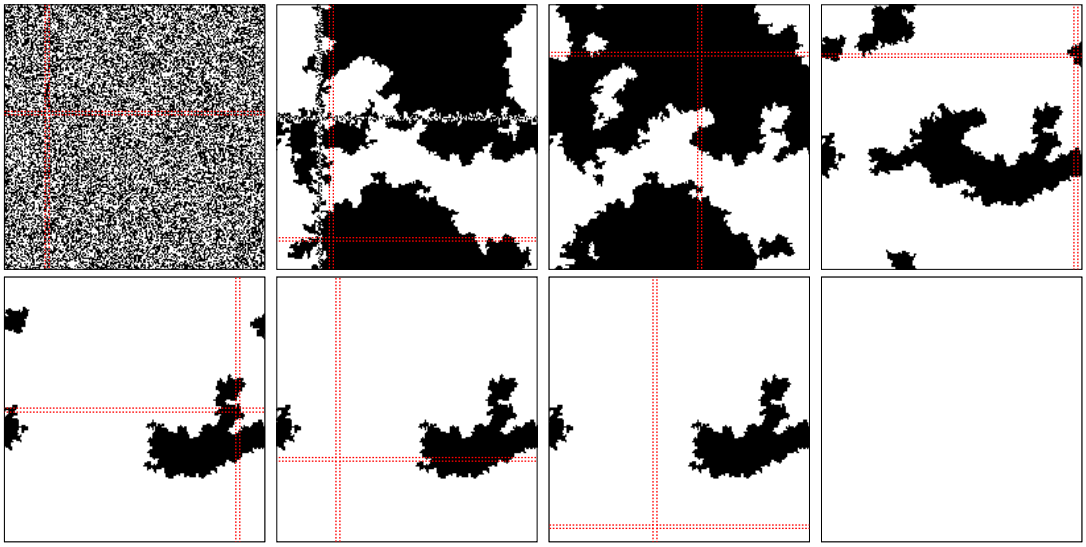

Figure 3.5: Application of the windowing method to find a ground state of a sample with toroidal boundaries. Spins on white lattice sites are consistent with the ground-state orientation s_i^0, i.e., $s_i s_i^0 = +1$, black spins are oppositely oriented, i.e., $s_i s_i^0 = -1$. In a random initial configuration the spins have $s_i s_i^0 = \pm 1$ uniformly at random (top left). Exact ground states are found in windows of size $(L-2)\times(L-2)$ placed at a random location (red dotted lines), with the remaining spins acting as fixed boundaries. After a few iterations all spins have the ground-state orientation (bottom right).

disorder realizations. The number of independent initial spin configurations varies between 2000 for system sizes $L \leq 150$ and 250 for $L \geq 700$. As is clearly seen, the success probabilities are quite high such that for $n = 20$, for instance, they are consistently above 70%. There is almost no size dependence of the average success probability $\overline{P}_n$, so the hardness of finding ground states for the fully periodic torus lattices with the proposed method does not increase with system size. Still, from the data presented in Table 3.1, it is clear that not every run of the windowing method converges to the ground state.

To further increase the success probability of the method, we use repeated runs and pick the lowest energy found there [117]. If the success probability for a given sample in runs of n iterations is $P_n(\{J_{ij}\})$, then the probability of finding the ground state at least once in m independent runs is

$$P_s(\{J_{ij}\}) = 1 - [1 - P_n(\{J_{ij}\})]^m, \tag{3.3.1}$$

and this can be tuned arbitrarily close to unity by increasing m. If we set a desired success probability of, say, $P_s = 0.999$, we can use Eq. (3.3.1) to determine the required number m of repetitions. For each realization we hence find

$$m(\{J_{ij}\}) = \log[1 - P_s]/\log[1 - P_n(\{J_{ij}\})].$$

Table 3.1: The average probability $\overline{P}_n$ of finding the ground state (success probability) for $20 \leq L \leq 1000$, and for different numbers n of iterations. Results are averaged over 100 disorder realizations.

$L\backslash n$	5	10	15	20	25	30
20	0.276	0.561	0.671	0.728	0.762	0.782
50	0.317	0.603	0.705	0.756	0.790	0.805
80	0.315	0.592	0.700	0.752	0.783	0.806
100	0.315	0.594	0.700	0.745	0.779	0.789
150	0.326	0.611	0.714	0.768	0.797	0.821
200	0.323	0.610	0.712	0.765	0.792	0.814
350	0.340	0.628	0.729	0.789	0.822	0.833
500	0.317	0.589	0.683	0.740	0.771	0.801
700	0.329	0.612	0.723	0.770	0.782	0.818
1000	0.322	0.609	0.713	0.764	0.779	0.807

In Table 3.2 we show the values of $\overline{m}$ averaged over 100 disorder realizations as a function of L and n. Clearly, the dependence on system size is weak. The total computational effort of such repeated runs is proportional to $m \times n$. From the values of n tested in Table 3.2, this effort is found to be minimal for $n = 10$, and we use $m = 8$ repetitions independent of system size to find the exact ground state in approximately 99.9% of the samples. As an additional protection against potential outliers we demand that the lowest-energy state found in these $m = 8$ runs must have occurred at least three out of these 8 times. If this is not the case, another 8 runs are performed etc. This adds only a tiny fraction of extra average runtime, but it will be able to catch a few of the 0.1% of samples where the ground state would otherwise not be found. As a test, we applied this combined technique to the samples for $L \leq 100$ where the exact ground-state energy is known and it arrived in a ground state in all cases.

3.3.2 Performance of the WT algorithm

It is interesting to see how the matching based on Kasteleyn cities for planar instances as well as the windowing method outlined above for toroidal graphs fare in computational efficiency as compared to the more general approaches implemented in the spin-glass server [116]. The run times of the matching based algorithms in seconds on standard hardware are shown for periodic-free boundary conditions (PFBC) and for periodic-periodic (toroidal) boundaries (PPBC), as compared to the corresponding results of the spin-glass server for system sizes $L \leq 100$ in Table 3.3. For PFBC the matching approach is always much faster than the method used by the spin-glass server, which is based on a modified exact numeration technique known as branch-and-cut. For PPBC the windowing

Table 3.2: The average number $\overline{m}$ of repetitions required according to Eq. (3.3.1) for runs of the windowing technique with n random placements of the window per run to ensure an overall success probably of $P_s = 0.999$.

$L\backslash n$	5	10	15	20	25	30
20	23.5	9.3	6.9	5.8	5.3	4.9
50	19.7	8.2	6.2	5.3	4.7	4.5
80	20.2	8.6	6.4	5.4	4.9	4.4
100	20.0	8.5	6.4	5.6	4.9	4.5
150	19.2	8.1	6.0	5.0	4.5	4.0
200	19.2	8.3	6.1	5.3	4.7	3.6
350	18.4	7.4	5.8	4.8	3.9	3.8
500	21.2	8.5	7.0	6.0	5.0	4.6
700	20.3	7.9	6.3	5.8	4.6	5.0
1000	20.0	8.5	6.4	5.1	5.0	4.5

technique introduces a certain overhead, such that a crossover is observed with branch-and-cut being faster for $L \lesssim 20$ and the windowing method winning out for $L \gtrsim 20$.

The scaling of run times with system size is illustrated in Fig. 3.6. The algorithm of the spin-glass server utilized here is based on branch-and-cut [118], which corresponds to a combination of a cutting plane technique with the iterative removal of branches of the search tree that cannot contain a solution. While this approach is quite efficient, and outperforms other exact methods for hard problems, its run-time still scales exponentially with system size. The super-polynomial behavior is clearly seen in the doubly logarithmic representation of Fig. 3.6. For the matching approach for PFBC, the implementation used here has $O(L^6)$ worst-case scaling [115]. As the straight line indicates, we indeed see clear power-law behavior, but the average run times probed here increase much more gently with system size. A power-law fit of the form

$$t(L) = A_t L^{\epsilon} \tag{3.3.2}$$

to the data yields $\epsilon = 2.22(2)$, so the scaling is only slightly worse than linear in the volume in the considered range of system sizes.

Finally, for the windowing technique built on top of MWPM for the PPBC samples, we find an overhead, that is to a very good approximation independent of system size, such that calculations for PPBC are by a factor of 80 more expensive than those for samples with PFBC for the chosen confidence level of $P_s = 0.999$, corresponding to the $n = 10$ iterations and $m = 8$ repetitions. A fit of the form

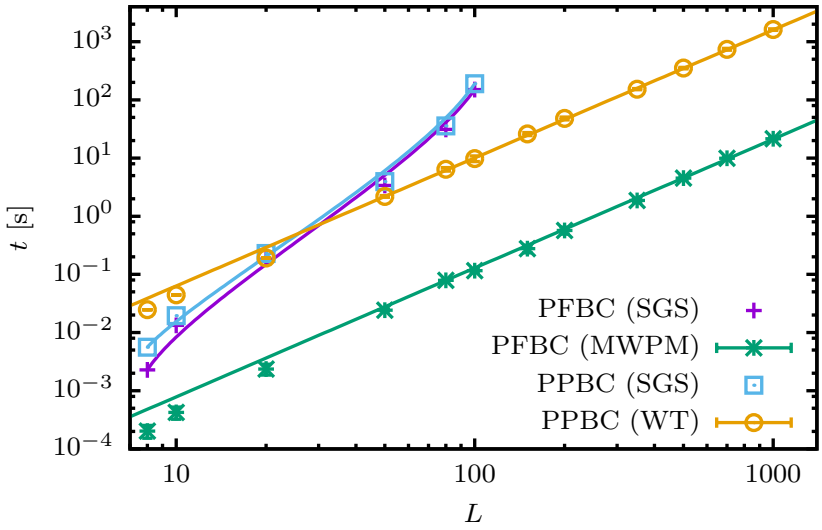

Figure 3.6: Average time t per sample to determine ground states of systems with PFBC and PPBC for $L \times L$ samples using the minimum-weight perfect matching (MWPM) method for periodic-free samples (PFBC), the windowing technique (WT) for periodic-periodic samples (PPBC), and the spin-glass server (SGS), respectively. The straight lines are fits of the form (3.3.2) to the data, whereas the lines for the SGS data are just interpolations to guide the eye.

(3.3.2) to the data for PPBC yields $\epsilon = 2.20(2)$, perfectly consistent with the results for PFBC. The ratio of amplitudes A_t is estimated as $A_t = 83 \pm 12$, consistent with the expected value of slightly above 80 resulting from the additional requirement of a threefold occurrence of the ground state.

3.4 Results for Gaussian couplings

For the Gaussian distribution (1.3.2) the set of couplings for which exact degeneracies occur is expected to be of zero measure. The present techniques based on matching hence directly yield the correct distribution of states at zero temperature. The ground state of systems with bimodal couplings (1.3.3), however, is hugely degenerate and the matching-based algorithms give us only one of the ground-state spin configurations. Although there are some techniques to generate more than one spin configuration by matching-based algorithms (for instance by adding small random noise to all the couplings), they do not generate the ground states in a uniform fashion resulting in a non-correct distribution of states at zero temperature for $\pm J$ couplings. In this section, we only present the results for system with Gaussian bond distribution. The results for bimodal couplings will be shown in chapter 4 where we present a new algorithm to sample the ground state of these systems uniformly.

Table 3.3: Average run time (in seconds) for determining a ground state of samples with periodic-free boundaries (PFBC) and periodic-periodic boundaries (PPBC), respectively, using the minimum-weight perfect matching (MWPM) approach based on Kasteleyn cities for PFBC and the windowing technique (WT) for PPBC as compared to the times reported by the spin-glass server (SGS) on the same samples.

L	PFBCs		PPBCs	
	SGS	MWPM	SGS	WT
8	0.00228	0.000203	0.00560	0.02468
10	0.01330	0.000424	0.01950	0.04462
20	0.18330	0.002361	0.22820	0.19119
50	3.38740	0.024184	3.93040	2.18788
80	31.0738	0.069104	35.7004	6.42005
100	150.218	0.115761	189.501	9.81247

3.4.1 Ground-state energies

The average ground-state energy per spin, $\langle e(L)\rangle_J$, depends on the coupling distribution. Additionally, we expect finite-size corrections which in turn are sensitive to the boundary conditions employed [119, 120, 121]. Following Ref. [120], one expects a Wegner correction exponent $\omega(d) = (6-d)+\cdots$ to leading order, whereas numerically one finds [22] $\omega \approx 1.0$ for Ising spin glasses in $d = 3$ and $\omega \approx 0.75$ for $d = 2$ [80]. As then $-(d-\theta)+\omega \approx -3.03$ in two dimensions, this implies that non-analytic corrections are substantially suppressed against the leading analytic ones in this quantity. We hence assume the following general form for the size dependence of the average ground-state energy,

$$\langle e(L)\rangle_J = e_\infty + A_E L^{-(d-\theta)} + C_E L^{-1} + D_E L^{-2} + E_E L^{-3} + \ldots. \tag{3.4.1}$$

The presence of a term proportional to $L^{-(d-\theta)}$ follows from standard arguments about the scaling of the correlation length and the free-energy density [122], taking additionally into account that for a $T = 0$ critical point the $1/\beta^2$ prefactor in the relation $e = (-1/\beta^2)\,\mathrm{d}(\beta f)/\mathrm{d}T$ is critical, as well as making use of the relation $\nu = -1/\theta$ [120]. Although this derivation should apply for any $T = 0$ critical point, for the spin glass it is tempting to attribute the occurrence of the $L^{d-\theta}$ term to the presence of domain-wall defects that are trapped in the system due to periodic boundary conditions. In Ref. [120] it is suggested that the number of parameters in Eq. (3.4.1) can be reduced by considering the energy $\hat{e}(L)$ per bond, instead of the energy $e(L)$ per site. If one assumes that depending on the boundary conditions this quantity has a $1/L$ correction for any free edge and a $1/L^2$ correction for any

corner, for the square lattice with its two bonds per site we expect

$$2\langle\hat{e}(L)\rangle_J = e_\infty + \hat{A}_E L^{-(d-\theta)} + \hat{C}_E L^{-1} + \hat{D}_E L^{-2},$$

up to higher-order corrections. For free-free boundaries, one has $E(L) = L^2 e(L) = (2L^2 - 2L)\hat{e}(L)$ and hence

$$\langle e(L)\rangle_J = e_\infty + \hat{A}_E L^{-(d-\theta)} + (\hat{C}_E - e_\infty)L^{-1} + (\hat{D}_E - \hat{C}_E)L^{-2} - \hat{D}_E L^{-3}, \tag{3.4.2}$$

where a term of order $L^{-(d-\theta)-1}$ which for $\theta < 0$ is asymptotically smaller than $1/L^3$ has been neglected. This is of the form of Eq. (3.4.1), but with the $1/L^3$ term merely being produced by the $1/L^2$ correction in $\hat{e}(L)$, such that there are only five fit parameters in (3.4.2) as compared to six parameters in Eq. (3.4.1). For periodic-free boundaries there is a free edge but no corners, such that $\hat{D}_E = 0$ and $E(L) = (2L^2 - L)\hat{e}(L) = L^2 e(L)$, and we find

$$\langle e(L)\rangle_J = e_\infty + \hat{A}_E L^{-(d-\theta)} + (\hat{C}_E - e_\infty/2)L^{-1} - (\hat{C}_E/2)L^{-2}, \tag{3.4.3}$$

where again a term proportional to $L^{-(d-\theta)-1}$ was omitted. For periodic-periodic boundaries, on the other hand, one should have $\hat{C}_E = 0 = \hat{D}_E$, and hence only a correction proportional to $L^{-(d-\theta)}$. We will test the validity of these assumptions for our data below.

Beyond the mean ground-state energy, it is interesting to study the shape of the energy distribution over different disorder samples. It has been shown in Ref. [119], based on results of Wehr and Aizenman [123], that the width of this distribution scales as L^{Θ_f} with $\Theta_f = -d/2$. Below, we investigate the distribution shape by direct inspection and by analyzing the scaling of its kurtosis defined by

$$\mathrm{Kurt}[e] = \frac{\langle(e - \langle e\rangle_J)^4\rangle_J}{[\langle(e - \langle e\rangle_J)^2\rangle_J]^2} \tag{3.4.4}$$

with system size, where $\mathrm{Kurt}[\cdot] = 3$ for a Gaussian distribution.

3.4.2 Domain-wall calculations

As we have seen in Chapter 1, introducing the domain walls into the system by changing the boundary conditions and the analysis of defect energies provides a convenient way of studying the stability of the ordered phase. The conceptually most direct way of inserting a domain-wall excitation is to compute a ground-state for free boundaries in, say, the x direction as a reference and to then fix the boundary spins along the x boundary in opposite relative orientations as compared to this state for a second ground-state calculation. The excess energy

in the second run corresponds to the energy contained in the domain wall. This setup is sometimes referred to as domain-wall boundary condition [75, 124]. An alternative proposed initially by Banavar [125] uses the difference between the ground-state energies for periodic and for antiperiodic boundaries in x direction. This can be done by multiplying all the horizontal couplings of one of the vertical columns of the system by -1. The resulting value of $\Delta E = E_{\mathrm{P}} - E_{\mathrm{AP}}$ is actually the difference of energies of two configurations with such domain walls as the periodicity of both P and AP boundaries forces a domain wall into the system [126, 127] which scales as $|\Delta E| \sim L^{\theta}$; but this difference is found to nevertheless scales with the same stiffness exponent as for domain-wall boundaries [124].

For calculations based on MWPM alone one needs to apply free boundaries in y direction in order to ensure planarity of the lattice. With the help of the windowing technique it is also possible to implement this procedure for samples with periodic-periodic boundaries, however. In general we expect the leading scaling to be accompanied by scaling corrections of the form [121]

$$\langle |\Delta E(L)| \rangle_J(L) = A_\theta L^\theta (1 + B_\theta L^{-\omega}) + \frac{C_\theta}{L} + \frac{D_\theta}{L^2} + \cdots , \tag{3.4.5}$$

where ω denotes the leading corrections-to-scaling exponent, and $1/L$ and $1/L^2$ are leading analytic corrections [122]. For the setup with domain-wall boundary conditions significantly stronger corrections have been observed than for the P-AP situation [124] and we hence concentrate on the latter approach here. As we shall see below, we find reduced scaling corrections for the fully periodic samples, and in particular the $1/L$ term relating to the presence of free boundaries is absent there.

Apart from the energy density of domain walls (or droplet boundaries) and the stiffness exponent, another interesting quantity is the length of domain walls because it determines the corresponding fractal dimension of the domain walls. We determined the domain wall as the set $\mathcal{D}$ of all dual bonds for which

$$[J_{ij} s_i s_j]^{(\mathrm{P})} [J_{ij} s_i s_j]^{(\mathrm{AP})} < 0. \tag{3.4.6}$$

The inclusion of the couplings J_{ij} in the product takes care of the fact that across the edge where the boundary condition is changed from P to AP the spins will be in different relative orientation before and after the change, but this is merely a consequence of the flip $J_{ij} \to -J_{ij}$ of the couplings there and should not be counted as a part of the induced domain wall. We denote by ℓ the number of (dual) edges in the set $\mathcal{D}$. Following the usual box-counting argument, scaling according to $\langle \ell \rangle_J \sim L^{d_{\mathrm{f}}}$ defines the domain-wall fractal dimension d_{f}. As for the defect energies

Table 3.4: The number of disorder realizations for different boundary conditions, coupling distributions and system sizes.

L	PFBC Gaussian	PPBC Gaussian	PFBC bimodal
8	1×10^6	1×10^5	1×10^5
10	1×10^6	1×10^5	1×10^5
20	1×10^6	1×10^5	1×10^5
30	1×10^6	1×10^5	1×10^5
40	1×10^6	1×10^5	1×10^5
50	1×10^6	1×10^5	1×10^5
80	1×10^6	8×10^4	1×10^5
100	1×10^6	8×10^4	1×10^5
150	1×10^6	1×10^5	1×10^5
200	1×10^6	5×10^4	8×10^4
350	5×10^5	5×10^4	8×10^4
500	5×10^5	3×10^4	5×10^4
700	5×10^5	1×10^4	3×10^4
1000	3×10^5	1×10^4	1×10^4
1500	1×10^5	7×10^3	5×10^3
2000	5×10^4	1×10^3	3×10^3
3000	3×10^4	640	1505
4000	2×10^4		
5000	3×10^3		
7000	400		
8000	455		
10000	265		

we anticipate the presence of corrections, leading to the scaling form

$$\langle \ell \rangle_J(L) = A_\ell L^{d_f}(1 + B_\ell L^{-\omega}) + \frac{C_\ell}{L} + \frac{D_\ell}{L^2} + \cdots . \tag{3.4.7}$$

3.4.3 Periodic-free boundaries

For the periodic-free setup (PFBC) we used the MWPM approach for periodic and antiperiodic boundaries in x direction and system sizes ranging from $L = 8$ up to $L = 10\,000$. For $L \leq 350$ we generated 10^6 disorder configurations, while for larger systems the number of replicas is gradually reduced down to about 300 for $L = 10\,000$, see the details collected in Table 3.4. We used the MIXMAX random number generator [128, 129] which has provably good statistical properties and also passes all of the tests in the suite TestU01 [130]. As an additional check in view of the high precision nature of the present study, a part of our calculations was repeated with Mersenne twister [131]. All results were found to be perfectly consistent within error bars.

We start by considering the ground-state energies. Here, we use the results for both P and AP boundary conditions. They differ from each other, on average, by far less than the statistical errors would suggest, but this is due to the fact that for each sample both energies are highly correlated. For studying the average ground-state energy, we hence calculated the average $\bar{E} = (E_{\mathrm{P}} + E_{\mathrm{AP}})/2$ and estimated statistical errors for $\langle \bar{E} \rangle_J$ through the variation over disorder samples. As the data in panel (a) of Fig. 3.7 show, the finite-size corrections to scaling are relatively small, with the result for $L = 10$ only being about 4% above the asymptotic value. Due to the large range of system sizes and high statistics in disorder samples we get a stable result for the full non-linear five parameter fit of the form (3.4.3) to the data with a quality-of-fit[4] of $Q = 0.81$. For the asymptotic ground-state energy we find

$$e_\infty = -1.314\,787\,6(7),$$

while the spin-stiffness exponent $\theta = -0.273(65)$ from this fit[5]. If we fix θ at the value $\theta = -0.2793$ found below from the defect energy calculations for the PFBC boundaries, the asymptotic ground-state estimate e_∞ is unaltered from the above value up to the given number of digits.

Our data for the defect energies are shown in Fig. 3.7(b). We find scaling corrections to be small and a pure power-law fit without corrections yields a quality-of-fit $Q = 0.37$ for $L \geq L_{\mathrm{min}} = 50$. The corresponding estimate of the stiffness exponent is $\theta = -0.2798(4)$. Corrections can hence only be resolved for $L \lesssim 50$. There, we find that the data is very well described by a single correction term proportional to $1/L^2$, cf. the inset of Fig. 3.7(b), where we show the residual contribution $\langle |\Delta E| \rangle_J - A_\theta L^\theta$ plotted against $1/L^2$. Our θ estimate from this fit is

$$\theta = -0.2793(3)$$

with $Q = 0.16$ when including all lattice sizes. Gradually increasing L_{min} does not reveal any discernible drift in the estimate for θ. Since we have one free boundary one might have expected the presence of a $1/L$ correction, which is clearly present in the ground-state energy itself according to the fit following Eq. (3.4.3). In the energy difference ΔE, however, this contribution cancels out since the couplings along the free edge are absent in both samples. If we nevertheless include such a term in the fit, its amplitude is found to be consistent with zero. We are not able to clearly resolve a Wegner correction $\propto L^{-\omega}$, which is not surprising since as discussed above we expect it to be clearly weaker than $1/L^2$.

[4] Q is the probability that a χ^2 as poor as the one observed could have occurred by chance, i.e., through random fluctuations, although the model is correct [132].

[5] Note that hence the form (3.4.3) is found to describe the data perfectly well, in contrast to the corresponding form used in Ref. [120], cf. Eq. (22) there, which is not consistent with the equation derived here.

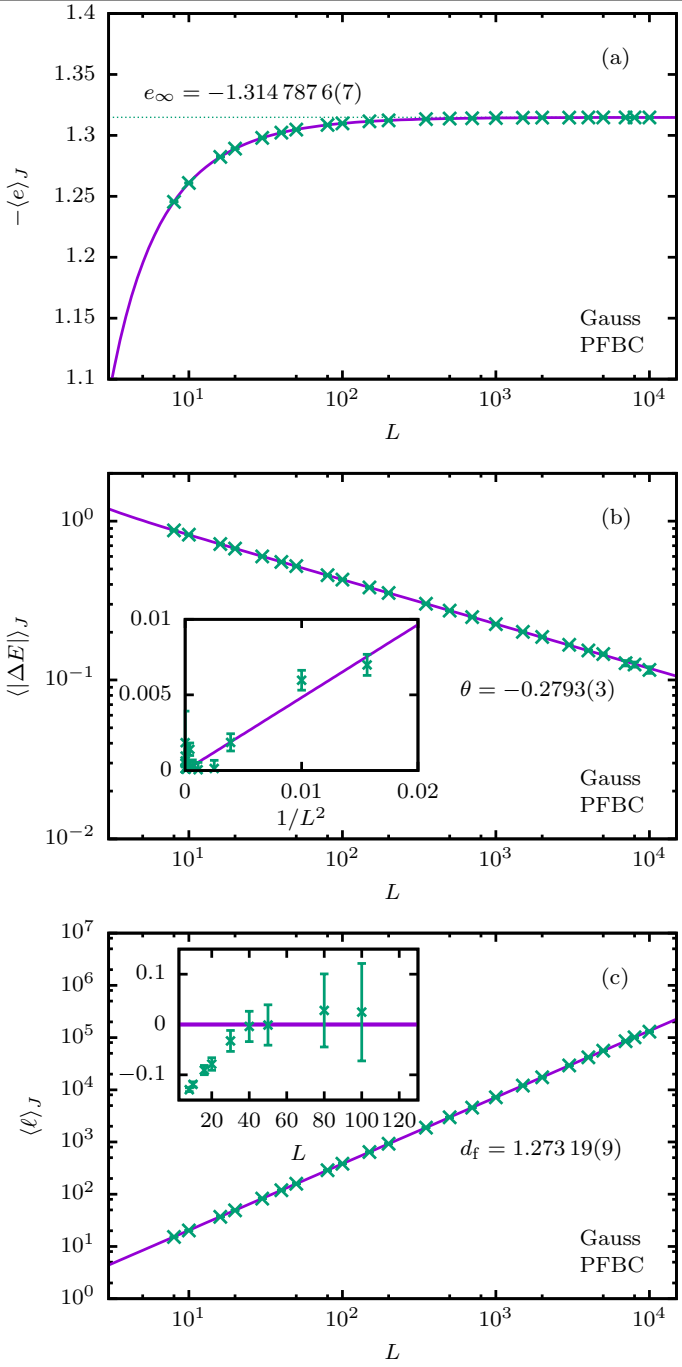

Figure 3.7: (a) Disorder-averaged ground-state energy per site $\langle e\rangle_J = \langle \bar{E}/L^2\rangle_J$ for PFBC and Gaussian couplings together with a fit of the form (3.4.3) to the data in the range $L = 10,\ldots,10\,000$. (b) Average defect energies $\langle|\Delta E|\rangle_J$ for the same system as calculated from the difference in ground-state energies between periodic and antiperiodic boundary conditions in the x direction. The points show our data for $8 \le L \le 10\,000$ and the solid line represents a fit of the form $\langle|\Delta E|\rangle_J(L) = A_\theta L^\theta + C_\theta/L^2$ to the data. The inset shows the correction $\langle|\Delta E|\rangle_J(L) - A_\theta L^\theta$ plotted against $1/L^2$ illustrating that this single term describes the corrections very well. (c) Average of the domain-wall length ℓ for the difference between the ground states for periodic and antiperiodic boundaries in x direction and free boundaries in y direction (PFBC boundaries). The line shows a fit of the functional form $\langle \ell \rangle_J = A_\ell L^{d_f}$ to the data for $L \ge L_{\min} = 40$. The inset shows a blow-up of the deviations for small L.

Table 3.5: Previous estimates of the spin-stiffness exponent θ and the fractal dimension d_f of the 2D Ising spin glass with Gaussian bound distribution.

Ref.	θ	d_f	max. system size
[133]	-0.281(5)	—	8×8
[11]	-0.285(2)	—	30×30
[134]	-0.294(9)	—	12×12
[135]	-0.29(1)	1.26(3)	120×13
[136]	-0.281(2)	1.34(10)	30×30
[75]	-0.282(2)	—	480×480
[137]	—	1.25(1)	256×256
[138]	-0.284(4)	1.273(3)	256×256
[91]	—	1.28(1)	720×360
[139]	-0.287(4)	—	16×1024
[124]	-0.282(3)	—	12×384
[120]	-0.281(7)	—	64×64
[90]	-0.285(5)	1.27(1)	300×300
[20]	-0.287(4)	1.274(2)	320×320
Our work	-0.2793(3)	1.27319(9)	$10\,000\times10\,000$

We finally turn to the domain-wall length. Fig. 3.8 shows a sample configuration with $L = 10\,000$ illustrating the meandering nature of the domain wall. For the average domain-wall length we find very clean scaling for PFBC as is seen from our data depicted in Fig. 3.7(c). A fit of the pure power-law form $\langle\ell\rangle_J = A_\ell L^{d_f}$ yields a fit quality of $Q = 0.56$ for $L_{\min} = 40$. The corresponding estimate of the fractal dimension is

$$d_f = 1.273\,19(9).$$

The deviations from a pure power law visible for system sizes $L < 20$ are rather small and not well described by a single correction term. We hence prefer to take them into account by simply omitting data from the small-L side instead of performing corrected fits. On systematically varying $L_{\min}$ in these fits, we find a drift only for $L_{\min} \leq 30$ and mutually consistent results for larger $L_{\min}$. Our results are in agreement with previous estimates shown in Table 3.5. This estimate for the fractal dimension d_f together with the estimate of the stiffness exponent θ, i.e., $\theta = -0.2793(3)$ are the most accurate values that have been reported to date.

3.4.4 Periodic-periodic boundaries

For fully periodic or toroidal boundaries (PPBC) we use the windowing technique discussed above in Sec. 3.3 to find exact ground states in more than 99.9% of the cases. Due to the increase in effort by the constant factor of 80 resulting from the windowing technique, we reduced the maximum system size a little and considered lattices in the range $8 \leq L \leq 3000$. Additionally, the number of

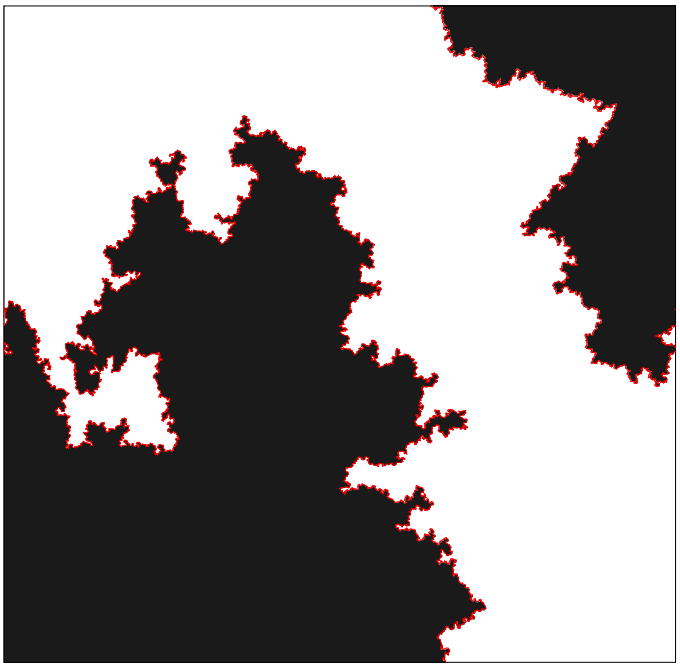

Figure 3.8: Overlap configuration of the ground states for P and AP boundaries for a $L = 10\,000$ disorder realization of the PFBC Gaussian system. The red line demarcates the domain wall which traverses $\ell = 233\,141$ dual links.

disorder realizations considered was reduced correspondingly, the exact numbers are shown in Table 3.4.

Our data for the ground-state energies for PPBC are shown in Fig. 3.9(a), illustrating that finite-size corrections in this case are tiny, even much weaker than for the PFBC case. According to the discussion above, for the ground-state energies we do not expect the presence of analytic corrections for PPBC, and so we assume a scaling form

$$\langle e \rangle_J = e_\infty + A_E L^{-(2-\theta)}. \tag{3.4.8}$$

Fits of this form work very well and yield fit qualities of $Q > 0.4$ for all $L_{\min} \geq 10$. For $L_{\min} = 16$ we find

$$e_\infty = -1.314\,788(3)$$

as well as $\theta = -0.35(14)$ and $A = 1.51(65)$ with a good $Q = 0.60$. This fit is shown together with the data in panel (a) of Fig. 3.9.

For the defect energies, the data again show clear power-law scaling with L, see Fig. 3.9(b). For $L \geq L_{\min} = 50$ we get an excellent fit ($Q = 0.74$) for the pure power-law $\langle |\Delta E| \rangle_J = A_L L^\theta$ with $\theta = -0.2778(14)$. Regarding scaling corrections, it turns out that the size range where they are visible is rather small. As the inset of Fig. 3.9(b) shows, corrections are well described by a single $1/L^2$ term, consistent with the findings for the PFBC case. A corresponding fit for $L_{\min} = 10$ yields high

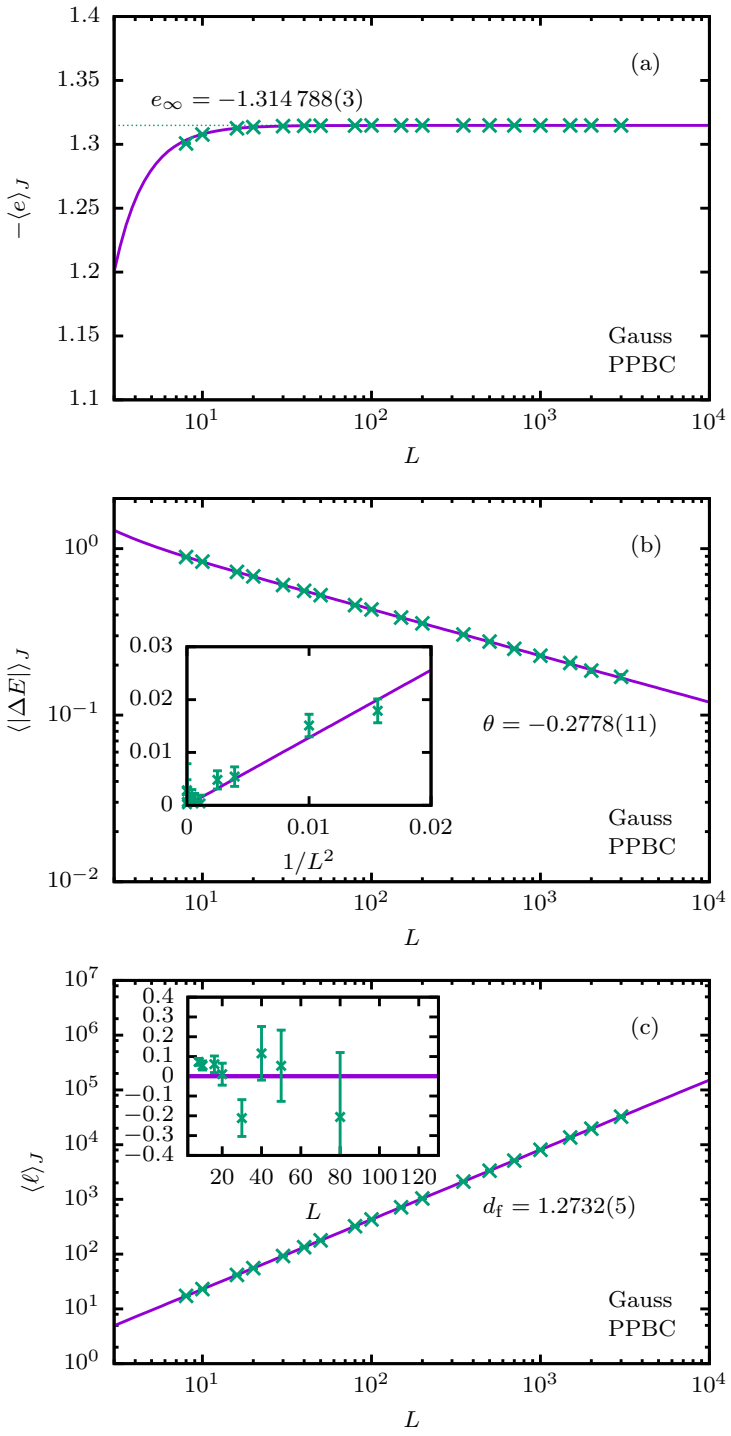

Figure 3.9: (a) Average ground-state energies for PPBC and Gaussian couplings together with a fit of the form (3.4.8) to the data in the range $L \geq L_{\min} = 10$. (b) Scaling of defect energies for the Gaussian model with fully periodic boundary conditions. The solid line shows a fit of the form $\langle|\Delta E|\rangle_J(L) = A_\theta L^\theta + C_\theta/L^2$ to the data. The inset shows the correction $\langle|\Delta E|\rangle_J(L) - A_\theta L^\theta$ plotted against $1/L^2$ illustrating that this single term describes the corrections very well. (c) Scaling of the length of the domain wall between P and AP ground states for the Gaussian PPBC case. The solid lines shows a fit of the form $\langle \ell \rangle_J = A_\ell L^{d_\mathrm{f}}$ to the data with $L_{\min} = 40$. The inset shows a detail of the main plot for small L.

quality with $Q = 0.92$ and

$$\theta = -0.2778(11).$$

A systematic trend on successively increasing $L_{\min}$ is not visible.

Regarding the domain-wall length, we again find only tiny scaling corrections, which cannot be resolved for any $L > 20$. To avoid any risk from spurious remnant corrections, we take $L_{\min} = 40$ for the uncorrected fit $\langle \ell \rangle_J = A_\ell L^{d_f}$ and arrive at

$$d_f = 1.2732(5).$$

which yields $Q = 0.73$. This fit is shown together with the data in Fig. 3.9(c). These estimates are also in agreement with previous estimates shown in Table 3.5. Comparing the results for θ and d_f between the PFBC and PPBC cases we see that they are in perfect agreement with each other, indicating that the results truly probe the asymptotic regime and acting as an *ex post* verification of the correctness of the windowing technique for the PPBC case.

3.4.5 The SLE conjecture

In 2006, Amoruso *et al.* [90] used results from stochastic Loewner evolution (SLE) to conjecture that the 2D spin glass with Gaussian couplings is described by a non-unitary conformal field theory with central charge $c < -1$, related to the SLE parameter κ as [95] $c = (6-\kappa)(3\kappa-8)/\kappa$, and they numerically determined a value $\kappa \approx 2.1$. Further, it was assumed that the scaling dimension $x_t = d - y_t = d - 1/\nu = d + \theta = 2 + \theta$ of the energy operator should be represented in the corresponding Kac table [140], and a numerically close value was found in tentatively identifying $x_t = 2\Delta_{1,2} = (6-\kappa)/\kappa$. Together with the relation $d_f = 1 + \kappa/8$ for the fractal dimension, this yields the equation [90]

$$d_f = 1 + \frac{3}{4(3+\theta)}. \tag{3.4.9}$$

We note that in addition to the assumption of a CFT representation, the identification of conformal weights with items in the Kac table is only supposed to work for rational values of κ, which does not appear to be the case here. Eq. (3.4.9) was found to be consistent with previous estimates of θ and d_f shown in Table 3.5. Here we are going to investigate the consistency of this conjecture with our accurate results. Our most accurate results are for PFBC boundaries. The corresponding estimate $d_f = 1.27319(9)$ would imply via Eq. (3.4.9) that $\theta = -0.2546(9)$ which does not seem consistent with the estimate $\theta = -0.2793(3)$ from the defect

energies. More systematically, if (3.4.9) is to hold, the difference

$$d_f - 1 - \frac{3}{4(3+\theta)} = -0.00247(9),$$

must be consistent with zero. Here, we used the estimates for d_f and θ from PFBC and standard error propagation [141]. The difference from zero corresponds to about 27 standard deviations, so based on the usual confidence limits one would need to reject the hypothesis that our data is consistent with (3.4.9). This neglects the fact, however, that our estimates for d_f and θ are correlated as they are derived from the same set of disorder realizations [142]. To correct for this effect, we divided the disorder samples for PFBC such that one half is used to estimate $\theta = -0.2795(3)$ ($Q = 0.47$) and the other half is used to estimate $d_f = 1.273\,22(12)$ ($Q = 0.32$) using the same fit functions and ranges as for the full data set. With these estimates, we find

$$d_f - 1 - \frac{3}{4(3+\theta)} = -0.00246(12),$$

where the deviation from zero is still about 20 standard deviations, corresponding to the expected reduction by halving the statistics, so the correlation effect appears to be weak.

As an alternative analysis, we also attempted to perform a simultaneous fit of power laws to the scaling of $|\Delta E|$ and ℓ while enforcing the relation (3.4.9) between the scaling exponents. Independent of whether we use the full or the split data set, a fit quality $Q > 0.01$ is only achieved for $L_{\min} \geq 1000$, which is way above the range of lattice sizes where scaling corrections are visible above the statistical errors (recall that both the defect energies and domain-wall lengths are fully consistent statistically with pure power-laws for $L > L_{\min} = 40$). The conclusions from considering the independent data set for PPBC are similar, with the deviation from Eq. (3.4.9) being $-0.00231(47)$, corresponding to 5 standard deviations. The values for the deviations for PFBC and PPBC are statistically consistent, the appearance of better consistency for PPBC is due to the smaller statistics there.

While it is always difficult to reject or confirm an exact (but non-rigorous) relation based on numerics, it appears safe to say that our data does not appear to be consistent with Eq. (3.4.9). It is worthwhile to note that, on the other hand, our values for θ and d_f are fully consistent with previous estimates, cf. the data compiled in Table 3.5, and it is only due to the increased accuracy resulting from the bigger systems and larger numbers of disorder samples considered here that the inconsistency with Eq. (3.4.9) arises.

3.4.6 Probability distributions

Apart from studying the ground-state, defect energies as well as the domain-wall lengths and the average values reported in the previous sections, it is also interesting to study the full distributions of these quantities over disorder samples. The width $\langle (e - \langle e \rangle_J)^2 \rangle_J$ of the distribution of ground-state energies per spin shows power-law scaling according to L^{Θ_f}, where we find $\Theta_f = -0.9995(3)$ for PFBC and $\Theta_f = -1.002(1)$ for PPBC, consistent with the theoretical expectation [119] $\Theta_f = -d/2$. The latter follows from a standard argument of decomposition of the system into effectively uncorrelated subsystems, such that the total energy is a sum of independent contributions. As a result, in the thermodynamic limit the distribution narrows to a delta peak, consistent with the fact that the ground-state energy is self-averaging [143]. To investigate the shape of the distribution, we studied its kurtosis defined in Eq. (3.4.4). Kurt$[e]$ is shown in Fig. 3.10(a) for the PFBC case, where it is found to be consistent with 3 to within statistical errors for all lattice sizes $L \geq 20$, indicating that the distribution of ground-state energies is in fact Gaussian [144]. This is in contrast to systems with long-range interactions such as the Sherrington-Kirkpatrick model, where non-Gaussian distributions are found [119].

For symmetric coupling distributions the histogram of defect energies for P and AP boundaries is also symmetric and so has zero mean. It is expected that the standard deviation $\sigma(E)$ has the same asymptotic scaling behavior as the modulus $|\Delta E|$, and this is consistent with our observations. Considering the data for $\sigma(\Delta E)$ for PFBC, we use a pure power-law fit with $L \geq L_{\min} = 30$ to find $\theta = -0.2793(3)$ ($Q = 0.55$). For PPBC, on the other hand, the same analysis yields $\theta = -0.279(2)$ and $Q = 0.81$ for the same range. In Fig. 3.10(b) we show the defect energy distribution for PFBC systems for a number of different lattice sizes, rescaled by the factor L^{θ} with $\theta = -0.2793$ describing the decay in width. As the Gaussian distribution with the same mean and width shows, the defect energy distribution is clearly not normal, but instead has much heavier tails[6]. This is confirmed by an inspection of the distribution kurtosis, Kurt$[\Delta E]$, which is found to be consistent with Kurt$[\Delta E] = 4.70(2)$ for systems of size $L \geq L_{\min} = 20$.

The standard deviation of the distribution of domain-wall lengths is found to have the same scaling as the mean, i.e., it is asymptotically proportional to L^{d_f}, suggesting a complementary way of determining the fractal dimension. This approach yields estimates of $d_f = 1.2740(3)$ for PFBC ($L_{\min} = 40$, $Q = 0.34$) and $d_f = 1.276(2)$ for PPBC ($L_{\min} = 50$, $Q = 0.61$), respectively. The result for PFBC is slightly high as compared to the result from the mean, but still statistically

[6] We note that there might be a relation between the behavior of the defect-energy distribution at vanishing energies and the question of a multiplicity of states in spin glasses [145].

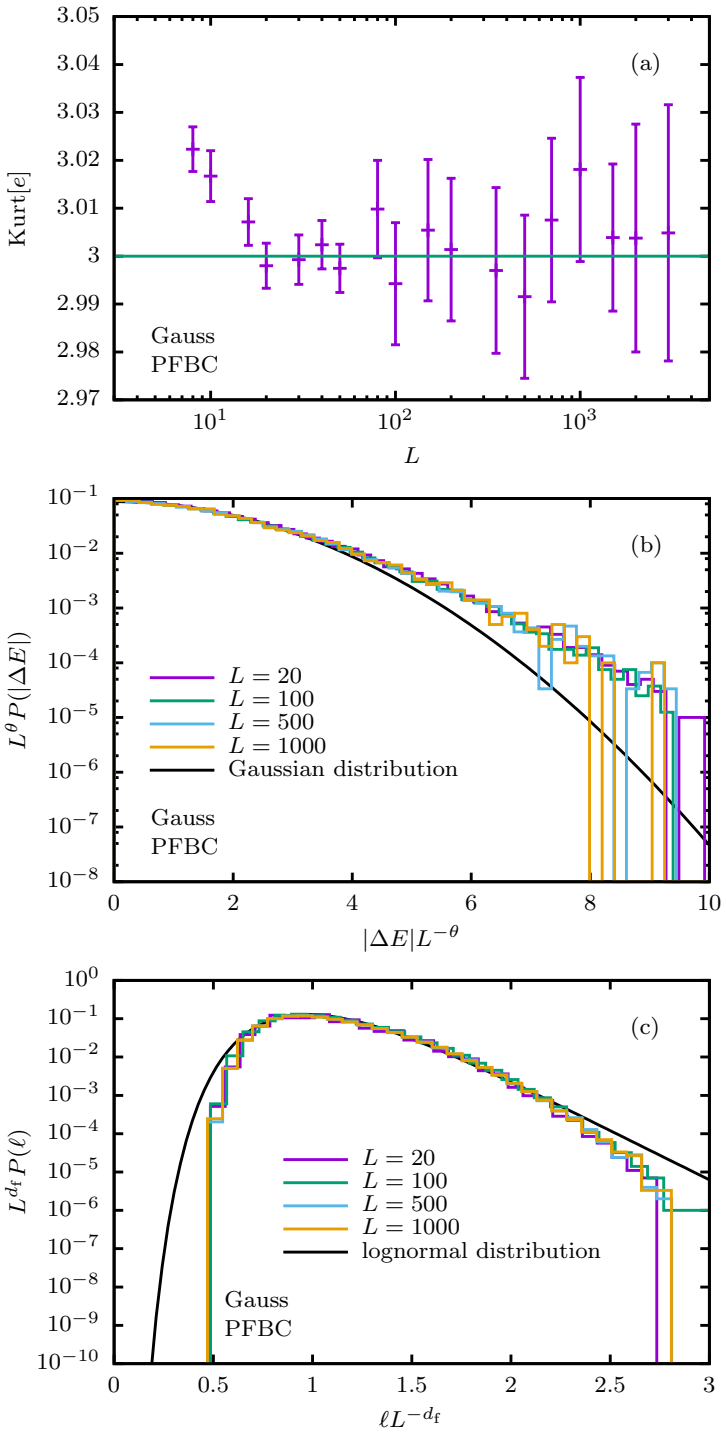

Figure 3.10: (a) Scaling of the kurtosis Kurt[e] of the distribution of ground-state energies per spin for the Gaussian model with PFBC as a function of system size. For $L \geq 20$ it is consistent with the value Kurt[e] = 3 of a normal distribution. (b) Distribution of defect energies $|\Delta E|$ for the same model, rescaled with the expected asymptotic behavior $\propto L^\theta$ with $\theta = 0.2793$. The solid line shows a Gaussian distribution of the same mean and variance. (c) Distribution of domain-wall lengths ℓ for the PFBC Gaussian case, rescaled according to the limiting form $\propto L^{d_f}$ with $d_f = 1.27319$. The solid line represents a lognormal distribution fitted to the empirical data.

consistent: the deviation is 2.6 times the combined error bar, but this does not take into account that the two error estimates are correlated and so the combined fluctuation is likely to be higher than the naive estimate [146, 142]. The two PPBC estimates are fully consistent. The distribution of domain wall lengths is found to be clearly non-Gaussian, with a kurtosis that is consistent with $\mathrm{Kurt}[\ell] = 3.656(4)$ for systems of size $L \geq L_{\mathrm{min}} = 20$. It was suggested in Ref. [20] that the distribution might be in fact lognormal. Our data for the distribution of ℓ for PFBC is shown in Fig. 3.10(c), together with a fit to a lognormal distribution. As is apparent, it describes the data reasonably well close to the mode, but there are significant deviations in the tails.

3.5 Summary and conclusion

In this chapter, we first presented a fast exact algorithm to calculate the grand state of the two-dimensional Ising spin glass systems. The algorithm is based on the minimum-weight perfect matching (MWPM) problem and works properly when the system has at least one open boundary. We then introduced a new quasi-exact algorithm based on the windowing technique and MWPM to determine the ground state of Ising spin-glass systems with fully periodic boundary conditions. Our algorithm is simple to understand and simple to implement (having MWPM algorithm in hand), and is able to find true ground states with arbitrary high probability in a polynomial time.

As an application of our algorithm, we considered systems with Gaussian bond distribution and looked at the ground-state energy, stiffness exponent, domain-wall lengths, fractal dimension and the probability distributions of these quantities for such systems. We studied systems with PPBCs by our algorithm up to $3\,000 \times 3\,000$ spins and compared our results against systems with PFBCs up to $10\,000 \times 10\,000$ (10^8) spins. Our estimates of the ground-state energies $e_\infty = -1.314\,787\,6(7)$ for PFBC and $e_\infty = -1.314\,788(3)$ are consistent with each other, and are compatible with, but up to 100 times more precise than the estimates in the careful study of Ref. [120] using exact ground-state methods, and the recent work Ref. [147] using Monte Carlo.

We also determined the stiffness exponent θ and the fractal dimension d_{f} for these two types of boundary conditions. Our results for PPBC obtained by our algorithm, i.e., $\theta = -0.2778(11)$ and $d_{\mathrm{f}} = 1.2732(5)$, are in agreement with the results of PFBC, i.e., $\theta = -0.2793(3)$ and $d_{\mathrm{f}} = 1.273\,19(9)$ (obtained by exact algorithm based on MWPM), indicating the correctness of the windowing technique for the PPBC case. These system sizes are the largest ones that have been ever studied and these estimates for θ and d_{f} are consistent with previous studies but one or two orders

of magnitude more precise than previous results, see the data collected in Table 3.5.

At the end, we checked the consistency of the SLE conjecture $d_f = 1 + 3/4(3 + \theta)$ (3.4.9) with our most accurate estimates where we saw that our data does not appear to be consistent with this conjecture.

Chapter 4

Cluster algorithm for uniform sampling of spin-glass ground states

4.1 Introduction

We have seen in chapter 3 that the the ground states for the two-dimensional EA model with free boundaries in at least one direction can be exactly determined by a transformation to a graph theoretical problem called minimum weight perfect matching (MWPM). Systems with Gaussian couplings have a unique ground state spin configuration. Therefore the domain wall of such systems can be simply determined by comparing the ground state spin configurations of periodic and anti-periodic boundary conditions. In contrast, for systems with bimodal bond distribution there is a huge ground-state degeneracy. As has been demonstrated with numerical calculations [83, 84] and also shown rigorously [148], this model even has a finite ground-state entropy, indicating that the number of ground states grows exponentially with system size. There are some properties at zero temperature that they do not depend on the spin configuration, such as the ground-state energy and the defect energy. In this case the system can be fully studied by having access to only one of the ground states of each system. However some other properties, for instance the magnetization or the domain-wall length, can vary from one ground-state configuration to another. Therefore all of the ground states are needed if we want to have the correct statistics of these properties. In order to do so we are facing two major problems. The first problem is that there is no such algorithm which can generate all of the ground states. The second problem arises by considering the fact that the number of the ground states grows exponentially and therefore we would not be able to generate all of them in a reasonable time. Although it is not possible to generate all of the ground states (except for very small system sizes), in many practical purposes it is sufficient to have good statistics of the ground states.

The matching-based algorithms described in chapter 3 can be used to generate different ground-state spin configurations of systems with $\pm J$ bond distribution, because the solution to the matching problem is not unique. There are several, possibly many, solutions to the matching problem that have the same minimal weight. In practice, the implementation of the matching algorithm used will return an arbitrary solution out of this set, where the state chosen depends on the specific implementation of the algorithm used (for instance on the order in which nodes and edges are examined) and the state returned might or might not be reproducible between runs[1]. Clearly, this setup is not suitable for sampling such states with a prescribed probability weight.

One way of solving this problem and ensuring uniform sampling of states might be to break the degeneracy in a way such that each ground state is preferred the same number of times by a chosen procedure. If one examines a pair of ground states, one will find that they differ by the overturning of a set of disjoint, but singly connected clusters of spins. As, by definition, this procedure does not change the overall energy, this corresponds to a set of "free" spins[2]. The degeneracy can be lifted by adding some small perturbation to the bonds, i.e., $J_{ij}(k) = J_{ij} + k\epsilon_{ij}$ with a continuous, symmetric distribution of the random variables ϵ_{ij}, a natural choice being the standard normal distribution, $\epsilon_{ij} \sim \mathcal{N}(0,1)$. As the spectrum of states for the bimodal model is gapped [84], if k is chosen sufficiently small the ground state of the system with couplings $J_{ij}(k)$ will also be a ground state of the system with $k = 0$. Since the perturbation follows normal distribution this method is known as *Gaussian noise* technique. Considering a cluster of free spins for a symmetric distribution of ϵ_{ij}, the sum of the noise terms ϵ_{ij} along the bonds on the cluster boundary will have either sign with the same probability of 1/2. Hence one half of the realizations of ϵ_{ij} should lead to this cluster being in one orientation and the other half to it being in the reversed orientation, implying uniform sampling of degenerate ground states. A similar approach was used in Refs. [149] and [150]. However, clusters that touch each other are not independent and hence the procedure leads to a strongly non-uniform distribution of sampled states [151].

In this chapter we are going to introduce a new efficient algorithm to sample the degenerate ground states of the two-dimensional $\pm J$ Ising spin glass uniformly. The algorithm is based on an analysis of free spin clusters and enables us to calculate all of the ground states for systems with $L \leq 20$. In addition, the algorithm picks up the ground states uniformly from the ground states manifold and therefore gives us the correct statistics of the ground states which can be used for larger

[1] The energy of the state returned, on the other hand, is of course always the same.
[2] Free spins are those which can be flipped without energy cost.

system sizes. We have successfully used it to sample ground states uniformly up to $L = 128$.

This chapter is organized as follows. Sec. 4.2 is devoted to the description of our algorithm where we first describe the main idea in section 4.2.1, followed by discussing how the exact cluster configuration can be determined in section 4.2.2 and how the cluster configuration can be used to generate the ground states uniformly in section 4.2.4. Then we show some features of our algorithm together with the results obtained by using the algorithm in Sec. 4.3. Finally, the summary and conclusions is presented in section 4.4.

4.2 The algorithm

4.2.1 Main idea

Firstly we present the main idea of the algorithm by looking at a simple real example. Consider an Ising spin glass which has $n_{\mathrm{GS}} = 8$ degenerate ground states. Due to the Ising symmetry of the spins, there is a global degeneracy in this system, which means that by flipping all the spins of one ground state we will get another ground state spin configuration. We are not interested in this kind of degeneracy because it only changes the magnetization from M to $-M$ and does not give us any new information. From now on we always neglect the global degeneracy. Therefore the considered system would have only $n_{\mathrm{GS}} = 4$ distinct ground states. Fig. 4.1 shows all of the ground state spin configurations of the system. If we compare these spin configurations with each other we will see that the only difference between them are two single spins which have different orientations in different ground states (Fig. 4.2). We call these spins *free spins*, because we can flip them without changing the energy. Therefore if we know these two free spins and only one of the ground states, then we will be able to generate all of the ground state spin configurations of the system.

In the above example we had only two separate free spins but in general free spins can be either one single free spin or a group of spins (called *free spin clusters*) which can only be flipped together without energy cost. Additionally, the two free spins were independent in the example, however in general, free spins and free spin clusters can be dependent, i.e., we can flip one of them only if the other one has been already flipped. The main idea of our algorithm is to find all the free spins and free spin clusters, i.e., the *cluster configuration* of the system and generate the ground states using the cluster configuration.

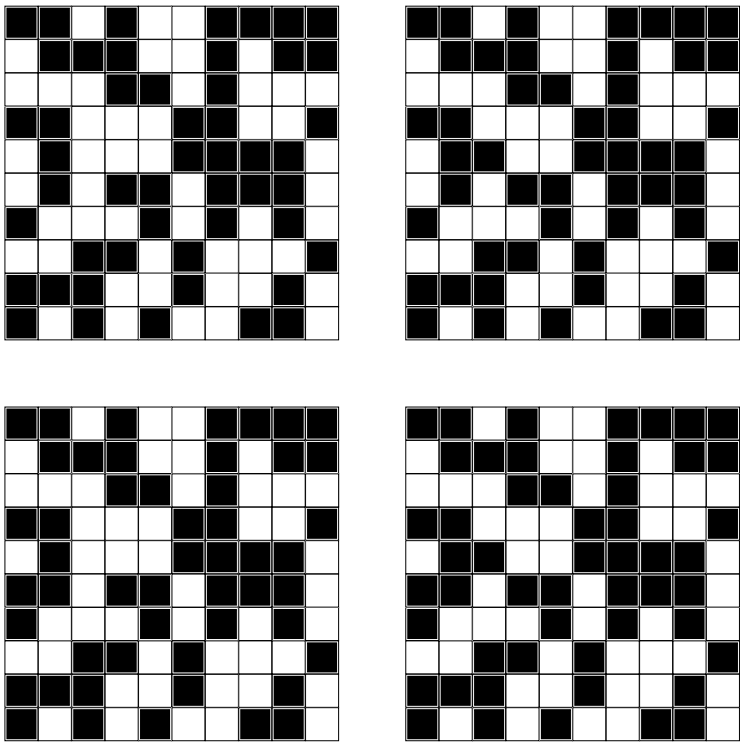

Figure 4.1: Ground state spin configurations of a system with $n_{GS} = 8$ ground states. Here we do not show the global degeneracy. Therefore we have only 4 ground state spin configurations. Black and white squares indicate $S = -1$ and $S = +1$ respectively.

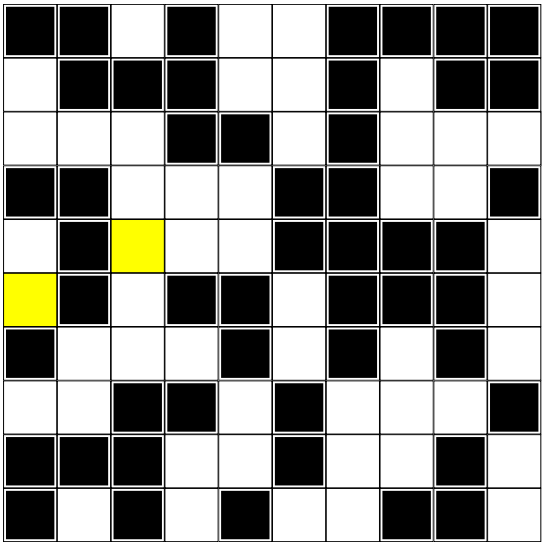

Figure 4.2: The difference between all of the ground states of the sample in Fig. 4.1. Black squares show $S = -1$, white squares represent $S = +1$, and yellow ones indicate the spins which are +1 in some configurations ans −1 in the others.

4.2.2 Calculating the cluster configuration

In order to calculate the cluster configuration of the system we need to check whether the status of each bond (being satisfied or unsatisfied) does change in all of the ground states or not. If the status of a bond changes from one ground state to another, it means that the relative orientation of the spins at the two ends of this bond can vary in different ground states and therefore they belong to two different clusters. These bonds are called *flexible bonds* while the remaining bonds are called *rigid bonds*. The status of a rigid bond remains unchanged in all of the ground states which means the two spins joint by the bond must be flipped together, i.e., they are in the same cluster. In order to find the flexible and rigid bonds of the system we use a technique introduced by Romá *et. al* [25]. In this method, we first determine the ground state energy E_0 of a system with couplings $\{J_{ij}\}$, and one of the ground states spin configurations. For each of the bonds J_{ij} of the system we then flip S_i and calculate the energy of the system with the constraint that the new relative spin orientation of S_i and S_j is fixed. This can be done by changing J_{ij} to KJ_{ij} where K is a large positive constant. Due to the value of K being large, the bond KJ_{ij} must be satisfied in the matching result which means the relative orientation of S_i and S_j will remain the same. Then we calculate the energy of of the original system $\{J_{ij}\}$ with respect to the new spin configuration. If the new energy is the same as the ground state energy then J_{ij} is flexible, otherwise it is a rigid bond. The exact cluster configuration of the system can be then determined by going through all the bonds and checking whether they are rigid or flexible.

4.2.3 Cluster decomposition

After finding all the flexible and the rigid bonds, the cluster configuration of the system can be easily determined by using one of the known methods such as the Hoshen-Kopelman algorithm [152], breadth-first (or depth-first) first search [153, 154], etc. We will use breadth-first search in our calculations.

4.2.3.1 Speeding up the process

In order to find the flexible and the rigid bonds explained in section 4.2.2, MWPM should be implemented for each bond. Therefore, for the 2D Ising spin glass system of system size L the number of necessary times that MWPM has to be called, N_{MWPM}, will be $N_{\mathrm{MWPM}} = \alpha L^2$ in which for systems with fully periodic boundary conditions $\alpha = 2$, and for systems with either periodic-free or free-free boundary conditions is slightly less than 2. This value, however, can be reduced by determining the free spins, and as the result, the cluster configuration can be determined faster.

Let us go back to our simple example in Fig. 4.1 and Fig. 4.2 again. The given system has two clusters both of which contain only one spin. We detected these clusters by comparing different ground states. But if we consider only one ground state spin configuration and try to flip all the spins one by one and check whether the energy changes or not, we are able to detect such clusters directly from even one ground state. In a general case, the system has both clusters of size one and bigger than one. Clusters of size one are free spins because they are free to be either *up* (+1) or *down* (-1) in the ground state spin configuration. It is possible to use this idea and reduce the value of α by generating some initial ground states and searching for the free spins on those ground states. To do so, we use the Gaussian noise technique explained in section 4.1. Note that although this technique does not pick up the spin configurations from the ground state manifold uniformly, however, we can still use it to generate the necessary initial ground state spin configurations for our cluster algorithm.

The relation between the number of initial ground states, N_{iGS} (generated by Gaussian noise technique), and the probability to find all of the clusters of the system, P_{all}, is shown in Fig. 4.3 for different system sizes[3]. According to Fig. 4.3 almost 70% of the clusters can be found by generating $0.3L^2$ initial ground states. Although this estimate varies a little for different system sizes and it is not very accurate, it is still good enough for us to speed up our algorithm. Therefore for a disorder realization of size L we will generate $0.3L^2$ initial ground states using Gaussian noise technique.

We can also speed up the process of finding the free spins of the systems. To do that, for each of these initial ground states, we check all the spins one by one to see whether they are free spins or not and we make a *list of free spins*. This can be done by considering one ground state and flipping each spin and calculate the energy of the system according to the new orientation of the spin. If the energy of the new system is the same as the ground state energy then the spin is a free spin and it needs to be added to the list. As soon as a spin is inserted in the list, we can conclude that all of its bonds are flexible without implementing extra MWPM which is needed in Romá's technique. Once we have gone through all the spins and the list is completed, we will choose one spin from the list randomly and flip it. It is because if we flip one free spin, new free spins might be created. We then check the neighbors of the flipped spin and if any of them was not a free spin and it has become a free spin in the new configuration, we will add it to the list, i.e., we *update the list*. Note that it is also possible that some of the free spins in the previous configuration are not free in the new one. In this case we delete the spins

[3]The technique explained in section 4.2.2 is able to determine all the clusters of the system. Therefore we first use that technique (without any optimization) to determine all the clusters, and then, we compared that with the obtained clusters for different values of N_{iGS} to calculate P_{all}.

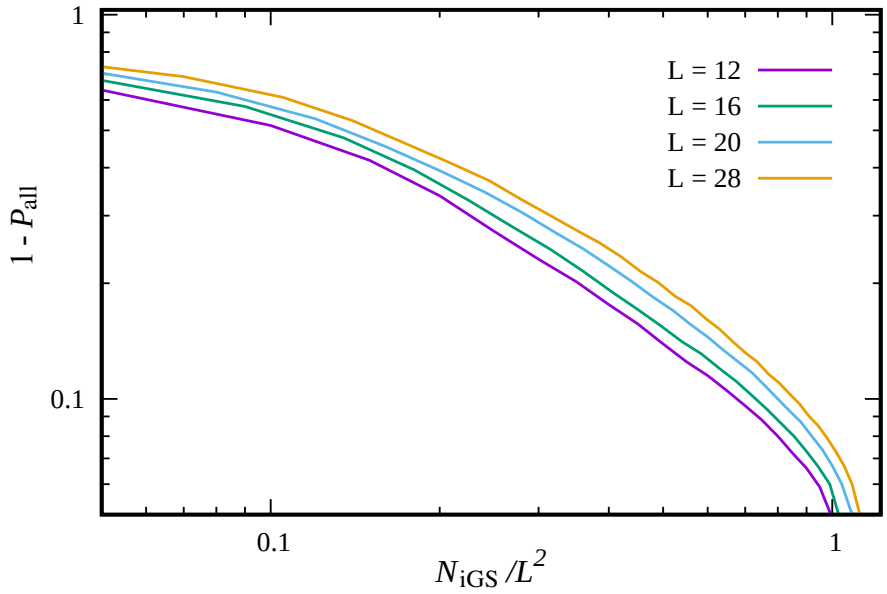

Figure 4.3: The average value of $1 - P_{all}$ vs. the number of initial ground states, N_{iGS}, for different system sizes in which P_{all} indicates the probability to find all the clusters of the system. The plot shows that P_{all} increases with N_{iGS} exponentially. The results are averaged over 100 disorder realizations.

from the list. We repeat updating the list for n_{upd} times until we do not find new free spins. Fig. 4.4 shows how the minimum number of the initial ground states needed to find all the clusters of the system, N_{min}, varies by changing the number of updates per ground states. As Fig. 4.4 indicates, by increasing the value of n_{upd} the value of N_{min} will be decreased until $n_{upd} \approx 3L^2$. Therefore we choose $n_{upd} = 3L^2$ in our calculations.

Apart from searching for free spins through the initial ground states, we can also compare them with each other to find some other flexible bonds, especially the bonds at the boundaries of the spin clusters. To do so, for each bond J_{ij} of the system we define $R_{ij} = \sum_{k=1}^{N_{iGS}} S_i^k S_j^k$ in which S_i^k is the orientation of the i-th spin in the k-th initial ground-state spin configuration. If spin i and spin j have the same relative orientation in all the initial ground states, then $|R_{ij}| = N_{iGS}$, otherwise $|R_{ij}| < N_{iGS}$ which means S_i and S_j are in different clusters. Therefore if $|R_{ij}| < N_{iGS}$ the bond between S_i and S_j is a flexible bond. By making the list of the free spins for each initial ground state, updating the list and comparing all the initial ground states with each other at last, we expect that the number of times of calling the MWPM to determine the cluster configuration of the system will be reduced.

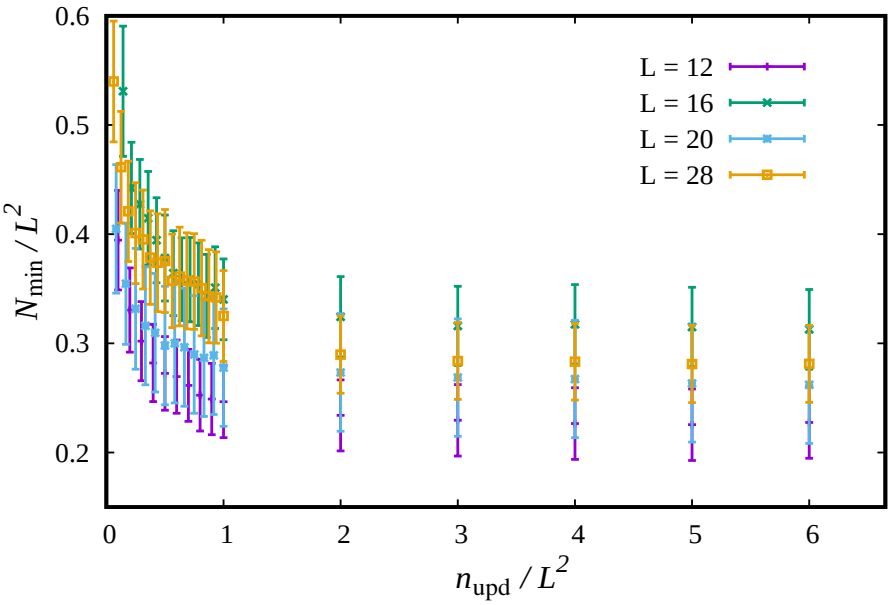

Figure 4.4: The average value of $N_{\min}$, the minimum number of necessary initial ground states to find all of all the clusters of the system, over 100 disorder realizations versus n_{upd}, the number of times we have updated the list of free spins, for different system sizes.

Fig. 4.5 shows the average number of times that we need to calculate MWPM for each system size. We have considered $N_{\text{iGS}} = 0.3L^2$ and $n_{\text{upd}} = 3L^2$ in our calculations, and the results have been averaged over 100 disorder realizations for each system size. According to Fig. 4.5 the idea of searching for free spins together with comparing the initial ground states can decrease the value of N_{MWPM} from $N_{\text{MWPM}} \approx 2L^2$ to $N_{\text{MWPM}} \approx 1.2L^2$.

The process of calculating the cluster configuration of a system of linear size L can be summarized as follows:

- An initial ground-state spin configuration is generated using Gaussian noise technique.
- We go through the spins, flip them one by one and make the list of all free spins. Every time one spin is inserted in the list all of the bonds between the spin and its neighbors will be labeled as flexible.
- The list of free spins will be updated for $n_{\text{upd}} = 3L^2$ times. The labels of the bonds will be updated accordingly as well.
- The above steps are repeated for $N_{\text{iGS}} = 0.3L^2$ times.

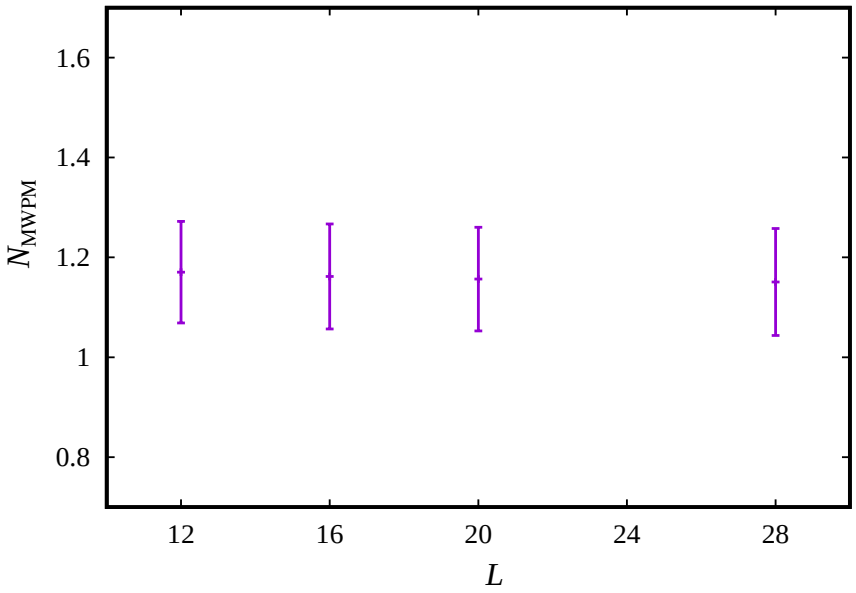

Figure 4.5: The average number of necessary iterations of MWPM vs. system size L for systems with periodic-free boundary conditions, over 100 disorder realizations. It indicates that one can consider $N_{\mathrm{MWPM}} \approx 1.2L^2$.

- All the initial ground-state configurations will be compared to each other by calculating $R_{ij} = \sum_{k=1}^{N_{\mathrm{iGS}}} S_i^k S_j^k$. Then if $|R_{ij}| < N_{\mathrm{iGS}}$ the corresponding bond J_{ij} will be labeled as flexible.
- All the remaining bonds will be checked by Romá's technique to find all the flexible bonds of the system exactly.
- Once all the flexible bonds are determined, the cluster configuration will be calculated using breadth-first search.

Note that all the bonds are labeled as rigid bonds at the beginning of the process. Once the cluster configuration is determined then it can be used to generate and sample the ground states of the system. This procedure is describe in the next section.

4.2.4 Sampling the ground states

Now we are ready to generate the ground states by using the cluster configuration of the system. The general idea, as we have shown in Fig. 4.1 and Fig. 4.2, is to flip the clusters randomly and check whether the energy of the new configuration is the same as the ground state energy or not. As the first idea, we can start from

one ground-state configuration, choose one cluster randomly and flip it[4]. We then calculate the energy of the new configuration and if it is the same as the ground state energy then we accept the move, otherwise the move will be rejected. This process is quite fast and can generate the accessible ground states uniformly, but it is restricted to only one ground-state valley [151].

The problem of being restricted to only one ground-state valley can be solved by using Markov chain Monte Carlo method together with Metropolis moves [155] instead of only zero-energy moves. In this case, we consider a low temperature T and we start from a random cluster configuration of the system. We then choose one of the clusters randomly and flip it. The energy of the new configuration is calculated and if the energy is smaller than the old configuration the move will be accepted. If the energy increases the move is accepted with probability $P_{\text{accept}} = e^{-\Delta E/k_{\text{B}}T}$ in which ΔE is the change in energy. This process is repeated until the system reaches equilibrium. Since the moves with $\Delta E > 0$ also have a chance to be accepted in this method, then technically the system is not restricted to only one valley and can jump between the valleys. In practice, however, Ising spin glasses have a rugged energy landscape and there are large energy barriers between different ground-states valleys. In order to find the ground states we have to go to low temperatures, and at those temperatures when ΔE is large, P_{accept} will be very small and the positive-energy moves will never be accepted. Therefore the system cannot jump over the large barriers and it is restricted only to the ground-state valleys with small energy barriers.

In order to overcome this problem one can increase the temperature. As the result of increasing the temperature, P_{accept} becomes large enough so the positive-energy moves even for large values of ΔE have a reasonable chance to be accepted. But if we increase the temperature, the probability of finding the ground state decreases exponentially. To over come this dilemma, Hukushima and Nemoto in 1996 [156] introduced a method called *Parallel Tempering Monte Carlo* (PTMC). This algorithm can be described as follows:

- Consider M copies of the system at different temperatures between T_{min} and T_{max} with random cluster configurations.
- For each copy, we do random cluster flips with probability $P_{\text{accept}} = \min(1, e^{-\beta\Delta E})$ in which $\beta = 1/k_{\text{B}}T$.
- For all pairs of replicas at neighboring temperatures:
  - $\delta = (\beta_{m+1} - \beta_m)(E_m - E_{m+1})$.

[4] All of the spins inside the cluster will be flipped.

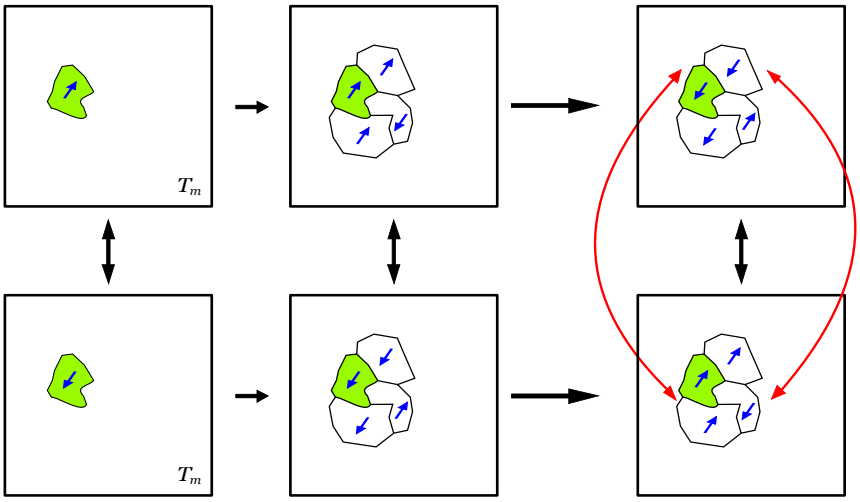

Figure 4.6: Schematic presentation of a Houdayer's exchange move. Two copies of the system at the same temperature T_m and one cluster are chosen randomly. If the orientation of the cluster is different in the two configurations this cluster and all the other clusters connected to this one which have different orientation in the two configurations will be exchanged.

  - If $\delta \leq 0$ we swap the temperatures $\beta_{m+1} \leftrightarrow \beta_m$.
  - If $\delta > 0$ we swap the temperatures with probability $p = e^{-\delta}$.
- Repeat everything until the system reaches equilibrium.

This algorithm enables the system to jump between large energy barriers, and it reaches the equilibrium much faster than simple Monte Carlo method [14]. Therefore we use this method in our calculations.

In addition to Parallel Tempering Monte Carlo algorithm we also consider another move introduced by Houdayer [157]. In this method we consider N copies of the system at each temperature T. We then choose two configurations at the same T and one cluster randomly. If the chosen cluster has different orientation in the two configurations, we will find all the connected clusters to this cluster which have different orientation in the two configurations, i.e., the domain of flipped clusters where the randomly chosen cluster is in that domain. We then exchange that domain between the two configurations[5]. This process is schematically shown in Fig. 4.6. We refer to the combination of PTMC and Houdayer's move as parallel tempering Monte Carlo with exchange cluster algorithm. This combination allows the copies of the system to exchange big domains of clusters which may not be possible to be exchanged even in PTMC, and enables the system to have access to the entire ground-state landscape. As a summary, in this algorithm we have M

[5]Note that if the orientation of the randomly chosen cluster is the same in both configuration nothing would be done.

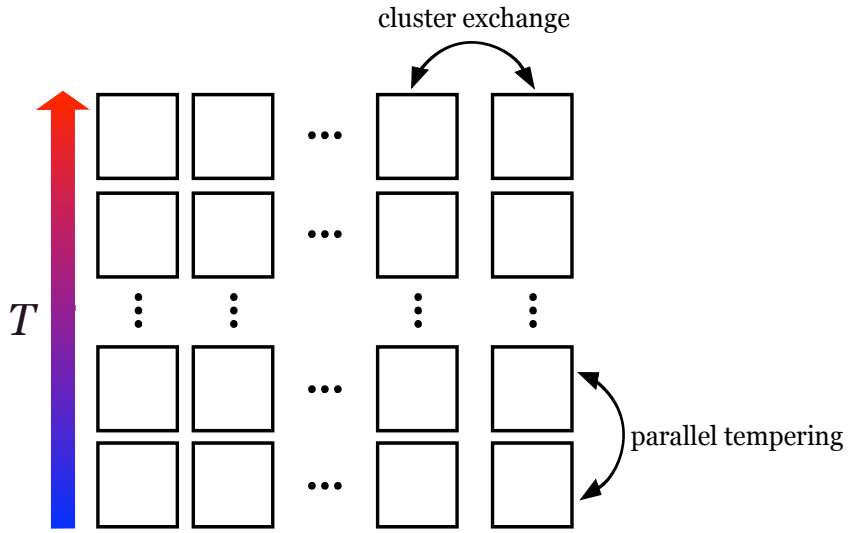

Figure 4.7: Schematic presentation of parallel tempering Monte Carlo with cluster exchange algorithm. There are M different copies of the system at different temperatures and N copies at the same temperature. Parallel tempering moves, i.e., exchange temperatures are done between two neighboring temperatures while cluster exchange is implemented between copies at the same temperature.

different temperatures between $T_{\min}$ and $T_{\max}$ and for each temperature we have N copies of the system. Therefore there are $M \times N$ copies in total. For each copy we will do simple Monte Carlo flips while temperature exchange is implemented between two neighboring temperatures and cluster exchange is done between the copies at the same temperature. This set up is shown in Fig. 4.7.

There are a few parameters in this algorithm which have to be fixed. We need to know the values of $T_{\min}$ and $T_{\max}$ as well as the difference between two neighboring temperatures, i.e., ΔT. We also have to fix the number of temperatures M and the number of copies at each temperature N. We describe the role of each parameter in this algorithm separately.

a) The minimum temperature $T_{\min}$:
The lowest temperature should be low enough to find the ground state. However the higher $T_{\min}$ is, the faster equilibrium will be reached. Therefore we should try to choose the highest $T_{\min}$ in which it is still possible to find the ground state at this temperature. As an example, Fig. 4.8 shows the energy distribution of a disorder realization of size $L = 32$ calculated by PTMC with exchange cluster algorithm. In Fig. 4.8(a) we have used the cluster configuration of the system (not the spin configuration). The results indicate that the probability of finding the ground state decreases by increasing $T_{\min}$. As we can see in Fig. 4.8(a), $T_{\min} \approx 1.0$ is an acceptable value for this system size because we want to have a reasonable

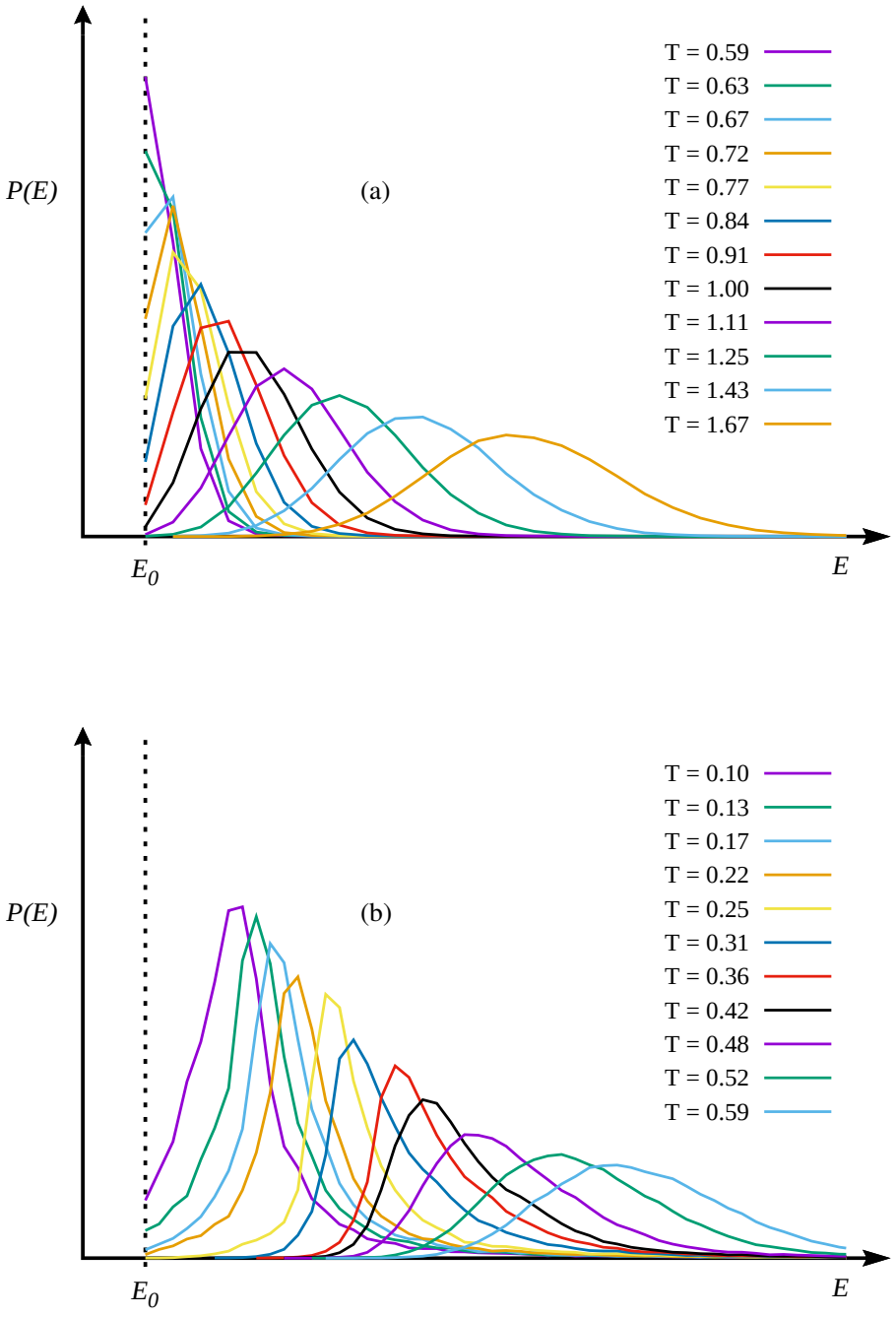

Figure 4.8: Energy distribution for one disorder realization of size $L = 32$ at different temperatures using PTMC with cluster exchange algorithm. E_0 is the ground-state energy. (a) The cluster configuration of the system is used. The probability of finding the ground state is reasonably large up to $T \approx 1.0$. (b) The spin configuration of the same system is used. In this case, the probability of finding the ground state of the system has a reasonable value only for temperatures below $T = 0.22$.

Table 4.1: The minimum temperature, $T_{\min}$, considered in our calculations for different system sizes L and systems with periodic free boundary conditions.

L	$T_{\min}$
10	1.30
16	1.20
20	1.10
24	1.10
28	1.00
32	0.90
48	0.80
64	0.70
80	0.60
100	0.50
128	0.40

probability of finding the ground state for the lowest temperature. If we use the standard Monte Carlo simulations, i.e., we flip only one single spin rather than clusters of spins, the lowest temperature for finding the ground state with reasonable probability would be much lower than $T_{\min} \approx 1.0$. This situation is shown in Fig. 4.8(b) and indicates that the lowest acceptable temperature for standard Monte Carlo moves for the same disorder realization is about $T = 0.22$. Our results show that by increasing the system size L the width of the energy distributions decreases, and therefore the value of $T_{\min}$ decreases as well. The value of $T_{\min}$ that we have chosen in our calculations for system sizes $10 \leq L \leq 128$ is shown in Table 4.1.

b) The maximum temperature $T_{\max}$:
Although we are only interested in the ground states of our systems, we still need to have some high temperatures in parallel tempering to allow the system to jump over the barriers between the ground states funnels. In order to overcome the barriers, some of the moves with increasing energy must be accepted. The acceptance probability of each move depends on change in the energy of the system as $P_{\text{accept}} = e^{-\beta \Delta E}$. For simple Monte Carlo only one single spin is flipped at each step and therefore the maximum value of energy change can be $\Delta E = 8|J|$ where J is the strength of the bonds of the system with bimodal couplings. Therefore the minimum value of P_{accept} would be $e^{-8\beta|J|}$ and if the highest temperature is chosen as $T_{\max} \approx 2$ there would be a reasonable value for P_{accept} at this temperature for the moves with the biggest increase in energy to be accepted. However in our algorithm we flip a cluster of spins at each step, and the change in energy depends on the size of the cluster. Since some of the clusters of the systems can be very large, the change in energy at each step can be very large as well and therefore we need to go to a much higher temperature for these moves to have a reasonable

acceptance probability. The highest temperature must be high enough to allow the biggest clusters to flip. Therefore in order to make sure that the biggest cluster would always get a reasonable chance to be flipped at the highest temperature we choose it as $T_{\max} = \infty$.

c) The temperature difference ΔT:
One of the key features of parallel tempering is that we swap the temperature of the copies of the system at neighboring temperatures with probability $p = e^{-\delta}$ in which $\delta = (\beta_{m+1} - \beta_m)(E_m - E_{m+1})$ and $\beta = 1/T$. Therefore, the probability of changing the temperatures depends on the difference between the energy of the copies at different temperature, i.e., $\delta E = E_m - E_{m+1}$. If δE becomes very large then the move of swapping neighboring temperatures would never be accepted. Therefore, E_m and E_{m+1} should not be too far from each other. This means the energy distribution of the two neighboring temperatures must overlap, otherwise E_m and E_{m+1} would be never close enough. As we can see from Fig. 4.1, the distribution of the energy becomes narrower as the temperature decreases and it is wider for higher temperatures. Therefore ΔT should be chosen in a way that the temperature difference at low temperatures becomes smaller than the temperature difference at high temperatures. One of the common choices of ΔT is equally spaced on β, i.e., $\Delta\beta = (\beta_{\max} - \beta_{\min})/M$ in which M is the number of temperatures. This choice of ΔT has the required condition for overlapping the energy distributions as it provides more copies at lower temperatures than higher temperatures. Therefore we choose ΔT as equally spaced in β in our calculations.

d) Number of temperatures M:
The number of temperatures plays an important role in parallel tempering. Increasing the number of temperatures will increase the overlap between the energy histograms (especially at low temperatures), and it helps exchanging the temperature between copies of the system at neighboring replicas, but increasing M will increase the computational effort as well. Therefore M should be large enough to have reasonable acceptance rate for low temperatures, and at the same time, it should be small enough to have a reasonable *tunnelling time*, the time (in MC steps) it takes for a copy of the system to go from $T_{\min}$ to $T_{\max}$ and come back to $T_{\min}$ again. In general, the number of temperatures depends on the system size L. We can write the number of temperatures as $M = \alpha L$ in which α is a constant to be determined. Fig. 4.9 shows the value of tunnelling time for different values of α for system sizes $L = 16, 32, 64$, revealing that the minimum value of the tunnelling time is obtained for $\alpha = 0.7$. Therefore we set $\alpha = 0.7$ and the number of temperatures in our calculations is $M = 0.7L$.

e) Number of copies per temperature N:
We want to use parallel tempering with exchange clusters and thus at least two

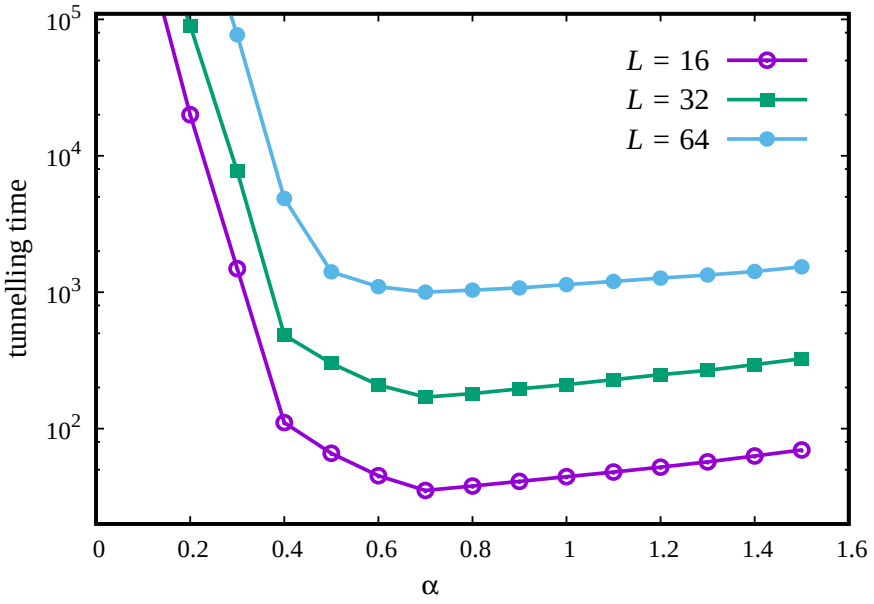

Figure 4.9: Tunnelling time vs. the number of temperatures $M = \alpha L$ for parallel tempering with cluster exchange for two different system sizes. The result indicates that the minimum value for tunneling time is achieved when $\alpha = 0.7$.

copies of the system per temperature is needed, i.e., $N = 2$. Increasing N will increase the computational effort so the value of N should not be too large. We choose $N = 4$ in our calculations[6].

All the required parameters in our algorithm are now determined and we are ready to use our algorithm to sample the ground-state configurations of the systems with degenerate ground states (in our case, the 2D $\pm J$ Ising spin glass) uniformly. As a summary, our algorithm has two major steps:

Step 1) Determining the exact cluster configuration of the system.

Step 2) Use the exact cluster configuration to generate the ground states uniformly.

The details of the first major step are discussed in section 4.2.2, and in the current section we have explained the second one. Our uniform sampling algorithm (including all the steps and parameters) can be summarized as follows:

[6]The reason for this choice is that sometimes we need to consider the overlap between the replicas at the same temperature and we want to have at least two separate sets of overlap. Therefore we choose have $N = 4$ replicas per temperature.

I . Determining the exact cluster configuration of the system (see sec. 4.2.2 for the details).

- Generate an initial ground state using Gaussian noise technique.
- Make a list of free spins and label the corresponding bonds as flexible.
- Update the list (and labelling the relative bonds) $n_{\text{upd}} = 3L^2$ times.
- The above steps are repeated for $N_{\text{iGS}} = 0.3L^2$ times.
- Compare all the initial ground states to find new flexible bonds.
- Check all the remaining bonds using Romá's technique.
- Determine the exact cluster configuration using the breadth-first search.

II . Use the exact cluster configuration to generate the ground states uniformly (see sec. 4.2.4 for the details).

- Consider $M \times N$ replicas of the exact cluster configuration (with random cluster orientations) in which $M = 0.7L$ copies are at different temperatures between T_{min} (Table 4.1) and $T_{\text{max}} = \infty$ distributed as equally spaced on $\beta = 1/T$, and $N = 4$ copies at the same temperatures.
  - Monte Carlo moves with probability $P_{\text{accept}} = \min(1, e^{-\beta\Delta E})$ for accepting increasing energy moves.
  - Swap the temperatures of replicas at neighboring temperatures by probability $p = \min(1, e^{-\delta})$ where $\delta = (\beta_{m+1} - \beta_m)(E_m - E_{m+1})$.
  - Implement cluster-exchange moves between replicas at the same temperature.
  - Repeat the above steps until the system reaches equilibrium.

Once the equilibrium is reached, we can calculate the energy of each replica (especially at lower temperatures), and the ones which have the energy equal to E_0 are the ground states.

4.3 Results

In this section, we first show some features of the cluster structure of the ground-state manifold of the 2D Ising spin glass system with bimodal bond distribution. Some aspect of our uniform sampling algorithm is presented next. At the end, the results of uniformly sampled ground states of these systems together with some results related to the ground-state energy will be shown.

4.3.1 Number of clusters N_c

In order to find the average number of clusters N_c, we have calculated the cluster configuration of 1000 disorder realizations of system sizes $10 \leq L \leq 128$. The

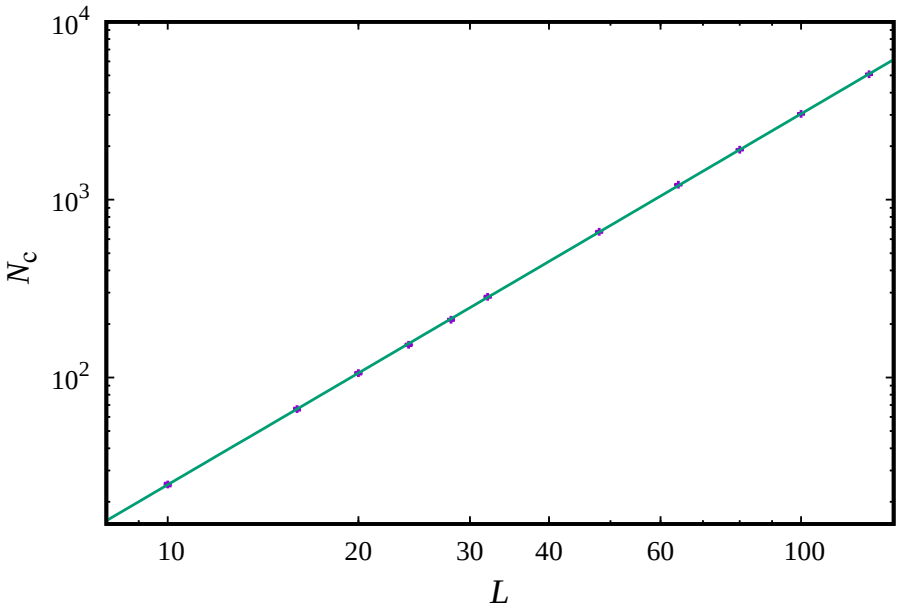

Figure 4.10: The average number of clusters N_c vs. system size L for systems with PFBCs. The result for each system size has been averaged over 1000 disorder realizations. Fitting data to the function $N_c(L) = aL^b$ gives us $a = 0.204 \pm 0.003$ and $b = 1.98 \pm 0.03$ with $Q = 0.30$.

results are shown in Fig. 4.10. By fitting the data to the function $N_c(L) = aL^b$ we obtained $a = 0.204 \pm 0.003$ and $b = 1.98 \pm 0.03$ with a reasonable value for the goodness-of-fit $Q = 0.30$. It is not surprising that the total number of clusters grows with the system size L in the same way as the number of spins of the system grows, i.e., $N_c \propto L^2$, otherwise we would have a problem at the thermodynamic limit[7].

The total number of spins of a system of size L is L^2 and since each spin can have two different orientations (up or down) then the total number of spin configurations of the system is 2^{L^2}. But when we consider the cluster configuration of the system, the number of clusters are almost $0.2L^2$ (in average) and the number of possible states would be $2^{0.2L^2}$. Therefore, the total number of possible states will be reduced by a huge factor, i.e., $2^{0.8L^2}$. As a result, the probability of finding the ground state will be increased, and the equilibration time will be decreased so larger systems can be studied in a reasonable time.

[7] It is because that the ratio between the number of clusters and the number of spins (N_c/L^2) in the thermodynamic limit would tend to zero or infinity for $b < 2$ and $b > 2$ respectively, which of course is not possible.

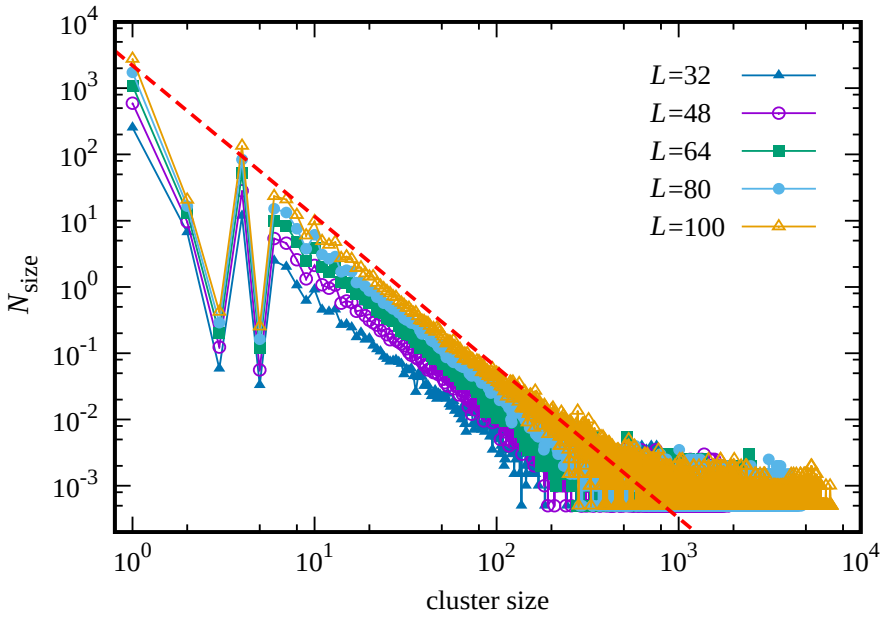

Figure 4.11: The average number of clusters for each size versus the size of the clusters averaged over 1000 realizations for each system size. The plot shows that by increasing the size of the clusters the average number of clusters decays. The dashed line is a guide to the eye and has a slope of 2.5.

4.3.2 Number of clusters of each size N_{size}

The average number of clusters of different size, N_{size}, is shown in Fig. 4.11. The data shows that most of the clusters of the system are free spins (clusters of size 1) and the number of bigger clusters decreases by increasing the size of the clusters. The dashed line in Fig. 4.11 is drawn to help us to visualize the relation between N_{size} and the size of the clusters. The line indicates a power low decay for the number of clusters of different size i.e. $N_{\text{size}} \propto L^{-\beta}$ with $\beta = 2.5$.

4.3.3 Equilibration time

Fig. 4.12 shows the value for the average energy, $\bar{E}$, averaged over M replicas of the system at the lowest temperature versus time for two disorder realizations of system sizes $L = 32$ and $L = 64$. We only consider the energy at the lowest temperature because it takes the longest for this temperature to equilibrate. The time is calculated in Monte Carlo steps (MCS), the time it takes for one complete cycle of parallel tempering with exchange clusters, i.e., doing $n = N_c^2$ simple Monte Carlo flips for all the $N \times M$ copies of the system, plus parallel tempering and the cluster-exchange moves.

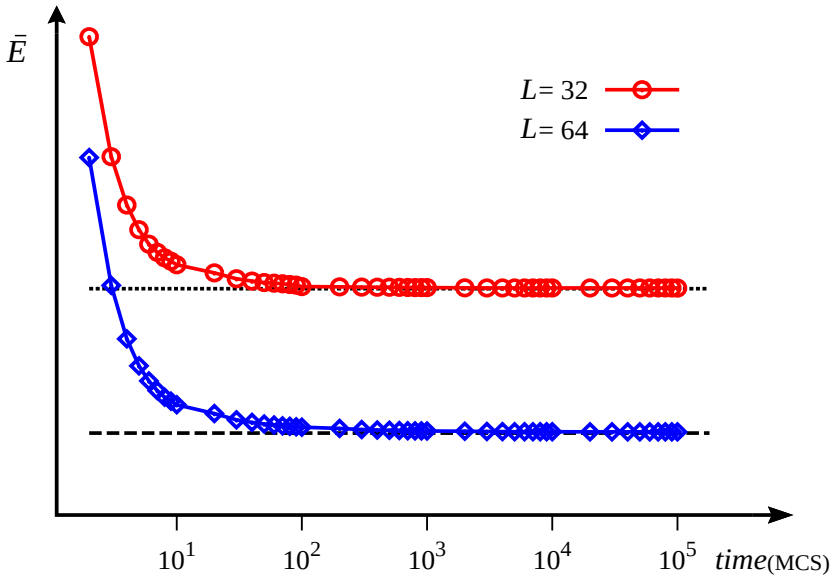

Figure 4.12: The time in Monte Carlo steps (MCS) taken for the equilibration of energy at the lowest temperature of two disorder realization of system sizes $L = 32$ and $L = 64$. The dotted line and dash line represent the ground state energy of system sizes $L = 32$ and $L = 64$ respectively.

As we can see in Fig. 4.12 after almost 10^2 MCS the energy of the system of size $L = 32$ does not change anymore which means the energy has been equilibrated. The dotted line in Fig. 4.12 shows the ground state energy of the disorder of size $L = 32$. Since we choose the lowest temperature in such a way that the system has a reasonable probability to be at the ground state, therefore the equilibrated value of the average energy at the lowest temperature is very close to the ground state energy. The same scenario occurs for a disorder realization of size $L = 64$ after almost 10^3 MCS[8]. The dashed line in Fig. 4.12 shows the ground state energy of the disorder realization of size $L = 64$. Our data shows that the equilibration time for system size $L = 128$ is of the order of 10^4 MCS.

4.3.4 Uniform sampling of ground states

For a given disorder realization, we first determine the exact cluster configuration of the system and then we use parallel tempering with exchange clusters to generate the ground states of the system. The set of the values of necessary

[8]We have calculated the equilibration time for the same disorder realizations using parallel tempering and the spin configuration (not the cluster configuration). In that case, the equilibration time was of the order of 10^4 and 10^6 MCS for the disorder of size $L = 32$ and $L = 64$ respectively.

parameters for this algorithm are summarized in section 4.2.4. The starting configuration of all the copies of the system are chosen randomly and Monte Carlo flips, followed by swapping temperatures and clusters exchange moves, will be done until the system reaches the equilibrium.

At the equilibrium, each of the configurations will be generated with a probability which depends only on the energy of the configuration and thus all the ground states will have the same probability to be generated. In order to see this explicitly, we consider some disorder realizations of size $L = 24$ which have different numbers of ground states N_{GS}, from $N_{\mathrm{GS}} = 32$ up to $N_{\mathrm{GS}} = 79488$. Fig. 4.13 shows the distribution of generated ground states, $P(\mathrm{GS})$, by our algorithm. Panel (a) of Fig. 4.13 shows the ground state distribution for a disorder realization with $N_{\mathrm{GS}} = 32$ ground states and the number of generated ground states, n_{gen}, for this realization is $n_{\mathrm{gen}} = 133550 \times N_{\mathrm{GS}}$. The dashed line indicates the theoretical result for a uniform sampling, in which $P(\mathrm{GS})$ is exactly the same for all the ground states. As the data in panel (a) of Fig 4.13 show, $P(\mathrm{GS})$ for the generated ground states by our algorithm is in very good agreement with the exact value with relatively small statistical fluctuations. In order to have a quantitative description for the uniformity of the ground state distribution $P(\mathrm{GS})$, we calcualate the χ^2 of the distribution defined as follows:

$$\chi^2 = \sum_{i=1}^{N_{\mathrm{GS}}} \frac{(O_i - e_i)^2}{e_i}.$$

Here, the sum runs over all the ground states, O_i is the observed (generated) number and e_i is the expected (exact) value for the i^{th} ground state. If the observed value is far from the expected value for the whole distribution then the value of χ^2 will be large and it shows that the observed distribution is not the same as it was expected to be. The number of ground states N_{GS} is usually referred as *the number of degrees of freedom* (n.d.f), and $\chi^2/\mathrm{n.d.f} \sim 1$ can be used as a measure of uniformity. The $\chi^2/\mathrm{n.d.f}$ for the disorder realization shown in panel (a) of Fig. 4.13 is 1.291 indicating that our algorithm has generated the ground states uniformly. The next disorder realization has $N_{\mathrm{GS}} = 48$ ground states and we have generated $n_{\mathrm{gen}} = 733881 \times N_{\mathrm{GS}}$ ground states for this realization. The distribution of generated ground states for this realization is shown in Fig. 4.13 (b) with $\chi^2/\mathrm{n.d.f} = 0.995$. Therefore the fluctuations of $P(\mathrm{GS})$ are in agreement with uniform sampling. Fig. 4.13 (c) shows $P(\mathrm{GS})$ for a disorder realization with $N_{\mathrm{GS}} = 96$ ground states. We have generated $n_{\mathrm{gen}} = 489572 \times N_{\mathrm{GS}}$ ground states for this realization and the fluctuations of $P(\mathrm{GS})$ from the exact uniform distribution result is $\chi^2/\mathrm{n.d.f} = 1.288$ indicating a good agreement with the uniform sampling.

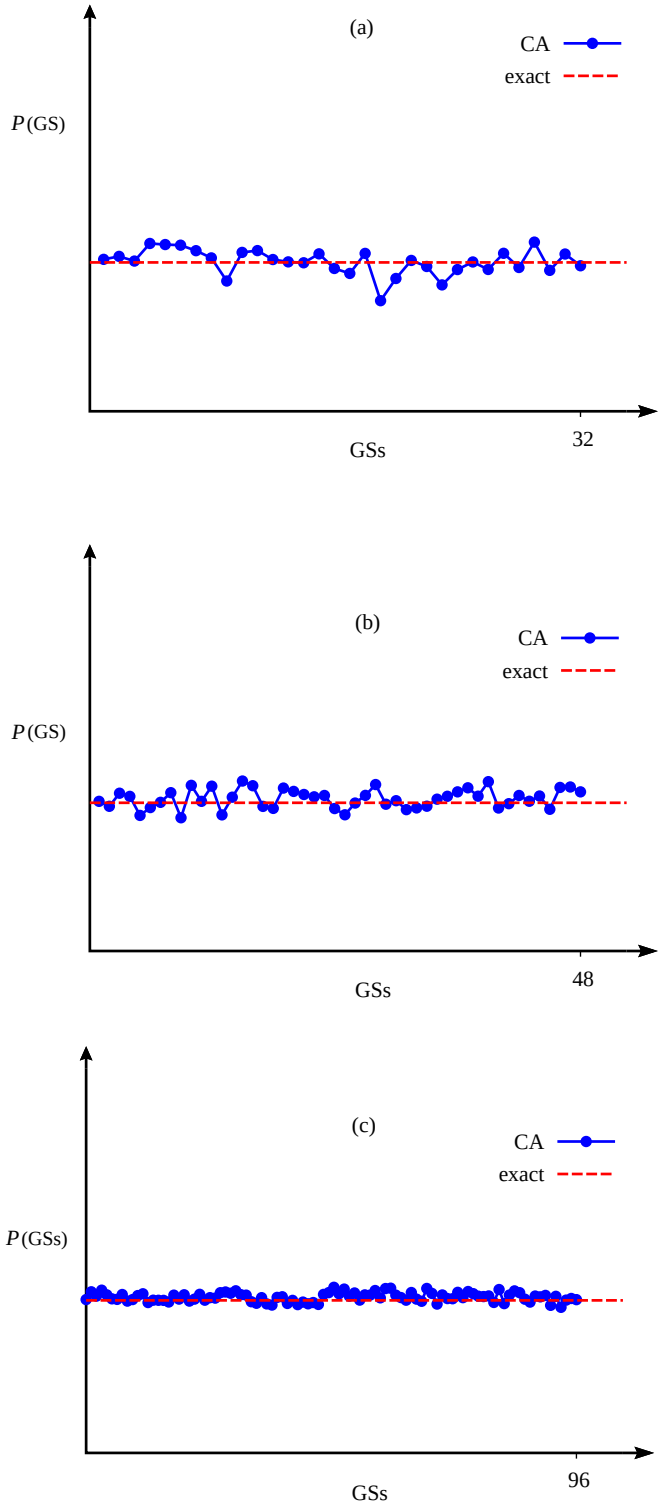

Figure 4.13: The distribution of generated ground states by our algorithm (CA) for three different disorder realizations of system size $L = 24$. (a) The realization has $N_{GS} = 32$ and we have generated $n_{gen} = 133550 \times N_{GS}$ ground states. The χ^2 value of the distribution is $\chi^2/\text{n.d.f} = 1.291$. (b) The realization has $N_{GS} = 48$ ground states, the number of generated ground states is $n_{gen} = 733881 \times N_{GS}$ and $\chi^2/\text{n.d.f} = 0.995$ for $P(\text{GS})$ of this realization. (c) The number of ground states for this realization is $N_{GS} = 96$ while $n_{gen} = 489752 \times N_{GS}$ ground states has been generated and $\chi^2/\text{n.d.f}$ for the distribution of the ground states is 1.288.

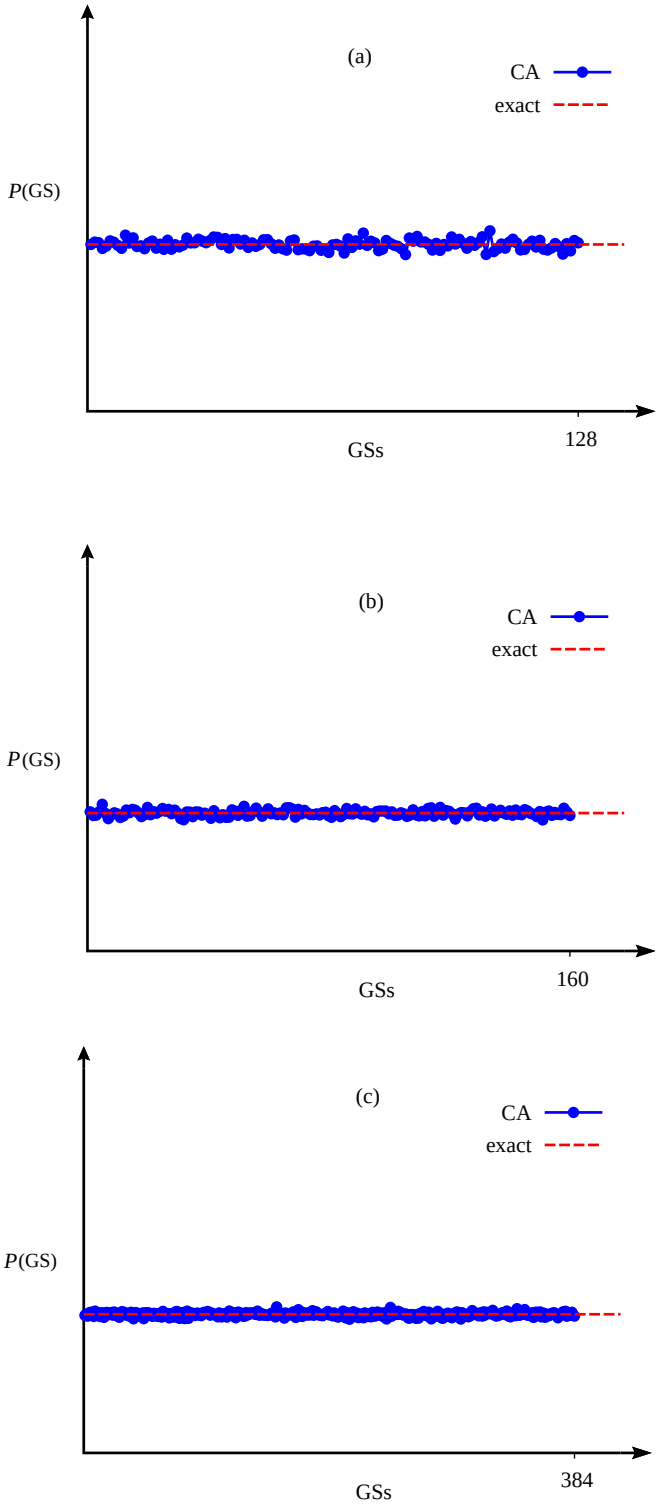

Figure 4.14: The distribution of generated ground states by our algorithm (CA) for three different disorder realizations of system size $L = 24$. (a) The realization has $N_{\mathrm{GS}} = 128$ and we have generated $n_{\mathrm{gen}} = 227371 \times N_{\mathrm{GS}}$ ground states. The χ^2 value of the distribution is $\chi^2/\mathrm{n.d.f} = 0.968$. (b) The realization has $N_{\mathrm{GS}} = 160$ ground states, the number of generated ground states is $n_{\mathrm{gen}} = 328725 \times N_{\mathrm{GS}}$ and $\chi^2/\mathrm{n.d.f} = 1.097$ for $P(\mathrm{GS})$ of this realization. (c) The number of ground states for this realization is $N_{\mathrm{GS}} = 384$ while $n_{\mathrm{gen}} = 125257 \times N_{\mathrm{GS}}$ ground states has been generated and $\chi^2/\mathrm{n.d.f}$ for the distribution of the ground states is 0.950.

Fig. 4.14 contains three more disorder realizations with larger number of ground states. The realization shown in panel (a) of Fig. 4.14 has $N_{\mathrm{GS}} = 128$ ground states and we have generated $n_{\mathrm{gen}} = 227371 \times N_{\mathrm{GS}}$ while the realization of panel (b) has $N_{\mathrm{GS}} = 160$ ground states and $n_{\mathrm{gen}} = 328725 \times N_{\mathrm{GS}}$, and finally the number of generated ground states is $n_{\mathrm{gen}} = 125257 \times N_{\mathrm{GS}}$ for the realization shown in panel (c) which has $N_{\mathrm{GS}} = 384$ ground states. As we can see from Fig. 4.14 all of these distributions are very close to the exact uniform distribution. The value of χ^2/n.d.f for panel (a), panel (b) and panel (c) of Fig. 4.14 are 0.968, 1.097 and 0.950 respectively.

The statistical fluctuations of all different ground-state distributions of Fig. 4.13 and Fig. 4.14 are in agreement with uniform sampling and result in a reasonable value for χ^2 for the distributions. The statistical fluctuations are expected to become smaller by increasing the number of generated ground states n_{gen}. In order to check this property for our algorithm, we consider a disorder realization with large number of ground states N_{GS}, and we generate $n_{\mathrm{gen}} = m \times N_{\mathrm{GS}}$ ground states with different values for m to see how the fluctuations of $P(\mathrm{GS})$ change with m. Fig. 4.15 shows another disorder realization with $N_{\mathrm{GS}} = 79488$ ground states, for which we have generated $n_{\mathrm{gen}} = m \times N_{\mathrm{GS}}$ ground states for three different values of m, $m = 195$, $m = 10^3$ and $m = 10^4$. As we can see from Fig. 4.15 all the distributions for different values of m are distributed around the exact value and the statistical fluctuations decrease by increasing the value of n_{gen} as expected. The χ^2/n.d.f for the distribution with $n_{\mathrm{gen}} = 195 \times N_{\mathrm{GS}}$ is 1.378, for the distribution with $n_{\mathrm{gen}} = 10^2 \times N_{\mathrm{GS}}$ is 1.224 and we have χ^2/n.d.f = 1.340 for the distributions with $n_{\mathrm{gen}} = 10^3 \times N_{\mathrm{GS}}$ generated ground states indicating that our algorithm generates the ground states uniformly.

4.3.5 Fractal dimension for $\pm J$ spin glasses in 2D

After being sure that our algorithm generates the ground states of $\pm J$ spin glasses in 2D uniformly, we are able to investigate one of the properties of these systems, i.e., the fractal dimension d_{f} of domain walls. As we discussed in chapter 3, the definition of the domain wall for spin glasses with Gaussian bond distribution is straightforward as the ground state of the systems with both periodic (P) and anti-periodic (AP) boundary conditions are unique. However, the ground state of the systems with $\pm J$ couplings is degenerate, which means there are some clusters of spins (often called bubbles) that can be flipped without increasing the energy of the system. The presence of free clusters of spins in the manifold of degenerate ground states complicates the identification of domain walls for the bimodal model [150]. A possible difference in configuration between the ground state for a disorder configuration with P boundaries and a ground state for the

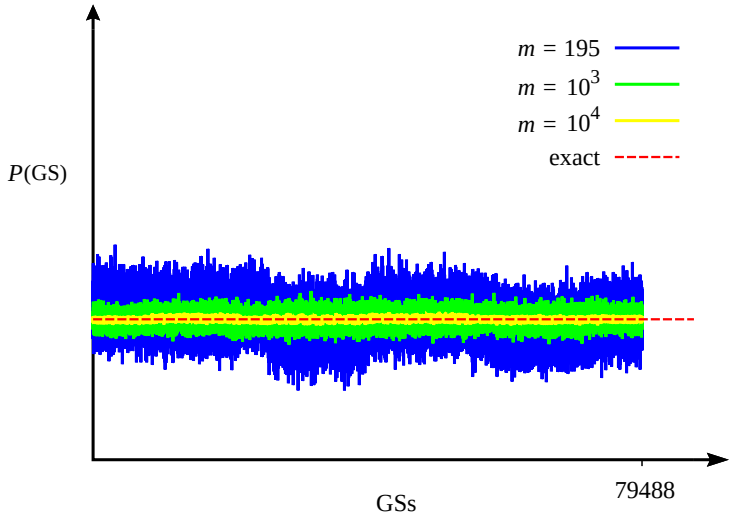

Figure 4.15: The distribution of generated ground states by our algorithm for a disorder realization of system size $L = 24$ and $N_{\mathrm{GS}} = 79488$ ground states. The number of generated ground states is $n_{\mathrm{gen}} = m \times N_{\mathrm{GS}}$.

same realization with AP boundary conditions is schematically depicted in the left panel of Fig. 4.16. We see that in this case the set of domain-wall bonds satisfying condition (3.4.6), i.e., different relative orientations of spins at both ends for the P and AP configurations, does not only contain the actual domain wall but also a set of closed loops detached from the wall. These correspond to free clusters that can be overturned at zero energy cost and so happen to be in one orientation in the P ground state, but in the opposite orientation in the AP configuration. Conceptually, these bonds do not belong to the domain wall. We remove them by only counting the system spanning part of the set $\mathcal{D}$. We refer to the corresponding set, denoted as $\mathcal{D}_{\mathrm{long}}$, as the "long" domain wall and its length as $\ell_{\mathrm{long}} = |\mathcal{D}_{\mathrm{long}}|$. Additionally, however, it is possible for such free clusters to be attached to the domain wall as is also depicted in the example of Fig. 4.16. Such "bubbles" attached to corners of the wall are somewhat arbitrary additions and removing them by only considering the shortest path in the set $\mathcal{D}$ connecting opposite ends of the system defines the reduced set $\mathcal{D}_{\mathrm{short}}$ with $\ell_{\mathrm{short}} = |\mathcal{D}_{\mathrm{short}}|$. Clearly we have that $\mathcal{D}_{\mathrm{short}} \subseteq \mathcal{D}_{\mathrm{long}} \subseteq \mathcal{D}$. Note that even after these removals the set $\mathcal{D}_{\mathrm{short}}$ is not unique for a given bond configuration, and the additional degeneracy is connected to zero-energy loops that share (at least) one bond with the domain wall (instead of only sharing a corner) and hence can be interpreted as diversions of the wall. In order to probe the equilibrium properties, we must sample from such walls with equal probability.

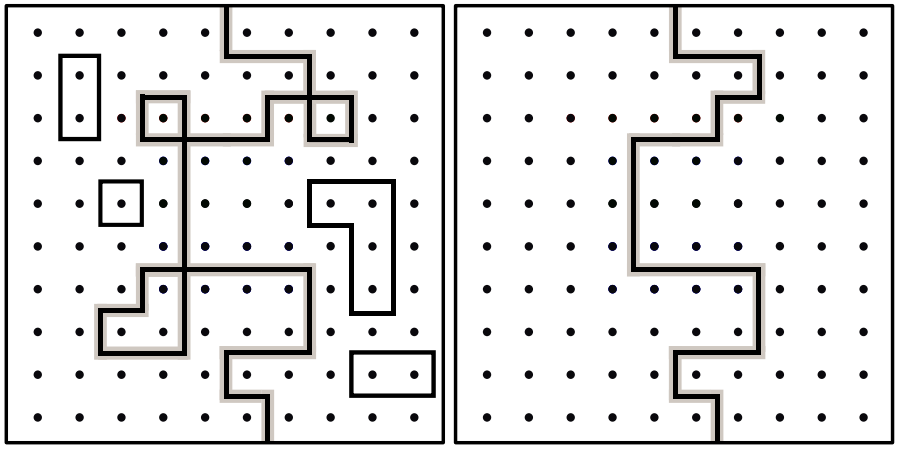

Figure 4.16: Left: Schematic representation of the set of dual bonds satisfying the condition (3.4.6) for the case of bimodal couplings. Besides the domain wall it contains isolated loops enclosing free clusters of spins as well as bubbles of free spins attached to the domain wall. Removing the isolated free loops one arrives at the set $\mathcal{D}_{\text{long}}$, which we denote as the "long" domain wall. Right: After the additional removal of bubbles one arrives at the set $\mathcal{D}_{\text{short}}$ of dual bonds comprising the "short" domain wall of the configuration.

Regarding the sampling of domain-wall lengths for the bimodal model we have produced data from three different algorithms:[9]

1. The implementation of the MWPM algorithm calculates a ground-state for each sample with both P and AP boundary conditions, and comparing these we can determine the lengths ℓ_{short} and ℓ_{long} of the related domain walls. It is clear that this does not correspond to a fair sampling of ground states, but the nature of the bias depends on internal details of the MWPM implementation [115] and is not clear on a physical level. This technique allows the treatment of large system sizes and we applied it to the data set of sizes $8 \leq L \leq 3000$ described in the third column of Table 3.4. In the following, we denote this as the "matching" algorithm.

2. The Gaussian noise technique described in Sec. 4.1 is designed to break the degeneracy in a systematic way. For each realization it only requires an additional run of the MWPM algorithm per boundary condition, and we hence applied it to the same set of samples with $8 \leq L \leq 3000$. As discussed in Sec. 4.1 it also does not provide uniform samples, however. This technique is referred to as "Gaussian noise" in the following.

3. Our new algorithm based on a cluster decomposition and parallel tempering provides uniform samples, but it is much more demanding computationally,

[9] The results of this and the following section previously appeared in Ref. [53].

such that only smaller system sizes can be treated reliably. We have studied systems of edge lengths $L = 10$, 16, 20, 24, 28, 32, 48, 64, 80, 100, and 128 for this method, using 1000 samples per size and producing ten independent ground-state configurations per sample. Data from this algorithm is labelled "uniform sampling".

Figure 4.17(a) shows the three data sets for the scaling of the lengths of short domain walls. On the scale of the domain-wall lengths themselves, all data appear to fall on top of each other, but a closer inspection reveals that this is in fact not the case. The data from uniform sampling show very clean scaling behavior and a pure power law $\langle \ell \rangle_J = A_\ell L^{d_\mathrm{f}}$ describes the data for $L \geq L_\mathrm{min} = 16$ well. No drift of the exponent value is observed on omitting further values on the small-L side. The fractal dimension is estimated from this fit as

$$d_\mathrm{f} = 1.279(2),$$

with $Q = 0.33$. As the inset of Fig. 4.17(a) shows, there are statistically significant deviations of the data from the other two sampling techniques from this result. The samples generated by the Gaussian noise technique show clean scaling as well, but with a significantly larger exponent $d_\mathrm{f} = 1.323(3)$ ($L_\mathrm{min} = 16$, $Q = 0.86$). The data from the matching approach alone, on the other hand, show somewhat inconsistent behavior for successive system sizes, and they are compatible with a pure power law only for $L \geq L_\mathrm{min} = 80$, yielding $d_\mathrm{f} = 1.2802(5)$ ($Q = 0.18$). This slightly unsteady statistical behavior is probably connected to the fact that the matching technique does not use a stochastic sampling technique, and due to internal design decisions the behavior of the algorithm might change discontinuously at certain system sizes. Somewhat surprisingly, however, the results for the pure matching technique are closer to the correct result represented by uniform sampling than the samples produced by Gaussian noise, see also the inset of Fig. 4.17(a).

We move on to considering the results for the long domain walls. The data is summarized in Fig. 4.17(b). While for each data set, the values of $\langle \ell_\mathrm{long} \rangle_J$ are somewhat larger than those of $\langle \ell_\mathrm{short} \rangle_J$ the relative behavior of the three data sets for the long domain walls is very similar to that found for the short walls. From the uniform sampling data, a pure power-law fit for $L_\mathrm{min} = 16$ yields $d_\mathrm{f} = 1.281(3)$ ($Q = 0.97$) which is statistically consistent with the result from the short domain walls. For comparison, matching and Gaussian noise yield $d_\mathrm{f} = 1.2797(5)$ and $d_\mathrm{f} = 1.325(3)$, respectively, for the same ranges that were used for the short walls. It hence appears that for the scaling of domain-wall length with system size, there is no difference between the short and long definitions of domain walls. This impression is corroborated by the data shown in Fig. 4.17(c) of the ratios of long and short lengths of domain walls, averaged over disorder, for the three different

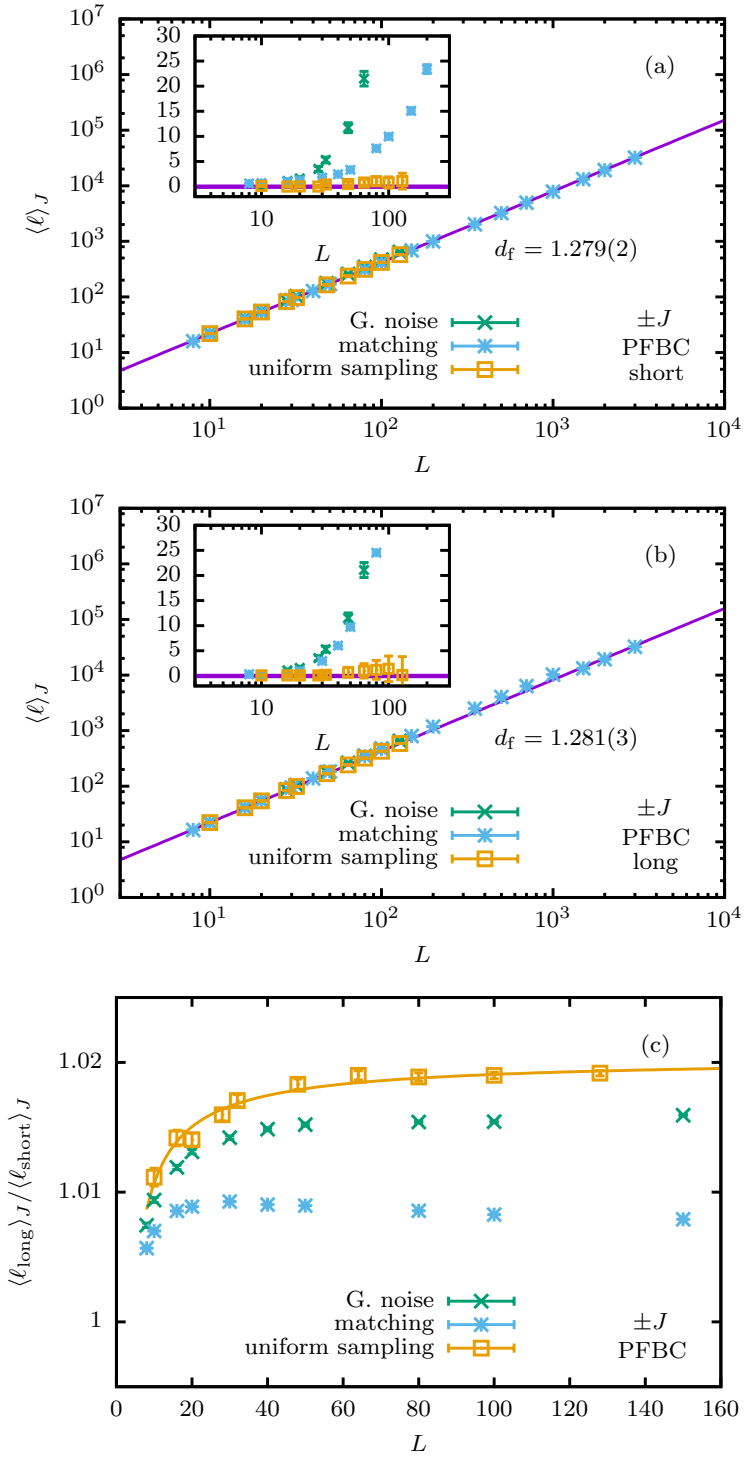

Figure 4.17: (a) Average length $\langle \ell_{\text{short}} \rangle_J$ of the short domain wall for the bimodal model as a function of linear system size L for the three different algorithms employed. The inset shows the deviation of each data set from the fit of the power law $\langle \ell \rangle_J = A_\ell L^{d_f}$ to the uniform sampling data for $L \geq L_{\text{min}} = 16$, which results in $d_f = 1.279(2)$ ($Q = 0.33$). (b) Average length $\langle \ell_{\text{long}} \rangle_J$ of the long domain walls for the different algorithms. The inset shows the deviation of each data set from the fit of a pure power law to the uniform data, yielding $d_f = 1.281(3)$ for $L_{\text{min}} = 16$ ($Q = 0.97$). (c) Ratio of the average lengths of long and short domain walls as estimated from the different algorithms. In all cases, the ratio approaches a constant, in line with the identical estimates of fractal dimension for ℓ_{short} and ℓ_{long}.

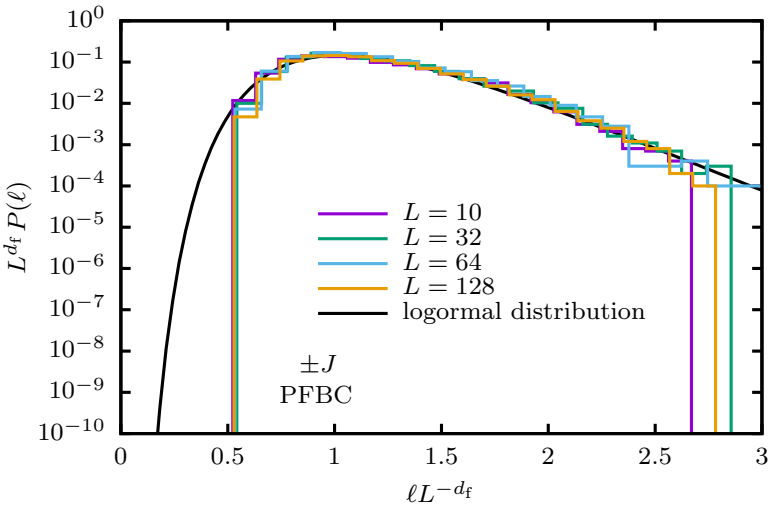

Figure 4.18: Distribution of the lengths ℓ_{long} of the long domain walls for $\pm J$ couplings and PFBC boundaries as resulting from the uniform sampling approach. The re-scaling of the axes is with respect to the fractal dimension $d_f = 1.281(3)$ estimated from the data in Fig. 4.17.

techniques. It is clear that this ratio settles down to a finite value as $L \to \infty$, and a fit of the function form $\langle \ell_{\text{long}}/\ell_{\text{short}} \rangle_J = \kappa + A_\kappa L^{-\omega}$ to the uniform sampling data yields $\kappa = 1.021(6)$ and $\omega = 0.85(16)$ with $Q = 0.18$ ($L_{\text{min}} = 10$).

It is worthwhile to compare these estimates of the fractal dimension to those found previously: Melchert and Hartmann [20] used combinatorial optimization methods to find minimal and maximal domain walls in the manifold of degenerate ground-state pairs, yielding lower and upper bounds for d_f, namely $1.095(2) \leq d_f \leq 1.395(3)$. Our estimates are clearly compatible with these, and it is interesting to note that the actual value is much closer to the upper than to the lower limit which corresponds to almost flat walls. Risau-Gusman and Romá [150] estimate $d_f = 1.323(3)$ using non-uniform sampling resulting from employing the bare MWPM algorithm; this is compatible with our "matching" results, but too large compared to the unbiased estimate from uniform sampling. Studying domain walls in a hexagonal lattice, Weigel and Johnston [138] find $d_f = 1.283(11)$, but again not using unbiased sampling. Analyzing the behavior of the ground-state entropy, Fisch [158] estimates $d_f = 1.22(1)$ which is strongly incompatible with our results, which could be a sign of the relation $d_f = 2\theta_S$ on which Fisch's estimate is based, where θ_S is the scaling exponent of the ground-state entropy, not being valid in two dimensions.

We finally tend to the distribution of domain-wall lengths for this case. As is illustrated in Fig. 4.18 for the long domain walls, these follow the scaling form $P(\ell) = L^{d_f} \hat{P}(\ell L^{-d_f})$ already observed for the case with Gaussian couplings, cf. Fig. 3.10(c), where now $d_f = 1.281(3)$. The fit to a log-normal distribution also

shown in Fig. 4.18 works quite well over the full range of the distribution, in contrast to the case of Gaussian couplings, where deviations could be seen in the right tail, cf. Fig. 3.10(c). Very similar results are obtained for the distribution of short domain walls also, so we do not show them here.

4.3.6 Ground-state and defect energies

For the ground-state energy the presence of degeneracies and sampling bias is not relevant. We hence used the regular MWPM procedure to determine ground-state energies for pairs of samples with periodic and antiperiodic boundaries and the resulting defect energies. For these quantities we restricted our calculations to the case of PFBC as this allows for treating larger system sizes, but studies of PPBC would also be possible using the windowing technique. The range of system sizes and number of realizations for each size are summarized in the fourth column of Table 3.4. The average ground-state energy per spin is shown in Fig. 4.19(a). Inspecting the general scaling ansatz (3.4.3) and taking into account that we expect $\theta = 0$ for this model (see below), we should only have analytical corrections proportional to $1/L$ and $1/L^2$ up to $O(L^{-3})$, and indeed we find a good fit ($Q = 0.18$) of this functional form for the range $L \geq L_{\min} = 20$, yielding

$$e_\infty = -1.401\,922(3).$$

This fit is shown together with the data in Fig. 4.19(a). No drift of e_∞ is visible on further increasing $L_{\min}$.

The defect energies resulting from this procedure are shown in Fig. 4.19(b), indicating that for this model $\langle|\Delta E|\rangle_J$ converges to a finite value instead of decaying away to zero. This is consistent with previous findings [75, 159]. If we assume a power-law decay as prescribed by Eq. (3.4.5) and ignore the correction terms, i.e., we use a pure power-law form $\langle|\Delta E|\rangle_J = A_\theta L^\theta$, a good fit is achieved for $L \geq L_{\min} = 150$, resulting in $\theta = -0.012(4)$, marginally compatible with $\theta = 0$. Additionally, the modulus of θ systematically drops as $L_{\min}$ is increased. The defect energy in this case hence does not decay to zero, but attains a non-zero value in the thermodynamic limit. We therefore make the scaling ansatz

$$\langle|\Delta E|\rangle_J = \Delta E_\infty + B_\theta L^{-\omega}. \tag{4.3.1}$$

We find an excellent fit with $Q = 0.99$ already for $L_{\min} = 10$, resulting in

$$\Delta E_\infty = 0.960(5)$$

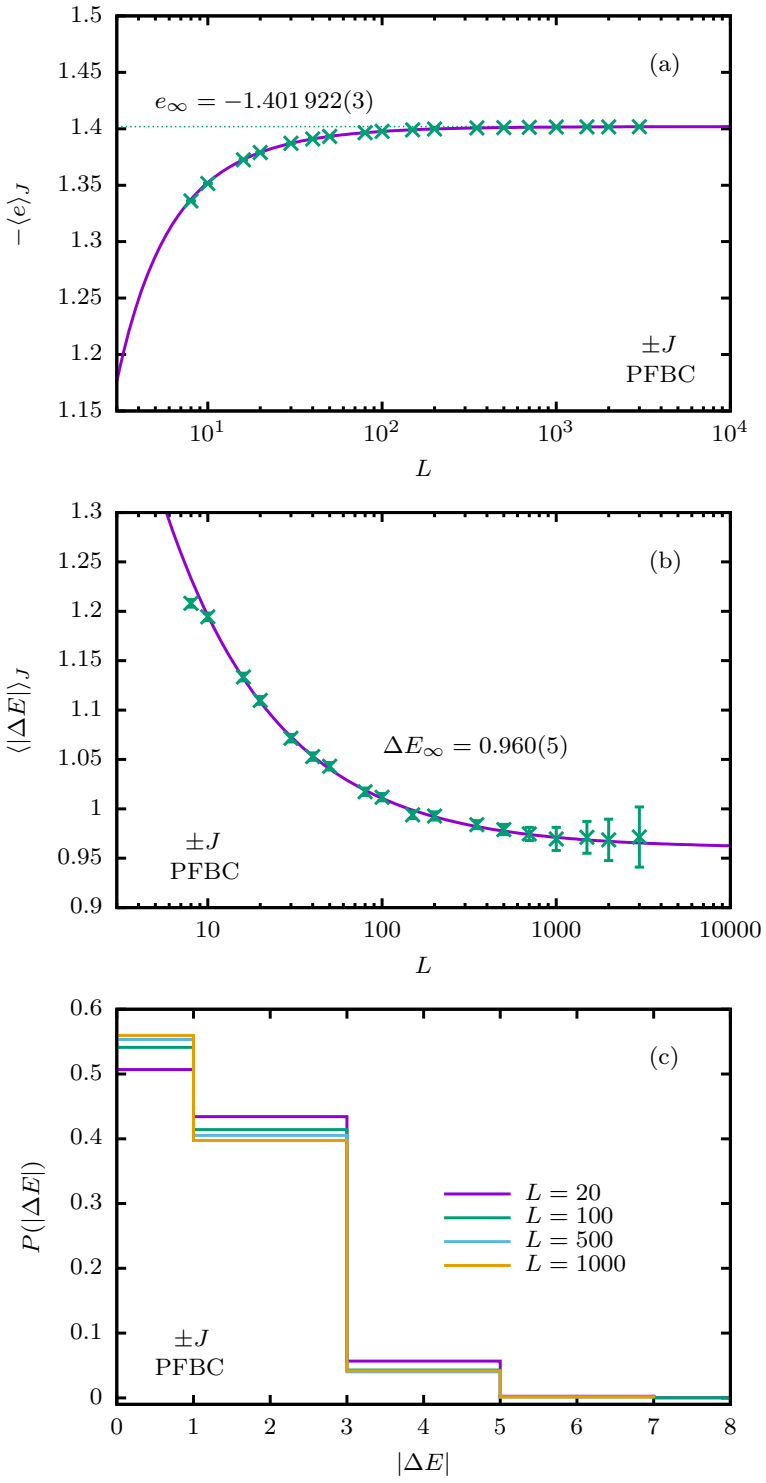

Figure 4.19: (Color online) (a) Average ground-state energies for bimodal couplings and PFBC boundaries, together with a fit of the functional form (3.4.3) with $\theta = 0$ to the data for the range $L = 20, \ldots, 3000$. (b) Defect energies for systems with bimodal couplings and PFBC boundaries. Clearly, $\langle|\Delta E|\rangle_J$ converges to a non-zero value as $L \to \infty$, indicating that $\theta = 0$. The line shows a fit of the form $\langle|\Delta E|\rangle_J = \Delta E_\infty + B_\theta L^{-\omega}$ to the data with $L \geq L_{\min} = 10$ yielding $\Delta E_\infty = 0.960(5)$. (c) Probability distribution over disorder of the defect energies for the PFBC $\pm J$ model and different system sizes. For $L \to \infty$ the distribution approaches a limiting shape close to the $L = 1000$ case shown here.

and $\omega = 0.67(4)$. An alternative fit form including analytic corrections proportional to $1/L$ and $1/L^2$ but omitting the $L^{-\omega}$ term is found to be of significantly lower quality.

Studying the distributions of both ground-state and defect energies, we again find a Gaussian shape for the ground-state energies, the kurtosis being compatible with that of a normal distribution for all system sizes studied. The standard deviation of the defect energy shows analogous behavior to $\langle|\Delta E|\rangle_J$, settling down at a finite value as $L \to \infty$. A fit of the form (4.3.1) yields an asymptotic $\sigma_\infty(\Delta E) = 1.1564(4)$ ($L_{\min} = 16$, $Q = 0.41$). The disorder distribution of defect energies is shown in Fig. 4.19(c), illustrating that it approaches a limiting shape as $L \to \infty$ in which about 57% of domain walls have zero energy, 38% have $\Delta E = 2$, 4% have $\Delta E = 4$, and higher defect energies occur in less than 1% of the cases.

4.4 Summary and conclusion

In this chapter, we have continued studying the two-dimensional Ising spin glasses at zero temperature, while our focus was only on the systems with bimodal bond distribution. The properties of these systems which are related to the energy, such as ground-state energy of the defect energy, can be fully studied using the algorithms based on MWPM. However the study of the properties of the system which are related to the ground-state spin configuration, such as magnetization or the domain-wall length, is challenging. The challenge arises due to the fact that the ground state of these systems is hugely degenerate, and such properties can vary from one ground-state configuration to another. Therefore, in order to study those properties we either need to have all the ground states or we need to have an unbiased sample of the ground states. None of these cases were actually possible as in the first case, it is known that the number of the ground states grows exponentially by the system size and therefore generating all of them is not possible in a reasonable time (except for very small systems only), and for the second case, methods based on matching do not allow to sample states with the proper statistical weight. As the result, unbiased studying of the ground-state dependent properties of these systems has not been possible.

In order to overcome this problem, we have developed a new algorithm to generate the ground states of these systems uniformly. Our algorithm is based on a combination of combinatorial optimization in the form of the MWPM algorithm and Markov chain Monte Carlo [151]. We use the MWPM to determine the exact cluster configuration of the system, and in the second step, we perform a parallel tempering simulation [156] with updates that are a combination of flipping individual rigid clusters and a non-local cluster-update move [157]. Our algorithm

allowed us to sample exact ground states for this case uniformly, here up to system size $L = 128$. The resulting estimates of the fractal dimension, $d_f = 1.279(2)$ and $d_f = 1.281(3)$ for "short" and "long" domain walls, respectively, are marginally consistent with d_f for the Gaussian couplings discussed in chapter 3, the deviation being 3 and 4 standard deviations, respectively.

We have also studied the ground-state energy of the 2D Ising spin glasses with $\pm J$ couplings, and obtained $e_\infty = -1.401\,922(3)$ for the asymptotic ground-state energy. Our results for the defect energy showed that $\langle|\Delta E|\rangle_J$ attains a non-zero value in the thermodynamic limit, and it be described very well by the scaling form $\langle|\Delta E|\rangle_J = \Delta E_\infty + B_\theta L^{-\omega}$, resulting in $\Delta E_\infty = 0.960(5)$ and $\omega = 0.67(4)$. This scaling form indicates that the stiffness exponent vanished for these systems, i.e., $\theta = 0$. Our results for the fractal dimension of the bimodal model are marginally consistent with those for the Gaussian model, and it remains an interesting question for further studies whether universality between the two models holds in this respect.

Chapter 5

Domain walls in spin glasses as SLE traces

5.1 Introduction

We have already seen that domain walls of the two-dimensional Ising spin glass are scale invariant, and the domain-wall length scales with the system size L as L^{d_f} where d_f is the fractal dimension. Recent works, including our estimates shown in chapters 3 and 4, show that $d_f \approx 1.27$ for the Gaussian bond distribution (c.f. Table 3.5) and $1.09 \lesssim d_f \lesssim 1.39$ for the bimodal model [20]. In the previous chapters, we checked the validity of the conjecture between the fractal dimension and the stiffness exponent of Ising spin glasses, i.e., $d_f = 1 + 3/[4(3+\theta)]$ [Eq. (3.4.9)]. We treated very large system sizes and obtained high precision estimates for both the stiffness exponent and the fractal dimension. Our data does not appear to be consistent with that conjecture.

In the present chapter we investigate the SLE properties of the two-dimensional Ising spin glass. The interest in SLE related to this system arises from the fact that SLE provides a unified description of domain boundaries of many lattice models in 2D [160], and it enables us to study these problems analytically, obtain exact results for critical exponents, and also attain more subtle geometric properties. For example, it has been shown rigorously that the domain boundaries in percolation and the Ising model (without quenched disorder) are compatible with SLE, regardless of the type of boundary conditions of the system [94, 161]. For some other models, for instance the loop-erased random-walk, however, the system can be described by SLE only for certain boundary conditions and not for others [101]. For the two-dimensional spin glass, a general consistency of domain walls with SLE has already been observed [18, 91], but the situation of the sensitivity of the SLE properties of this system to boundary conditions is still open.

Our aim in this chapter is to figure out whether the domain walls of the 2D spin glass for both continuous and discrete couplings can be described by SLE, and whether or not changing the boundary conditions may have any effects on the SLE properties of the domain walls. Therefore our focus will be on the domain walls (and not the energy) of this system. The goal of this chapter is to investigate the possibility of describing the domain walls of these systems with various boundary conditions using SLE_κ. Different boundary conditions and different bond distributions are considered. For each case, the SLE diffusion constant κ of the relative Brownian motion is calculated using two different methods (left passage probability and Loewner map), and we will check whether the SLE relation between κ and d_f , i.e.,

$$d_\mathrm{f} = 1 + \frac{\kappa}{8},$$

is fulfilled [Eq. (2.5.9)]. In addition, we check the domain Markov property of the domain walls by considering the test of independent increments.

This chapter is organized as follows: we first present a short review of the methods we have used in section 5.2 and we describe how different parameters have been calculated. The way of implementing different boundary conditions and determination of the domain walls are also described in this section. All the calculations and results will be discussed in section 5.3. At the end, the summary and conclusions are presented in Sec. 5.4.

5.2 Methods

5.2.1 Left passage probability

Let us recall some properties of the left passage probability (see Sec. 2.5.1). Consider $\mathbb{H}$ to be the upper half plane and a continuous simple random curve γ_t which grows in time t. Instead of studying γ_t directly, one can imagine a growth process defined via conformal maps $g_t : \mathbb{H} \setminus \gamma_t \to \mathbb{H}$ which are solutions of Loewner's equation:

$$\frac{\partial g_t(z)}{\partial t} = \frac{2}{g_t(z) - \xi_t}, \tag{5.2.1}$$

where ξ_t is the driving function. It was shown by Schramm [106] that if the ensemble of curves γ_t is conformally invariant and satisfies the domain Markov property, then the driving function ξ_t is proportional to one-dimensional Brownian motion B_t, i.e., $\xi_t = \sqrt{\kappa} B_t$ where κ is the diffusion constant of the corresponding Brownian motion. Although changing the diffusion constant κ does not change the behavior of Brownian motion qualitatively, it alters the behavior of SLE drastically.

For such processes in chordal SLE, if the curves start at the origin of the upper half plane $\mathbb{H}$, the probability $P_{LP}^{\kappa}(x,y)$ that the curve γ_t passes to the left of the point (x,y) can be written as:

$$P_{\mathrm{LP}}^{\kappa}(x,y) = \frac{1}{2} + \frac{\Gamma(4/\kappa)}{\sqrt{\pi}\,\Gamma\left(\frac{8-\kappa}{2\kappa}\right)} \frac{x}{y} {}_2F_1\left(\frac{1}{2}, \frac{4}{\kappa}; \frac{3}{2}; -\left(\frac{x}{y}\right)^2\right), \tag{5.2.2}$$

where ${}_2F_1$ is Gauss' hyper-geometric function (see section 2.5.1).

In order to examine the agreement of the domain walls of the two-dimensional Ising spin glass with the SLE expectations for the left passage probabilities, the domain wall of the lattice is forced to run through the diagonal, i.e, from the bottom left corner to the upper right corner, by fixing the spins at the boundaries[1]. The bottom left and the upper right corners of the system are then mapped to the origin and to infinity in $\mathbb{H}$, respectively. For a quantitative comparison, the mean square deviation of the computed left passage probability P_{LP}^{c} from the exact result P_{LP}^{κ} of Eq. (5.2.2) is considered

$$E(\kappa) = \left\langle \left[P_{\mathrm{LP}}^{c}(x,y) - P_{\mathrm{LP}}^{\kappa}(x,y)\right]^2 \right\rangle_{\mathbb{D}}^{1/2}, \tag{5.2.3}$$

where $\langle \cdots \rangle_{\mathbb{D}}$ denotes a spatial average over the domain $\mathbb{D}$, excluding the vicinity of the fixed spins at the boundaries [160]. The value of κ which minimizes the $E(\kappa)$ is considered as the appropriate value of the diffusion constant of the relative Brownian motion.

5.2.2 Loewner map

In this method, the possibility of characterizing the domain walls of the spin glass systems is checked by generating the driving function ξ_t. According to Eq. (5.2.1), the family of maps g_t is realized as a discrete series of maps g_i iteratively removing a small segment from the beginning of the curve. By using a vertical slit map [162], g_i is approximated as[2]

$$g_i(z) = \sqrt{(z-\xi_i)^2 + 4\Delta t_i} + \xi_i, \tag{5.2.4}$$

where $z = x + iy$, $\xi_i = x_{i,i-1}$ and $\Delta t_i = y_{i,i-1}^2/4$. The parameter ξ_i is the value of the driving function ξ_t sampled at time[3] $t_i = \sum_{j\le i} \Delta t_j$, and $x_{i,i-1}$ and $y_{i,i-1}$ are the coordinates of the i'th segment of the curve after undergoing the $i-1$ successive maps $g_{i-1} \circ \ldots \circ g_1$. The complex square root in Eq. (5.2.4) is calculated, as usual, with the branch cut along the negative real axis [160]. This transformation maps

[1] The methods for fixing the spins at the boundaries are explained in section 5.2.4

[2] The origin of this equation is explained in section 2.3.1.

[3] This time is known as *Loewner time*.

the random curve to a one-dimensional Brownian motion, i.e., ξ_t, with zero mean and variance κt. Therefore the value of κ is simply the slope of the $\langle \xi^2(t) \rangle_J$ versus Loewner time t in which, as usual, $\langle \cdots \rangle_J$ means the average over disorder realizations.

5.2.3 Test of independent increments

Since the driving function ξ_t is a Brownian motion with zero mean and variance κt in SLE traces, every increment of the driving function must have a Gaussian distribution and be independent of all other increments. In order to check this property for domain walls of the 2D Ising spin glass, we use the test of independent increments based on χ^2 goodness-of-fit [163].

Consider a stochastic process ξ_t and the time intervals $t_1, \ldots, t_n$ such that $0 < t_1 < t_2 < \cdots < t_n$. If ξ_t is Brownian motion, then the increments $X_i = \xi_{t_i} - \xi_{t_{i-1}}$ are independent and each is normal with mean zero and variance $\kappa(t_i - t_{i-1})$. The possible values of the set $(X_1, X_2, \ldots, X_n)$ are then considered and divided into m different cells. Under the hypothesis that the X_i are independent and normally distributed, the expected number of samples that fall into each cell can be computed. If O_i represents the observed number of samples that fall into cell i and E_i is the expected value of the number of samples in cell i, then we construct the test based on the statistic:

$$\chi^2 = \sum_{i=1}^{m} \frac{(O_i - E_i)^2}{E_i}. \tag{5.2.5}$$

If m is large enough, then under the hypothesis that the driving function $\xi_i(t)$ is Brownian motion, the distribution of the above statistic is approximately a χ^2 distribution with $m-1$ degrees of freedom. Therefore only if the increments X_i are independent then the fluctuations would have the right value to be described by a χ^2-distribution. Once this statistic is calculated, it would be easier if we look at its corresponding "p-value" rather than the value of the statistic, because everything can be described in terms of probabilities. The p-value is simply the probability of getting such extreme value for χ^2 when the increments are independent (our Null hypothesis). If the p-value is close to zero, we conclude that the observed test result would be unlikely for independent variables, so there is evidence that the variables are correlated. Generally speaking, the p-value is interpreted as follows[4] [164]:

- $0.1 \lesssim p$-value: no evidence against the null hypothesis (independence of increments in our case)

[4]There is also a significant level associated to this interpretation which usually considered as 0.05. It means that there is a 5% risk of concluding that a difference exists when there is no actual difference.

- $0.05 \lesssim p$-value $\lesssim 0.1$: very weak evidence of dependence between the increments
- $0.01 \lesssim p$-value $\lesssim 0.05$: moderately strong evidence of dependence between the increments
- p-value $\lesssim 0.01$: strong evidence of dependence between the increments.

Please note that these interpretations are based on the assumption that the size of the sample is large. Therefore apart from the p-value itself, the behavior of the p-value when the number of samples or the number of cells change is also important. If the p-value decreases by increasing either the number of samples or the number of cells, then the hypothesis of the increments being independent should be rejected.

For the test to follow we use equally spaced times $t = T/m, 2T/m, \ldots, T$, and we choose the number of cells to be $m = 2^n$ with $n = 5, 7, 10$ and the number of samples $N = k \times 10^4$ with $k = 2, 4, 6, 8$ and 10 to check the trend of the p-value.

5.2.4 Description of the boundary conditions

The simplest form of SLE describes curves defined between two points on the boundary of a domain. In order to test the SLE properties of the domain walls we must conduct our calculations in such a way that the resulting domain walls satisfy this condition. The SLE equations often take their simplest form when this domain is the upper half plane and the curves are defined to run from the origin to infinity. However, due to the invariance of SLE properties under conformal transformations, the equations are exactly known in a number of other domains as well. These are generally domains for which there exists a simple closed form expression for the conformal mapping to the upper half plane. One such domain, and the domain we use, is a square geometry (an $L \times L$ lattice) with the domain wall required to run from the bottom left hand corner (the origin) to the upper right hand corner[5].

This condition on the starting and ending points of the domain wall is fulfilled using two methods. As discussed in section 3.4.2, the domain wall is defined by changes in the ground state spin configurations when the boundary conditions are changed from periodic to anti-periodic. In the first method, in order to satisfy the above condition, we replace all the bonds at the boundaries with very strong ones such that all of the spins at the left and the top edges remain the same in the original and the new ground state spin configurations, while all the spins at

[5] We use this method only for systems with totally-fixed and partially-fixed boundary conditions (described in the next paragraph) because only in these two types of boundaries the domain wall runs through the diagonal.

the bottom and the right edges are flipped. We call this case *totally-fixed boundary conditions*. A similar effect can be achieved by changing only two bonds near the origin and the top right hand corner. The bottom left and the top right couplings are made sufficiently strong such that all of the spins at the left and the top edges remain the same in both periodic and anti-periodic ground state spin configurations, while all the spins along the bottom and right edges are flipped. We refer this one as *partially fixed boundary conditions*.

The above two boundary conditions allow us to compute the SLE properties of the domain wall by using exact calculations. However, the method of imposing the end points by fixing spins may produce domain walls that are not representative of those in the unconstrained system. An alternative method of testing SLE is to produce domain walls in an unbiased way and use an approximate method of comparing to SLE. In this case, we use periodic-free boundary conditions, again in a square domain (an $L \times L$ lattice). Then, instead of comparing to chordal SLE defined in a square domain, we compare to chordal SLE defined in the upper half plane with the origin defined to be the bottom end of the domain wall. Because an $L \times L$ square is not really the upper half plane, this will fail if we look at the whole domain wall, but it is approximately correct in the vicinity of the origin.

5.3 Results

5.3.1 Left passage probability

After finding the domain wall for a given disorder realization, we identify which sites are located on the left or on the right side of the domain wall. For a fixed system of size L, this procedure is repeated for a large number of disorder realizations (Table 5.1), and the results are averaged over the disorders to find the probability $P_L(x,y)$ that a single site is located on the left side of the domain wall. The left passage probability then is obtained from $P^c_{LP}(x,y) = 1 - P_L(x,y)$ and κ is found by minimizing the deviation $E(\kappa)$ according to Eq. (5.2.3). Systems with different boundary conditions with both Gaussian and bimodal couplings are considered and $E(\kappa)$ is calculated. The appropriate value of κ is considered as the value which minimizes the $E(\kappa)$.

5.3.1.1 Totally-fixed boundary conditions

Fig. 5.1 shows the value of $E(k)$ for several values of κ for systems with totally-fixed boundary conditions. Results are reported for Gaussian bond distribution for linear sizes $500 \leq L \leq 3000$ (left panel) as well as for systems with bimodal couplings and linear sizes $200 \leq L \leq 1000$ (right panel). For each disorder realization, shown in Table 5.1, of systems with bimodal bond distribution, we have

Table 5.1: The number of disorder realizations for different boundary conditions, Gaussian (G) or bimodal ($\pm J$), and different system sizes.

L	totally-fixed		partially-fixed		periodic-free	
	G	$\pm J$	G	$\pm J$	G	$\pm J$
100	1×10^5	1×10^5	1×10^5	1×10^5	1×10^5	1×10^5
150	8×10^4	5×10^4	5×10^4	5×10^4	5×10^4	5×10^4
200	1×10^5	1×10^5	5×10^4	1×10^5	1×10^5	1×10^5
350	5×10^4	3×10^4	3×10^4	2×10^4	5×10^4	3×10^4
500	1×10^5	1×10^5	1×10^5	1×10^5	1×10^5	1×10^5
700	4×10^4	1×10^4	2×10^4	1×10^4	3×10^4	2×10^4
1000	2×10^4	5×10^3	1×10^4	5×10^3	2×10^4	1×10^4
1500	7×10^3		5×10^3		1×10^4	
2000	3×10^3		2×10^3		5×10^3	
3000	2×10^3		1×10^3		3×10^3	

generated 10 pairs of ground-state spin configurations using the Gaussian-noise technique (Sec. 4.1) for both periodic and antiperiodic boundaries, determined the domain wall, and averaged over them.

Figure 5.1 shows that the relative minimum of the deviation from the left-passage probability is attained for $\kappa \sim 4.3$ and $\kappa \sim 4.8$ for systems with the Gaussian and bimodal couplings, respectively. According to the SLE relation between κ and the fractal dimension, i.e., $d_\mathrm{f} = 1 + \kappa/8$ [Eq. (2.5.9)], these values of κ hence imply $d_\mathrm{f} \approx 1.54$ for the Gaussian and $d_\mathrm{f} \approx 1.60$ for the bimodal case, which is not compatible with the accurate estimates of d_f reported before. Please note that under the assumption that the domain walls of systems with this boundary conditions could be described by SLE, then the "expected" values of κ according to Eq. (2.5.9) and our precise estimates of the fractal dimension, i.e., $d_\mathrm{f} = 1.273\,19(9)$ for the Gaussian and $d_\mathrm{f} = 1.279(2)$ for bimodal couplings, are $\kappa_\mathrm{G}^\mathrm{expected} \sim 2.2$ and $\kappa_\mathrm{b}^\mathrm{expected} \sim 2.3$ for the Gaussian and bimodal case, respectively. However, the obtained values for κ are much larger than the expected values, and hence it appears clear that the domain walls in this case are not compatible with SLE.

It is necessary to pay attention to the fact that the couplings at the boundaries of the system have been changed in order to force the domain wall to run through the diagonal. This can impact the domain-wall properties, however, it is expected that the effect would vanish far enough away from the boundaries. In order to minimize the impact of the boundaries, the average is taken only over a window of size αL with $0 < \alpha < 1$. The value of $E(\kappa)$ calculated with $\alpha = 0.8$ is shown in Fig. 5.1. Several additional values of α, namely $\alpha = 0.6, 0.4$ and 0.2, were also considered, but the results show that decreasing the value of α only makes the curve of $E(\kappa)$ narrower and does not change the position of its minimum.

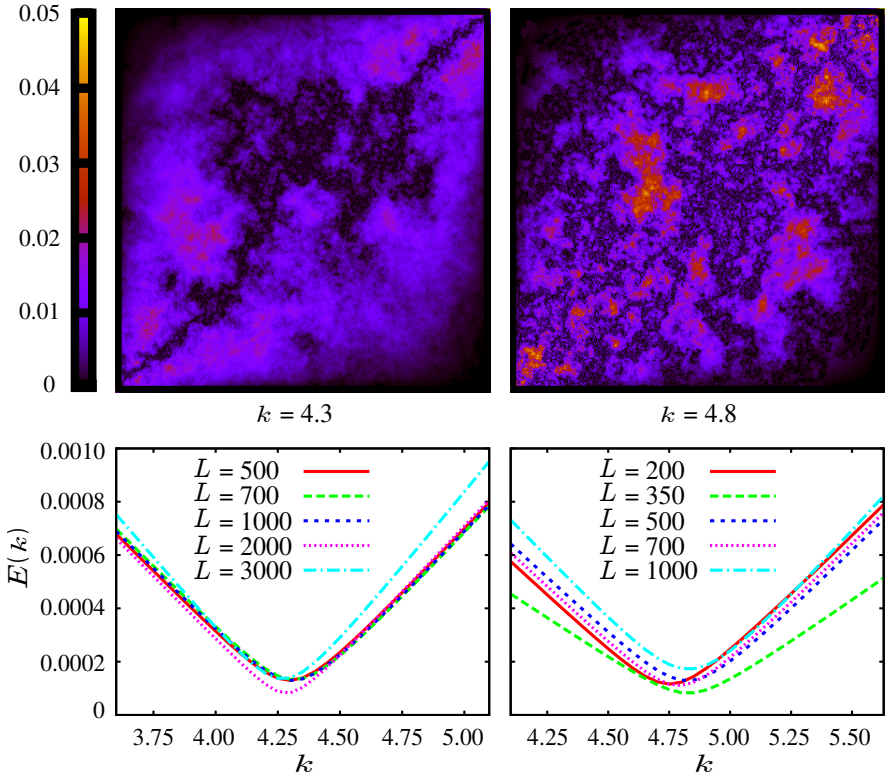

Figure 5.1: The magnitude of deviation of the left passage probability for domain wall from the exact result of Eq. (5.2.2) using totally-fixed boundary conditions. The domain walls are constrained to run between the left bottom corner and the right top corner. The top left panel shows the results for Gaussian couplings with $\kappa = 4.3$ and the top right panel shows the bimodal bond distribution with $\kappa = 4.8$. The lower panel displays the spatially averaged deviation (Eq. (5.2.3)) as a function of the diffusion constant κ, showing a minimum close to $\kappa \sim 4.3$ and $\kappa \sim 4.8$ for Gaussian and bimodal couplings, respectively. The calculations are done over a window of size αL at the center of the system with $\alpha = 0.8$.

5.3.1.2 Partially-fixed boundary conditions

Fig. 5.2 shows the value of $E(k)$ for different values of κ for partially-fixed boundary conditions. The left panel shows systems with Gaussian bond distributions and linear sizes $500 \leq L \leq 3000$, and the right panel has systems with bimodal couplings and linear sizes $200 \leq L \leq 1000$ where for each disorder realization of this case, 10 pairs of ground states for periodic and antiperiodic boundaries were generated by the Gaussian-noise technique (Sec. 4.1). This figure indicates that $E(k)$ reaches its minimum at $\kappa \sim 2.8$ for Gaussian bond distribution and $\kappa \sim 3.6$ for bimodal couplings. The value of $E(\kappa)$ was calculated over a window of size αL with $\alpha = 0.8$. The calculation was repeated for several values of α and we find that although the shape of the figure is narrower for smaller values of α, the position of its minimum remains almost unchanged. The κ values are still bigger than the

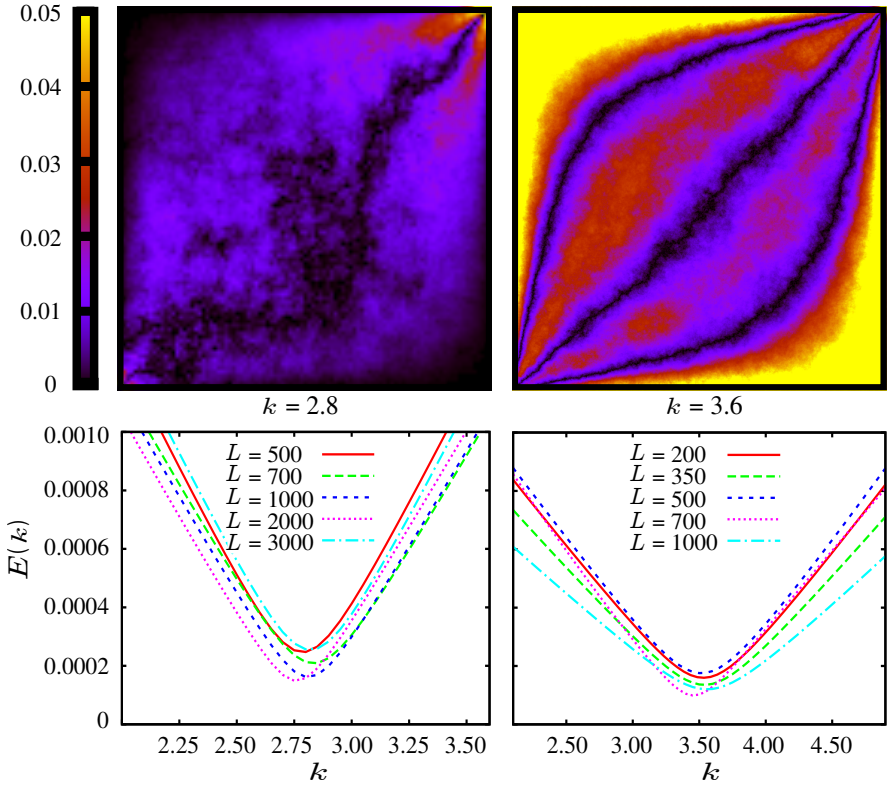

Figure 5.2: The magnitude of deviation of the left passage probability for spin domain wall from the exact result of Eq. (5.2.2) for $\kappa = 2.8$ for Gaussian couplings and $\kappa = 3.6$ for bimodal bond distribution with partially-fixed boundary conditions. The domain walls are constrained to run between the left bottom corner and the right top corner. The lower panel displays the spatially averaged deviation (Eq. (5.2.3)) as a function of the diffusion constant κ, showing a minimum close to $\kappa \sim 2.8$ and $\kappa \sim 3.6$ for Gaussian and bimodal couplings respectively. The calculations are done over a window of size αL at the center of the system with $\alpha = 0.8$.

expected values $\kappa_{\mathrm{G}}^{\mathrm{expected}} \sim 2.2$ for the Gaussian and $\kappa_{\mathrm{b}}^{\mathrm{expected}} \sim 2.3$ for bimodal couplings. However, the deviation from the required κ values is less than that with totally-fixed boundary conditions. This possibly indicates that the impact of fixing the boundaries of the system on the domain wall has been reduced by fixing only two bonds instead of all of the bonds.

5.3.2 Loewner map

The value of κ is also calculated using the Loewner map. For this purpose, the domain wall of the system was calculated and the whole domain mapped to the upper half plane. The vertical slit map introduced in Eq. (5.2.4) was then applied and the one dimensional stochastic process ξ_t is calculated. Each lattice spacing is considered as a segment in the discrete Loewner map. If the domain wall of

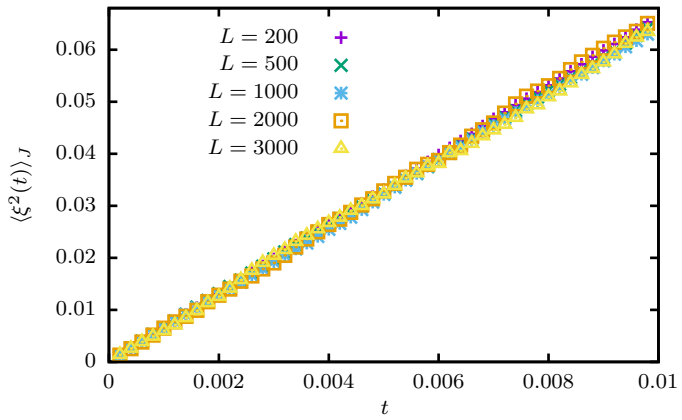

Figure 5.3: $\langle \xi^2(t) \rangle$ vs. Loewner time t for systems with Gaussian couplings and linear size $200 \leq L \leq 3000$ and totally-fixed boundary conditions. The value of κ is estimated as $\kappa \sim 6.6$ for this case.

such a system is an SLE process, then the random process described by ξ_t must be Brownian motion with zero mean and variance κt.

5.3.2.1 Totally-fixed boundary conditions

The average value of $\xi^2(t)$ over disorder realizations (Table 5.1), i.e., $\langle \xi^2(t) \rangle_J$, versus Loewner time for systems with Gaussian couplings and for different values of L is shown in Fig. 5.3. The results show that $\langle \xi^2(t) \rangle_J$ is almost linear in time for times $0 \leq t \leq 0.01$. From the slope of the plot the value of κ was estimated as $\kappa \sim 6.6$. Fig. 5.3 also indicates that the slope is nearly the same for all system sizes. This value for κ is not consistent with the estimate $\kappa \sim 4.3$ obtained from the left passage probability nor with the expected value from the fractal dimension $\kappa_{\mathrm{G}}^{\mathrm{expected}} \sim 2.2$. This is a further evidence that the domain wall for systems with Gaussian couplings and totally-fixed boundary conditions cannot be characterized by SLE.

Fig. 5.4 shows the same quantity as Fig. 5.3 , i.e., $\langle \xi^2(t) \rangle_J$ versus Loewner time, for systems with bimodal bond distribution and linear sizes $200 \leq L \leq 1000$. For the bimodal case we consider both *short* and *long* domain walls, as described in section 4.3.5. The results show that for short domain walls, $\langle \xi^2_{\mathrm{short}}(t) \rangle_J$ is linear in time for $0 \leq t \leq 0.003$, and $\langle \xi^2_{\mathrm{long}}(t) \rangle_J$ is linear in time for $0 \leq t \leq 0.006$. In both cases the linear time range decreases with increasing the lattice sizes. From the slope of these curves the value of κ has been estimated as $\kappa_{\mathrm{s}} \sim 7.2$ and $\kappa_{\mathrm{l}} \sim 7.5$ for short and long domain walls, respectively. Again these estimates do not agree with the κ values from either the left passage probability ($\kappa \sim 4.8$) or the expected value from the fractal dimension ($\kappa_{\mathrm{b}}^{\mathrm{expected}} \sim 2.3$).

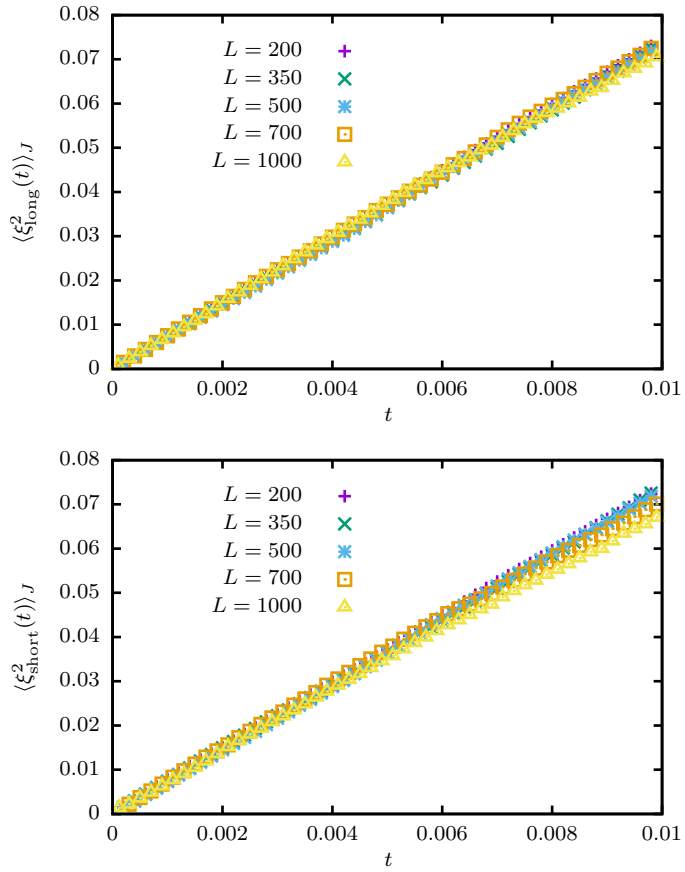

Figure 5.4: $\langle \xi^2(t) \rangle$ vs. Loewner time t for systems with bimodal couplings and linear size $200 \leq L \leq 1000$ and totally-fixed boundary conditions. The value of κ is estimated as $\kappa_{\rm s} \sim 7.2$ and $\kappa_{\rm l} \sim 7.5$ the short and the long domain walls, respectively.

5.3.2.2 Partially-fixed boundary conditions

Fig. 5.5 shows $\langle \xi^2(t) \rangle_J$ versus Loewner time for systems with Gaussian bond distribution and partially-fixed boundary conditions, and indicates that $\langle \xi^2(t) \rangle_J$ is linear for all of the system sizes between $200 \leq L \leq 3000$ up to $t = 0.01$. From the slope we find that $\kappa \sim 2.8$ and it does not vary for different system sizes. In contrast to the case of totally-fixed boundary conditions, this result is in very good agreement with that obtained from the left passage probability. It is, however, still different from the value of κ expected from the fractal dimension ($\kappa_{\rm G}^{\rm expected} \sim 2.2$).

Fig. 5.6 presents $\langle \xi^2(t) \rangle_J$ versus Loewner time for both short and long domain walls of the systems with bimodal couplings and linear sizes $200 \leq L \leq 1000$. The results show that for both cases $\langle \xi^2(t) \rangle$ is linear in time for $0 \leq t \leq 0.01$. Our results indicate that the value of both $\kappa_{\rm s}$ and $\kappa_{\rm l}$ is almost the same, and it is estimated as $\kappa_{\rm s} \simeq \kappa_{\rm l} \sim 3.6$.

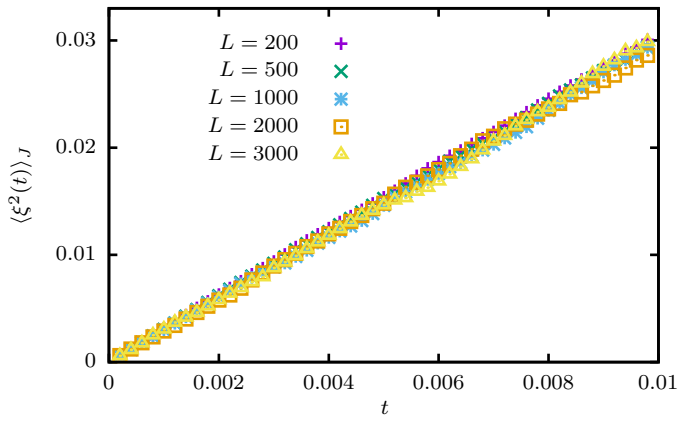

Figure 5.5: $\langle \xi^2(t) \rangle$ vs. Loewner time t for systems with Gaussian couplings and linear size $200 \leq L \leq 3000$ and partially-fixed boundary conditions. The value of κ is estimated as $\kappa \sim 2.8$ for this case.

These values were estimated as $\kappa_s \simeq 7.2$ and $\kappa_l \simeq 7.5$ for systems with totally-fixed boundary conditions. As with the Gaussian couplings, these results are in contrast with the results of totally-fixed boundary conditions, but in rough agreement with the results from the left passage probability (Fig. 5.2). However, they are still different from $\kappa_b^{\text{expected}} \sim 2.3$ determined from the fractal dimension.

5.3.2.3 Periodic-free boundary conditions

So far we have seen that when we fixed the starting point and the endpoint of the domain wall, either with totally-fixed or partially-fixed boundary conditions, the domain wall cannot be characterized by SLE. Here we want to consider unbiased domain walls, i.e., we do not want to force the domain wall to run through the diagonal. For this purpose, we consider systems with periodic-free boundary conditions. Let us consider the periodic boundary to be in the x direction, so the domain wall is free to run between any points of the bottom and the top of the system. In order to compare the domain wall with the SLE on the upper half plane, we need the domain wall to start from the origin. Therefore, once we determined the domain wall, we shift the whole domain wall in such a way that it starts at the bottom left of the system, i.e., the origin. Since the end of the domain wall will not be fixed to be at the upper right corner of the system, it is not correct to consider the whole domain wall and compare it with the SLE on the upper half plane. However if we only consider the beginning of the domain wall, i.e., if we stay in the vicinity of the origin, the comparison is approximately correct.

Fig. 5.7 shows $\langle \xi^2(t) \rangle_J$ for systems with Gaussian couplings and periodic-free boundary conditions as a function of Loewner time for $0 \leq t \leq 0.005$. The beginning of the domain wall, i.e., $t = 0$, is defined to be the origin and $t = 0.005$ roughly corresponds to less than 8 percent of the domain wall length. This ensures that

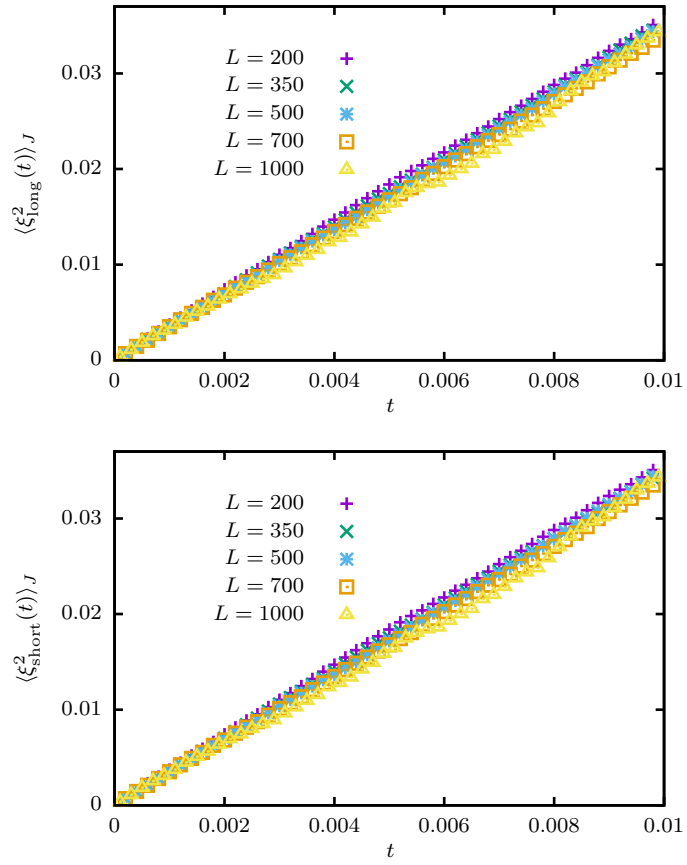

Figure 5.6: $\langle \xi^2(t) \rangle$ vs. Loewner time t for systems with bimodal couplings and linear size $200 \leq L \leq 1000$ and partially-fixed boundary conditions. The estimated value of κ for the short and the long domain domain walls is $\kappa_s \simeq \kappa_l \sim 3.6$.

the calculations were done near the origin. The results show that $\langle \xi^2(t) \rangle_J$ is linear in this range of time, and it has nearly the same slope for all system sizes between $L = 200$ and $L = 3000$. From the slope of the curve the value of κ is estimated as $\kappa \sim 2.2$ which is in a very good agreement with the expected value from the fractal dimension, i.e., $\kappa_G^{\text{expected}} \sim 2.2$. This estimate of κ is also in good agreement with the previous estimates in the literature, for instance $\kappa = 2.1 \pm 0.1$ in Ref. [18] and $\kappa = 2.32 \pm 0.08$ in Ref. [91]. Let us have a closer look at the value of κ for individual system sizes. The value of κ for different system sizes is presented in Fig. 5.8. The results indicate that the estimate of κ for spin glass systems with Gaussian couplings and periodic-free boundary conditions is consistent with the expected value from SLE for the whole range of system sizes.

In Fig. 5.9 we present analogous data for bimodal couplings. The results show that for both short and long domain walls $\langle \xi^2(t) \rangle_J$ is linear in time for the time range $0 \leq t \leq 0.005$. The value of κ for both the short and the long domain walls is then estimated as $\kappa_s \simeq \kappa_l \sim 2.8$. Although we do not force the domain wall to go through the diagonal for this case, however the values of κ_s and κ_l are still too far from the expected value $\kappa_b^{\text{expected}} \sim 2.3$. Therefore our results indicate that

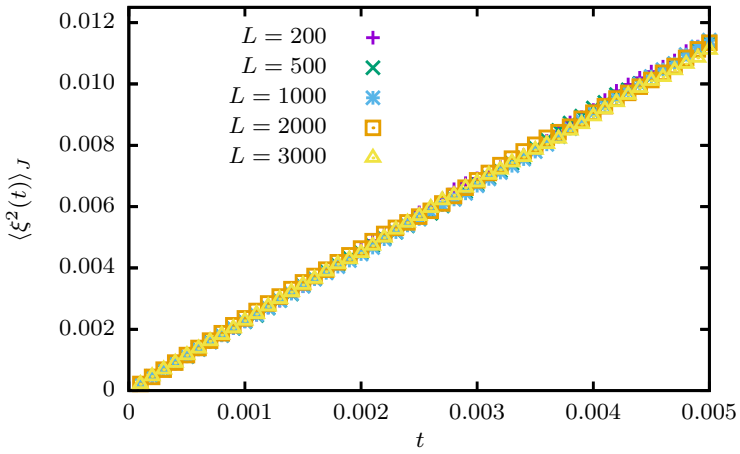

Figure 5.7: $\langle \xi^2(t) \rangle$ vs. Loewner time t for systems with Gaussian couplings and linear size $200 \leq L \leq 3000$ and periodic-free boundary conditions. The value of κ is estimated as $\kappa \sim 2.2$ for this case.

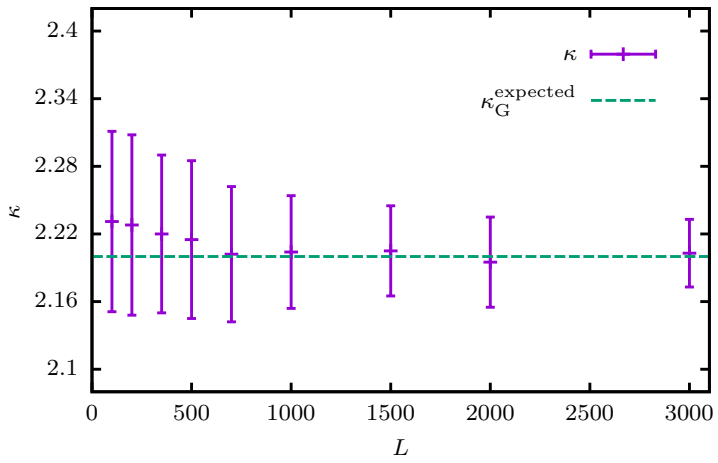

Figure 5.8: The estimated value of κ vs. lattice size for systems with Gaussian couplings and periodic-free boundary conditions. $\kappa_G^{\text{expected}}$ shows the expected value of κ according to Eq. (2.5.9) with $d_f = 1.273\,19(9)$ from our calculation in the chapter 3.

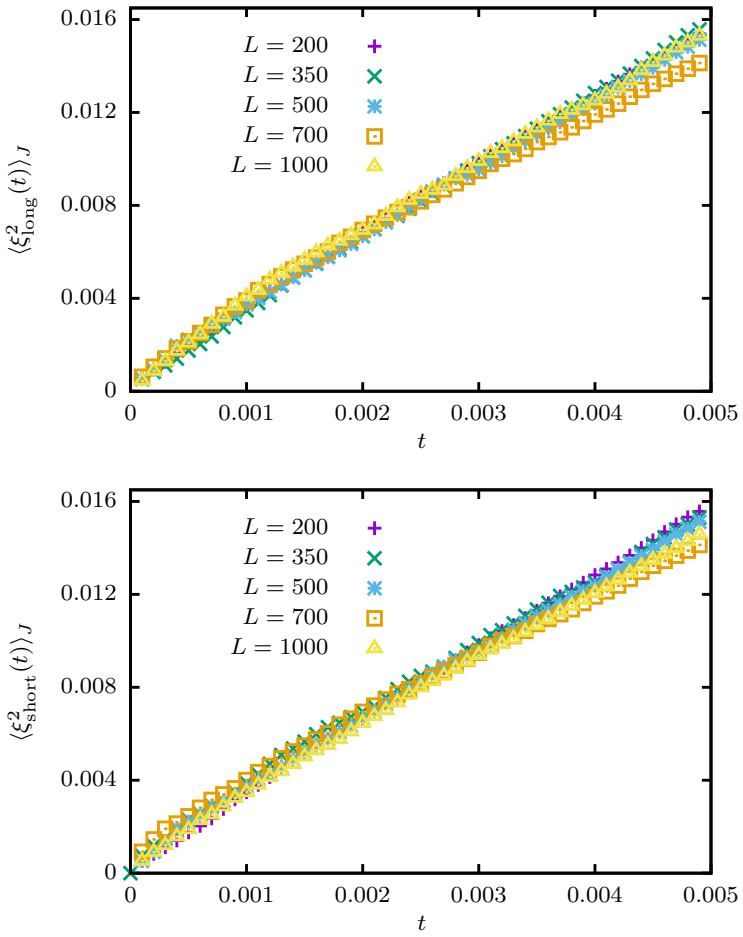

Figure 5.9: $\langle \xi^2(t) \rangle$ vs. Loewner time t for systems with bimodal couplings and linear size $200 \leq L \leq 1000$ and periodic-free boundary conditions. The estimated value of κ for the short and the long domain domain walls is $\kappa_{\rm s} \simeq \kappa_{\rm l} \sim 2.8$.

the domain walls in system with bimodal couplings cannot be characterized by SLE. However, please note that the ground-state spin configurations for bimodal couplings were generated by the Gaussian-noise technique, and hence, we did not have a fair sampling of the ground states. In order to understand whether non-uniform sampling has any effects on this estimate or not, further investigations are needed.

5.3.3 Test of independent increments

In the previous sections we estimated the diffusion constant κ of the underlying Brownian motion of the domain walls. Brownian motion must not have any memory, which means each increment of the driving function must be independent of every other increment. In this section, we want to investigate whether this condition holds for the domain wall of the 2D Ising spin glass when different

boundary conditions are applied by using the test of independent increments described in section 5.2.3.

In order to do that, we consider both Gaussian and bimodal couplings with all the three boundary conditions we have considered before, i.e., totally-fixed, partially-fixed and periodic-free boundary conditions[6]. We calculate the driving function $\xi_i(t)$ for each case. The X_i increments are then determined and only the sign of each increment is taken into account to define the cells (see section 5.2.3). The relative value of the χ^2 test is then computed and the results are presented in terms of the corresponding p-value of each statistics [163]. A p-value gives the probability that a value drawn from the assumed distribution would be at least as extreme as that observed. A small p-value ($\lesssim 0.05$) indicates that the assumption (that the increments are independent) is probably false. The assumption is also false if the p-value tends to zero by increasing the number of realizations N or increasing the system size L.

5.3.3.1 Gaussian couplings

Table 5.2 shows the p-values for the systems with Gaussian couplings and two different boundary conditions: totally-fixed and partially-fixed boundary conditions. The table contains a lot of numbers, but they clearly show the following. For the totally-fixed boundaries the p-values corresponding to $L = 100$ are too small for all values of the number of cells m and the number of realizations N. The situation is more or less the same for $L = 200$, while the p-values for $L = 500$ have larger values, especially for $m = 2^{10}$ cells. However, p-values decrease as the number of realizations increases, and become too small for $N = 80000$ and $N = 100\,000$. The p-values of systems with partially-fixed boundary conditions are simply too small everywhere. We, therefore, reject the hypothesis that $\xi_i(t)$ is a Brownian motion for both of them. The resulting p-values for systems with periodic-free boundary conditions, however, show that the hypothesis that $\xi_i(t)$ is a Brownian motion cannot be rejected (Table 5.3), because they have relatively large values almost everywhere, especially for the largest system size ($L = 500$).
Therefore we conclude that the domain walls of systems with Gaussian couplings and both totally-fixed and partially-fixed boundary conditions are not SLE processes, while the domain wall of systems with periodic-free boundary conditions can be described by chordal SLE. In this sense, the results based on the test of independent increments are in agreement with the previous results obtained from the left passage probability and the Loewner map.

[6] Again, 10 pairs of ground-state spin configurations for each realization of bimodal couplings were generated using the Gaussian-noise technique.

Table 5.2: p-values for systems with Gaussian bond distribution and both totally-fixed and partially-fixed boundary conditions. The number of cells is $m = 2^n$, and N represents the number of realizations.

n	N	totally-fixed			partially-fixed		
		$L = 100$	$L = 200$	$L = 500$	$L = 100$	$L = 200$	$L = 500$
$n = 5$	20000	0.000015	0.200460	0.021396	0.000000	0.000000	0.000000
	40000	0.000000	0.000209	0.000040	0.000000	0.000000	0.000000
	60000	0.000000	0.000000	0.000000	0.000000	0.000000	0.000000
	80000	0.000000	0.000000	0.000000	0.000000	0.000000	0.000000
	100000	0.000000	0.000000	0.000000	0.000000	0.000000	0.000000
$n = 7$	20000	0.000010	0.000737	0.110223	0.000000	0.000000	0.000000
	40000	0.000000	0.000004	0.027159	0.000000	0.000000	0.000000
	60000	0.000000	0.000000	0.000158	0.000000	0.000000	0.000000
	80000	0.000000	0.000000	0.000001	0.000000	0.000000	0.000000
	100000	0.000000	0.000000	0.000000	0.000000	0.000000	0.000000
$n = 10$	20000	0.000343	0.125719	0.907915	0.000000	0.000002	0.000000
	40000	0.000000	0.000000	0.351905	0.000000	0.000000	0.000000
	60000	0.000000	0.000000	0.146010	0.000000	0.000000	0.000000
	80000	0.000000	0.000000	0.007570	0.000000	0.000000	0.000000
	100000	0.000000	0.000000	0.001444	0.000000	0.000000	0.000000

Table 5.3: p-values for systems with Gaussian bond distribution and periodic-free boundary conditions. The number of cells is $m = 2^n$, and N represents the number of realizations.

n	N	periodic-free		
		$L = 100$	$L = 200$	$L = 500$
$n = 5$	20000	0.184371	0.292873	0.421404
	40000	0.643369	0.178140	0.589917
	60000	0.796821	0.258908	0.711042
	80000	0.512961	0.319063	0.530684
	100000	0.058417	0.218448	0.802898
$n = 7$	20000	0.431683	0.648731	0.075871
	40000	0.370006	0.187306	0.264601
	60000	0.372715	0.196407	0.387504
	80000	0.211085	0.021160	0.413074
	100000	0.012888	0.025379	0.586806
$n = 10$	20000	0.284363	0.898157	0.159843
	40000	0.282449	0.694483	0.153048
	60000	0.420596	0.316162	0.780828
	80000	0.160943	0.037184	0.923543
	100000	0.076669	0.012304	0.870001

5.3.3.2 Bimodal couplings

The data for the short domain walls as well as the long domain walls for systems with bimodal couplings and totally-fixed and partially-fixed boundary conditions are shown in Tables 5.4 and 5.5, respectively. The results clearly show that the hypothesis that the driving function of these domain walls is a Brownian motion is rejected.

The corresponding data for systems with periodic-free boundary conditions is shown in Table 5.6. The results indicate that the p-value is large enough for small systems and small number of realizations, especially for long domain walls. However by increasing the number of realization the p-value decreases almost monotonically. We, therefore, reject the hypothesis that $\xi_i(t)$ is a Brownian motion for both of them in this case.

The fact that the test of independent increments shows some sort of correlations between the segments of this type of domain walls for bimodal couplings, although the domain walls were not forced to run through the diagonal and were actually free to move, might be a consequence of the fact that the ground states were not generated by an unbiased algorithm. Therefore it might not be surprising if the test shows that there is a dependency between the increments. However it is not clear how this dependency would change if ground states are generated uniformly. Hence, the question of possibility of characterizing domain walls of the two-dimensional $\pm J$ Ising spin glass with open periodic boundary conditions by SLE remains still open.

5.4 Summary and conclusion

In this chapter, we investigated the possibility of characterizing the domain walls of the two-dimensional Ising spin glass by SLE, and we wanted to find out whether changing the boundary conditions of the system may change the SLE properties or not. Therefore, three different boundary conditions as totally fixed, partially fixed and periodic-free boundary conditions were considered. Two different tests, the left passage probability and the Loewner map, based on the SLE relation between κ and d_f, i.e., $d_f = 1 + \kappa/8$ have been considered. In addition, the Markov property of the domain walls was also checked using the test of independent increments. The results show that if we force the domain wall of the system to run through the diagonal, the hypothesis of describing the domain wall by SLE will be rejected. On the other hand, if we consider periodic-free boundary conditions and leave the domain wall to be free, then results clearly show that the domain wall for systems with Gaussian bond distribution can be characterized by SLE_κ with $\kappa \sim 2.2$. This estimate of κ is in good agreement with previous estimates of Refs. [18, 91]. The

Table 5.4: p-values of the short domain walls for systems with bimodal bond distribution and both totally-fixed and partially-fixed boundary conditions. The number of cells is $m = 2^n$, and N represents the number of realizations.

n	N	totally-fixed			partially-fixed		
		$L = 100$	$L = 200$	$L = 500$	$L = 100$	$L = 200$	$L = 500$
$n = 5$	20000	0.001182	0.000000	0.000000	0.000000	0.000000	0.000001
	40000	0.000005	0.000000	0.000000	0.000000	0.000000	0.000000
	60000	0.000000	0.000000	0.000000	0.000000	0.000000	0.000001
	80000	0.000000	0.000000	0.000000	0.000000	0.000000	0.000000
	100000	0.000000	0.000000	0.000000	0.000000	0.000000	0.000000
$n = 7$	20000	0.001104	0.000015	0.000008	0.000007	0.000019	0.000000
	40000	0.000055	0.000017	0.000430	0.000060	0.000011	0.000431
	60000	0.000016	0.000010	0.000000	0.000017	0.000016	0.000000
	80000	0.000002	0.000009	0.000021	0.000003	0.000003	0.000000
	100000	0.000000	0.000000	0.000000	0.000000	0.000000	0.000000
$n = 10$	20000	0.004011	0.000000	0.104602	0.000084	0.000000	0.000621
	40000	0.000129	0.000000	0.000423	0.000000	0.000000	0.000020
	60000	0.000013	0.000000	0.000013	0.000006	0.000000	0.000017
	80000	0.000001	0.000000	0.000019	0.000000	0.000000	0.000001
	100000	0.000000	0.000000	0.000003	0.000000	0.000000	0.000000

Table 5.5: p-values of the long domain walls for systems with bimodal bond distribution and both totally-fixed and partially-fixed boundary conditions. The number of cells is $m = 2^n$, and N represents the number of realizations.

n	N	totally-fixed			partially-fixed		
		$L = 100$	$L = 200$	$L = 500$	$L = 100$	$L = 200$	$L = 500$
$n = 5$	20000	0.001770	0.000000	0.000040	0.000000	0.000001	0.000042
	40000	0.000000	0.000000	0.000001	0.000000	0.000000	0.000005
	60000	0.000003	0.000000	0.000000	0.000000	0.000008	0.000000
	80000	0.000000	0.000000	0.000000	0.000000	0.000000	0.000000
	100000	0.000000	0.000000	0.000000	0.000000	0.000000	0.000000
$n = 7$	20000	0.008454	0.000070	0.000035	0.000611	0.000079	0.000230
	40000	0.000127	0.000000	0.000174	0.000000	0.000000	0.000000
	60000	0.000038	0.000002	0.000009	0.000000	0.000019	0.000000
	80000	0.000001	0.000000	0.000009	0.000000	0.000146	0.000000
	100000	0.000000	0.000000	0.000000	0.000000	0.000000	0.000034
$n = 10$	20000	0.002191	0.002354	0.000197	0.000236	0.000354	0.000425
	40000	0.000089	0.000110	0.000093	0.000100	0.000012	0.000699
	60000	0.000043	0.002902	0.000000	0.000015	0.000987	0.000101
	80000	0.000000	0.000005	0.000008	0.000023	0.000008	0.000001
	100000	0.000001	0.000006	0.000000	0.000009	0.000009	0.000001

Table 5.6: *p*-values of the short and the long domain walls for systems with bimodal bond distribution and periodic-free boundary conditions. The number of cells is $m = 2^n$, and N represents the number of realizations.

n	N	short domain walls			long domain walls		
		$L = 100$	$L = 200$	$L = 500$	$L = 100$	$L = 200$	$L = 500$
$n = 5$	20000	0.424005	0.228394	0.286541	0.451371	0.151334	0.110691
	40000	0.228210	0.042883	0.036227	0.200810	0.116894	0.001687
	60000	0.069371	0.000745	0.003364	0.042156	0.065703	0.020076
	80000	0.009747	0.000741	0.000204	0.007963	0.035550	0.009661
	100000	0.000644	0.000092	0.000239	0.000438	0.047064	0.017260
$n = 7$	20000	0.002097	0.604357	0.018851	0.002594	0.981155	0.537001
	40000	0.005731	0.306794	0.189576	0.007572	0.196186	0.343064
	60000	0.000410	0.028716	0.079984	0.000601	0.422864	0.028263
	80000	0.000018	0.006666	0.010740	0.000017	0.055700	0.011770
	100000	0.000000	0.000014	0.011607	0.000003	0.008824	0.003557
$n = 10$	20000	0.020893	0.323344	0.106475	0.046666	0.882380	0.685051
	40000	0.000070	0.177650	0.124357	0.000234	0.288142	0.305543
	60000	0.000001	0.041131	0.014675	0.000009	0.340613	0.024407
	80000	0.000000	0.000222	0.002954	0.000000	0.109041	0.014435
	100000	0.000003	0.000106	0.000078	0.000001	0.033620	0.010861

results for systems with periodic-free boundary conditions and bimodal couplings, however, are not compatible with SLE. This might be due to the fact that the ground-state spin configurations for these systems were not generated according to a fair sampling. Hence there could be a correlation between the considered ground-state configurations, and this can affect the Markov property, and in general, the SLE property of the domain walls.

Chapter 6

Conclusions and outlook

This thesis was devoted to a study of the two-dimensional Ising spin glass at zero temperature. The rich physics, the unique features, and the numerical tractability of the 2D models compared to higher-dimensional systems are some reasons which make this system very interesting to study.

We started by a general introduction to spin-glass systems in Chapter 1. The Edwards-Anderson model as well as some key concepts of statistical mechanics, phase transitions and finite-size scaling techniques were recalled. We then discussed the most famous pictures for spin glasses, i.e., the *replica symmetry breaking picture* [58] and the *droplet picture* [10], and we described some physical aspects of these two scenarios. The stiffness exponent θ, defect energy, domain walls and the fractal dimension d_f of the domain walls were also introduced in Chapter 1, and we have seen that the spin-glass phase transition in two dimensions occurs at zero temperature. Therefore in order to study the spin-glass phase for 2D systems, ground-state calculations are suitable.

Since the domain walls of spin-glass systems look like random curves (see Fig. 3.8 as an example), in Chapter 2 we introduced a powerful mathematical tool for studying random curves in 2D known as *Schramm-Loewner evolution* (SLE) [93]. The precise definition of SLE as well as the postulates of SLE were discussed in this chapter. If a random curve in 2D can be described by SLE then the curve can be characterized by only one parameter, κ, which is the diffusion constant of the relative Brownian motion driving the SLE. Ref. [90] suggested that if the domain walls of the 2D Ising spin glasses can be described by SLE (and some further assumptions hold) then the following relation between stiffness exponent and fractal dimension should hold:

$$d_f = 1 + \frac{3}{4(3+\theta)}.$$

Calculating accurate estimates of d_f and θ, and investigating the validity of this conjecture was one of the goals of this thesis.

In Chapter 3 we introduced a recently proposed and efficient algorithm to calculate ground states of 2D spin glasses. This method is based on the minimum-weight perfect matching problem and it is able to determine the ground states in polynomial time as long as periodic boundary conditions are applied in at most one direction. Since the finite-size corrections are expected to be smaller for systems with fully periodic boundary conditions and the matching algorithm does not work for these systems, we then developed a new algorithm to treat such systems. Our approach is based on the combination of the matching algorithm and a windowing technique, and it enables us to determine quasi-exact ground states for systems with periodic-periodic boundary conditions in a polynomial time. The run-time of this method is increased over that of the original matching algorithm by a constant factor only. Since the ground states of systems with bimodal couplings are highly degenerate and thus extra calculations are needed to study these systems, in Chapter 3 we first focused on systems with a Gaussian bond distribution (where one has a unique ground state), and studied systems with $\pm J$ couplings in Chapter 4. By using the matching technique and our new algorithm we determined exact ground states for systems with Gaussian couplings and periodic-free boundary conditions (PFBC) for lattices of linear size up to $L = 10\,000$, and quasi-exact ground states of systems with periodic-periodic boundary conditions (PPBC) up to $L = 3000$. We then calculated the defect energies as well as the domain walls of these systems and arrived at $\theta = -0.2793(3)$ and $d_f = 1.273\,19(9)$ for PFBC obtained by the exact algorithm based on the matching method, and $\theta = -0.2778(11)$ and $d_f = 1.2732(5)$ for PPBC obtained by the windowing technique. These estimates are in agreement with each other indicating the correctness of the windowing technique for the PPBC case. These are the most accurate estimates of the stiffness exponent and the fractal dimension which have been reported to date. Our values are fully consistent with previous estimates of θ and d_f in the literature shown in Table 3.5, but 10 to 100 times more accurate. At the end, we checked the consistency of the SLE conjecture $d_f = 1 + 3/4(3 + \theta)$ with our estimates, and we concluded that our data do not appear to be consistent with this relation.

The two-dimensional Ising spin glass with discrete coupling distribution is considered in Chapter 4. It is known that this system has an extensive ground-state degeneracy, and the number of degenerate ground states grows exponentially with system size [83, 84, 148]. Therefore an exact enumeration is not practical, except for very small systems. It is hence necessary to develop techniques for sampling the ground-state manifold uniformly. While the matching based algorithms can be modified to generate random ground states in the presence of degeneracies,

they are not in general produced with uniform probabilities. In Chapter 4 we presented a new efficient algorithm to sample degenerate ground states of the two-dimensional $\pm J$ Ising spin glass uniformly. Our algorithm is based on a determination of the exact cluster configuration of the system by using the matching technique, and a subsequent parallel tempering Monte Carlo simulation to generate and sample the ground states uniformly. The algorithm enables us to calculate all of the ground states for systems with $L \lesssim 20$, and sample exact ground states for systems up to size $L = 128$ uniformly. By using the matching technique and our new sampling algorithm we studied the ground-state energy and domain wall properties of this system. Our results showed that the defect energy for this system has an asymptotic value of $e_\infty = -1.401\,922(3)$ indicating that the stiffness exponent vanishes for this model, i.e., $\theta = 0$. For the fractal dimension of the model with $\pm J$ couplings we considered two cases. In the first one, no bubbles (clusters of free spins) are attached to the domain wall and we called this case *the short domain wall*. In the other case, all such bubbles were considered as parts of the domain wall and we referred to this case as *the long domain wall*. We then obtained $d_\mathrm{f} = 1.279(2)$ for the short domain walls and $d_\mathrm{f} = 1.281(3)$ for the long domain walls. The results for the short and the long domain walls are hence consistent with each other, while they are marginally consistent with those for the Gaussian model. It hence remains an interesting question for further studies whether universality between the two models holds in this respect.

In Chapter 5 we focused on the domain walls of the 2D Ising spin glass and investigated some more of their properties. In particular, we asked whether the domain walls of this system are consistent with Schramm-Loewner evolution implying that they are also conformally invariant. One of the checks was to see whether the SLE relation between the fractal dimension d_f and the diffusion constant κ, i.e., $d_\mathrm{f} = 1 + \frac{\kappa}{8}$ [Eq. (2.5.9)] is fulfilled. We considered three different boundary conditions namely *totally-fixed*, *partially-fixed* and *periodic-free* boundaries. For the first two boundary conditions we forced the domain walls to run through the diagonal and estimated the value of κ by calculating the left passage probability. For periodic-free boundary conditions the domain wall is free to move. We then used the Loewner map to estimate κ for the three different setups. The results for both Gaussian and bimodal couplings showed that the forced domain walls are not consistent with SLE. For the case of free domain walls, only systems with a Gaussian bond distribution were consistent with SLE. After that, the correlations between different domain-wall segments were explicitly checked by testing for independence of the increments of the Loewner driving function. The test showed that segments of the forced domain walls are not independent, and segments of the free domain walls are independent only for systems with Gaussian couplings. The dependency between segments of the free domain walls in the bimodal case

might be a consequence of not choosing the ground states uniformly. Therefore it remains as a question for future work to see what happens if the ground states of systems with bimodal couplings are chosen uniformly.

Bibliography

[1] N. Kawashima and H. Rieger. *Recent progress in spin glasses*. World Scientific, Singapore, 2005.

[2] Marco Baity Jesi. *Spin Glasses Criticality and Energy Landscapes*. Springer Nature, Switzerland, 2016.

[3] K. Binder and A. P. Young. Spin glasses: Experimental facts, theoretical concepts, and open questions. *Rev. Mod. Phys.*, 58:801, 1986.

[4] H. Nishimori. *Statistical Physics of Spin Glasses and Information Processing*. Oxford University Press, Oxford, 2001.

[5] P. W. Anderson. Localisation theory and the Cu-Mn problem: Spin glasses. *Materials Research Bulletin*, 5(8):549 – 554, 1970.

[6] S. F. Edwards and P. W. Anderson. Theory of spin glasses. *Journal of Physics F: Metal Physics*, 5(5):965, 1975.

[7] A. J. Bray and M. A. Moore. Lower critical dimension of Ising spin glasses: a numerical study. *J. Phys. C: Solid State Phys.*, 17:463, 1984.

[8] Andrew T. Ogielski. Dynamics of three-dimensional Ising spin glasses in thermal equilibrium. *Phys. Rev. B*, 32:7384–7398, 1985.

[9] E Marinari, G Parisi, and F Ritort. On the 3D Ising spin glass. *Journal of Physics A: Mathematical and General*, 27(8):2687, 1994.

[10] D. S. Fisher and D. A. Huse. Equilibrium behavior of the spin-glass ordered phase. *Physical Review B*, 38(1):386, 1988.

[11] M. Palassini and S. Caracciolo. Finite size scaling in 3D Ising spin glasses. *Computer Physics Communications*, 121(Supplement C):180 – 182, 1999. Proceedings of the Europhysics Conference on Computational Physics CCP 1998.

[12] H. G. Ballesteros, A. Cruz, L. A. Fernández, V. Martín-Mayor, J. Pech, J. J. Ruiz-Lorenzo, A. Tarancón, P. Téllez, C. L. Ullod, and C. Ungil. Critical

behavior of the three-dimensional Ising spin glass. *Phys. Rev. B*, 62:14237–14245, 2000.

[13] A. K. Hartmann. A new method for analysing ground-state landscapes : ballistic search. *IOP J. Phys. A Gen.*, 33:657–674, 2000.

[14] Helmut G. Katzgraber, Matteo Palassini, and A. P. Young. Monte Carlo simulations of spin glasses at low temperatures. *Phys. Rev. B*, 63:184422, 2001.

[15] J. Landry and S. Coppersmith. Ground states of two-dimensional $\pm J$ Edwards-Anderson spin glasses. *Physical Review B*, 65(13):134404, 2002.

[16] I. A. Campbell, A. K. Hartmann, and H. G. Katzgraber. Energy size effects of two-dimensional Ising spin glasses. *Physical Review B*, 054429:1–10, 2004.

[17] Helmut G. Katzgraber, Mathias Körner, and A. P. Young. Universality in three-dimensional Ising spin glasses: A Monte Carlo study. *Phys. Rev. B*, 73:224432, 2006.

[18] C. Amoruso, A. Hartmann, M. Hastings, and M. Moore. Conformal Invariance and Stochastic Loewner Evolution Processes in Two-Dimensional Ising Spin Glasses. *Physical Review Letters*, 97(26):267202, 2006.

[19] Pierluigi Contucci, Cristian Giardinà, Claudio Giberti, Giorgio Parisi, and Cecilia Vernia. Ultrametricity in the edwards-anderson model. *Phys. Rev. Lett.*, 99:057206, 2007.

[20] O. Melchert and A. K. Hartmann. Fractal dimension of domain walls in two-dimensional Ising spin glasses. *Phys. Rev. B*, 76:174411, 2007.

[21] G. Pardella and F. Liers. Exact ground states of large two-dimensional planar Ising spin glasses. *Phys. Rev. E*, 78:056705, 2008.

[22] M. Hasenbusch, A. Pelissetto, and E. Vicari. The critical behavior of 3D Ising spin glass models: universality and scaling corrections. *Journal of Statistical Mechanics: Theory and Experiment*, 2008(02):L02001, 2008.

[23] F. Belletti *et. all* . An In-Depth View of the Microscopic Dynamics of Ising Spin Glasses at Fixed Temperature. *Journal of Statistical Physics*, 135(5):1121–1158, 2009.

[24] Alvarez Baños *et. all* . Static versus Dynamic Heterogeneities in the $D = 3$ Edwards-Anderson Ising Spin Glass. *Phys. Rev. Lett.*, 105:177202, 2010.

[25] F. Romá, S. Risau-Gusman, A. J. Ramirez-Pastor, F. Nieto, and E. E. Vogel. Ground-state topology of the Edwards-Anderson $\pm J$ spin glass model. *Phys. Rev. B*, 82:214401, 2010.

[26] J. M. Kosterlitz. The critical properties of the two-dimensional *XY* model. *Journal of Physics C: Solid State Physics*, 7(6):1046, 1974.

[27] S. Teitel and C. Jayaprakash. Phase transtions in frustrated two-dimensional *XY* models. *Phys. Rev. B*, 27:598–601, 1983.

[28] J. Maucourt and D. R. Grempel. Lower critical dimension of the *XY* spin-glass model. *Phys. Rev. Lett.*, 80:770–773, 1998.

[29] J. A. Olive, A. P. Young, and D. Sherrington. Computer simulation of the three-dimensional short-range Heisenberg spin glass. *Phys. Rev. B*, 34:6341–6346, 1986.

[30] A. J. Bray and M. A. Moore. Heisenberg-Ising crossover in spin glasses. *Phys. Rev. B*, 34:6561–6563, 1986.

[31] I. Campos, M. Cotallo-Aban, V. Martín-Mayor, S. Perez-Gaviro, and A. Tarancon. Spin-Glass Transition of the three-dimensional Heisenberg Spin Glass. *Phys. Rev. Lett.*, 97:217204, 2006.

[32] L. W. Lee and A. P. Young. Large-scale Monte Carlo simulations of the isotropic three-dimensional Heisenberg spin glass. *Phys. Rev. B*, 76:024405, 2007.

[33] D. X. Viet and H. Kawamura. Numerical Evidence of Spin-Chirality Decoupling in the Three-Dimensional Heisenberg Spin Glass Model. *Phys. Rev. Lett.*, 102:027202, 2009.

[34] D. Sherrington and S. Kirkpatrick. Solvable model of a spin-glass. *Phys. Rev. Lett.*, 35:1792–1796, 1975.

[35] S. Kirkpatrick and D. Sherrington. Infinite-ranged models of spin-glasses. *Phys. Rev. B*, 17:4384–4403, 1978.

[36] Giorgio Parisi. Mean field theory of spin glasses: Statics and dynamics. In Jean-Philippe Bouchaud, Marc Mézard, and Jean Dalibard, editors, *Complex Systems*, volume 85 of *Les Houches*, pages 131–178. Elsevier, 2007.

[37] A. P. Young. *Numerical studies of spin glasses*, pages 328–345. Springer Berlin Heidelberg, 1983.

[38] P. Pfeuty and G. Toulouse. *Introduction to the Renormalization Group and to Critical Phenomena*. John Wiley and Sons Ltd., London . New York . Sydney . Toronto, 1977.

[39] A. Pelissetto and E. Vicari. Critical phenomena and renormalization-group theory. *Physics Reports*, 368(6):549 – 727, 2002.

[40] N. Goldenfeld. *Lectures on Phase Transitions and The Renormalization Group*. Perseus Books Publishing, L.L.C., Reading, Massachusetts, 1992.

[41] Michael E. Fisher and Michael N. Barber. Scaling theory for finite-size effects in the critical region. *Phys. Rev. Lett.*, 28:1516–1519, 1972.

[42] K. Binder. Finite size scaling analysis of Ising model block distribution functions. *Zeitschrift für Physik B Condensed Matter*, 43(2):119–140, 1981.

[43] K. Binder. Monte Carlo calculation of the surface tension for two- and three-dimensional lattice-gas models. *Phys. Rev. A*, 25:1699–1709, 1982.

[44] H.G. Ballesteros, L.A. Fernández, V. Martín-Mayor, and A. Munoz Sudupe. Finite size effects on measures of critical exponents in $d = 3$ $O(N)$ models. *Physics Letters B*, 387(1):125 – 131, 1996.

[45] L. W. Lee and A. P. Young. Single spin and chiral glass transition in vector spin glasses in three dimensions. *Phys. Rev. Lett.*, 90:227203, 2003.

[46] T. Jörg. Critical behavior of the three-dimensional bond-diluted Ising spin glass: Finite-size scaling functions and universality. *Phys. Rev. B*, 73:224431, 2006.

[47] L. Leuzzi, G. Parisi, F. Ricci-Tersenghi, and J. J. Ruiz-Lorenzo. Dilute one-dimensional spin glasses with power law decaying interactions. *Phys. Rev. Lett.*, 101:107203, 2008.

[48] T. Jörg, H. G. Katzgraber, and F. Krząkała. Behavior of Ising Spin Glasses in a Magnetic Field. *Phys. Rev. Lett.*, 100:197202, 2008.

[49] L. A. Fernandez, V. Martín-Mayor, and D. Yllanes. Tethered Monte Carlo: Computing the effective potential without critical slowing down. *Nuclear Physics B*, 807(3):424 – 454, 2009.

[50] R. A. Baños, L. A. Fernandez, V. Martín-Mayor, and A. P. Young. Correspondence between long-range and short-range spin glasses. *Phys. Rev. B*, 86:134416, 2012.

[51] M. Baity-Jesi, L. A. Fernández, V. Martín-Mayor, and J. M. Sanz. Phase transition in three-dimensional Heisenberg spin glasses with strong random anisotropies through a multi-GPU parallelization. *Phys. Rev. B*, 89:014202, 2014.

[52] Matteo Lulli, Giorgio Parisi, and Andrea Pelissetto. Out-of-equilibrium finite-size method for critical behavior analyses. *Phys. Rev. E*, 93:032126, 2016.

[53] Hamid Khoshbakht and Martin Weigel. Domain-wall excitations in the two-dimensional Ising spin glass. *Phys. Rev. B*, 97:064410, 2018.

[54] Enzo Marinari, Giorgio Parisi, Federico Ricci-Tersenghi, Juan J. Ruiz-Lorenzo, and Francesco Zuliani. Replica symmetry breaking in short-range spin glasses: Theoretical foundations and numerical evidences. *Journal of Statistical Physics*, 98(5):973–1074, 2000.

[55] C. M. Newman and D. L. Stein. Ordering and broken symmetry in short-ranged spin glasses. *Journal of Physics: Condensed Matter*, 15(32):R1319, 2003.

[56] M. Mézard, G. Parisi, and M. Virasoro. *Spin Glass Theory and Beyond*. World Scientific, 1986.

[57] Tommaso Castellani and Andrea Cavagna. Spin-glass theory for pedestrians. *Journal of Statistical Mechanics: Theory and Experiment*, 2005(05):P05012, 2005.

[58] G. Parisi. Infinite number of order parameters for spin-glasses. *Phys. Rev. Lett.*, 43:1754–1756, 1979.

[59] E Orlandini, M C Tesi, and S G Whittington. Self-averaging in the statistical mechanics of some lattice models. *Journal of Physics A: Mathematical and General*, 35(19):4219, 2002.

[60] Georgio Parisi. The physical meaning of replica symmetry breaking. *arXiv:cond-mat/0205387 [cond-mat.stat-mech]*, 2002.

[61] M. Mézard, G. Parisi, N. Sourlas, G. Toulouse, and M. Virasoro. Nature of the spin-glass phase. *Phys. Rev. Lett.*, 52:1156–1159, 1984.

[62] Jayanth R. Banavar and Marek Cieplak. Nature of ordering in spin-glasses. *Phys. Rev. Lett.*, 48:832–835, Mar 1982.

[63] A. J. Bray and M. A. Moore. Scaling theory of the ordered phase of spin glasses. In J. L. van Hemmen and I. Morgenstern, editors, *Heidelberg Colloquium on Glassy Dynamics*, page 121, Heidelberg, 1987. Springer.

[64] A. K. Hartmann and A. P. Young. Large-scale low-energy excitations in the two-dimensional Ising spin glass. *Phys. Rev. B*, 66:094419, 2002.

[65] A. K. Hartmann. Droplets in the two-dimensional $\pm J$ Ising spin glass. *Phys. Rev. B*, 77:144418, 2008.

[66] Matthew Wittmann, B. Yucesoy, Helmut G. Katzgraber, J. Machta, and A. P. Young. Low-temperature behavior of the statistics of the overlap distribution in Ising spin-glass models. *Phys. Rev. B*, 90:134419, 2014.

[67] Daniel S. Fisher and David A. Huse. Ordered Phase of Short-Range Ising Spin-Glasses. *Phys. Rev. Lett.*, 56:1601–1604, 1986.

[68] F. Krzakala and O. C. Martin. Spin and Link Overlaps in Three-Dimensional Spin Glasses. *Phys. Rev. Lett.*, 85:3013, 2000.

[69] F. Krzakala and O. C. Martin. Discrete energy landscapes and replica symmetry breaking at zero temperature. *EPL (Europhysics Letters)*, 53(6):749, 2001.

[70] Matteo Palassini and A. P. Young. Effects of ground-state degeneracy on the $\pm J$ spin glass. *Phys. Rev. B*, 63:140408, 2001.

[71] Alexander K. Hartmann and Federico Ricci-Tersenghi. Direct sampling of complex landscapes at low temperatures: The three-dimensional $\pm J$ Ising spin glass. *Phys. Rev. B*, 66:224419, 2002.

[72] Wolfhard Janke. *Rugged Free Energy Landscapes: Common Computational Approaches to Spin Glasses, Structural Glasses and Biological Macromolecules*. Springer-Verlag Berlin Heidelberg, 2008.

[73] F. Parisen Toldin, A. Pelissetto, and E. Vicari. Strong-disorder paramagnetic-ferromagnetic fixed point in the square-lattice $\pm J$ Ising model. *J. Stat. Phys.*, 135:1039, 2009.

[74] Creighton K. Thomas and Helmut G. Katzgraber. Simplest model to study reentrance in physical systems. *Phys. Rev. E*, 84:040101, 2011.

[75] A. K. Hartmann and A. P. Young. Lower critical dimension of Ising spin glasses. *Phys. Rev. B*, 64(18):180404, 2001.

[76] Creighton K. Thomas, David A. Huse, and Alan A. Middleton. Zero- and Low-Temperature Behavior of the Two-Dimensional $\pm J$ Ising Spin Glass. *Phys. Rev. Lett.*, 107:047203, 2011.

[77] Francesco Parisen Toldin, Andrea Pelissetto, and Ettore Vicari. Finite-size scaling in two-dimensional Ising spin-glass models. *Phys. Rev. E*, 84(5):051116, 2011.

[78] Thomas Jörg and Florent Krzakala. The nature of the different zero-temperature phases in discrete two-dimensional spin glasses: entropy, universality, chaos and cascades in the renormalization group flow. *JSTAT*, 2012(01):L01001, 2012.

[79] N. Jinuntuya and J. Poulter. Elementary excitations and the phase transition in the bimodal Ising spin glass model. *JSTAT*, 2012(01):P01010, 2012.

[80] L. A. Fernández, E. Marinari, V. Martín-Mayor, G. Parisi, and J. J. Ruiz-Lorenzo. Universal critical behavior of the two-dimensional Ising spin glass. *Phys. Rev. B*, 94:024402, 2016.

[81] F. Barahona. On the computational complexity of Ising spin glass models. *Journal of Physics A: Mathematical and General*, 15(10):3241–3253, 1982.

[82] I. Bieche, R. Maynard, R. Rammal, and J. P. Uhry. On the ground-states of the frustration model of a spin-glass by a matching method of graph-theory. *J. Phys. A*, 13:2553, 1980.

[83] J. A. Blackman and J. Poulter. Gauge-invariant method for the $\pm J$ spin-glass model. *Phys. Rev. B*, 44:4374–4386, 1991.

[84] L. Saul and M. Kardar. Exact integer algorithm for the two-dimensional $\pm J$ Ising spin glass. *Phys. Rev. E*, 48(5), 1993.

[85] A. Galluccio, M. Loebl, and J. Vondrák. New Algorithm for the Ising Problem: Partition Function for Finite Lattice Graphs. *Phys. Rev. Lett.*, 84(26):5924, 2000.

[86] C. K. Thomas and A. A. Middleton. Exact algorithm for sampling the two-dimensional Ising spin glass. *Phys. Rev. E*, 80:046708, 2009.

[87] J. G. Propp and D. B. Wilson. Exact Sampling with Coupled Markov Chains and Applications to Statistical Mechanics. *Rand. Struct. Alg.*, 9:223, 1996.

[88] David B. Wilson. Determinant Algorithms for Random Planar Structures. In *Proceedings of the Eighth Annual ACM-SIAM Symposium on Discrete Algorithms (SODA)*, pages 258–267, 1997.

[89] C. Chanal and W. Krauth. Renormalization group approach to exact sampling. *Phys. Rev. Lett.*, 100:060601, 2008.

[90] C. Amoruso, A. K. Hartmann, M. B. Hastings, and M. A. Moore. Conformal Invariance and Stochastic Loewner Evolution Processes in Two-Dimensional Ising Spin Glasses. *Phys. Rev. Lett.*, 97:267202, 2006.

[91] D. Bernard, P. Le Doussal, and A. A. Middleton. Possible description of domain walls in two-dimensional spin glasses by stochastic Loewner evolutions. *Phys. Rev. B*, 76(2):020403, 2007.

[92] Hamid Khoshbakht, Jacob D. Stevenson, and Martin Weigel. The effect of boundary conditions on Schramm-Loewner evolution in the 2D Ising spin glass at zero temperature. in preparation.

[93] R. Lyons and O. Schramm. Stationary Measures for Random Walks in a Random Environment with Random Scenery. *New York Journal of Mathematics*, 5:107–113, 1999.

[94] S. Smirnov and W. Werner. Critical exponents for two-dimensional percolation. *Mathematical Research Letters*, 8(6):729–744, 2001.

[95] Malte Henkel and Dragi Karevski. A short introduction to conformal invariance. 853:1–49, 2012.

[96] J. Cardy. SLE for theoretical physicists. *Annals of Physics*, 318(1):81–118, 2005.

[97] J. Cardy. Lectures on Stochastic Loewner Evolution and Other Growth Processes in Two Dimensions. *Rudolf Peierls Centre for Theoretical Physics*, (April):1–28, 2006.

[98] Wouter Kager and Bernard Nienhuis. A Guide to Stochastic Löwner Evolution and Its Applications. *Journal of Statistical Physics*, 115(5):1149–1229, 2004.

[99] R. Friedrich and J. Kalkkinen. On conformal field theory and stochastic Loewner evolution. *Nuclear Physics B*, 687(3):279–302, 2004.

[100] Hans C. Fogedby. *Stochastic Loewner Evolution: Linking Universality, Criticality and Conformal Invariance in Complex Systems*, pages 8708–8730. Springer New York, New York, NY, 2009.

[101] M. Bauer and D. Bernard. 2D growth processes: SLE and Loewner chains. *Physics Reports*, 432(3):115 – 221, 2006.

[102] M. Bauer and Denis B. Conformal Field Theories of Stochastic Loewner Evolutions. *Communications in Mathematical Physics*, 239(3):493–521, 2003.

[103] Steffen Rohde and Oded Schramm. *Basic properties of SLE*, pages 989–1030. Springer New York, New York, NY, 2011.

[104] O. Schramm. A Percolation Formula. *Elect. Comm. in Probab.*, 6:115–120, 2001.

[105] P. M. Chaikin and T. C. Lubensky. *Principles of Condensed Matter Physics*. Cambridge University Press, 1995.

[106] O. Schramm. Scaling limits of loop-erased random walks and uniform spanning trees. *Israel Journal of Mathematics*, 118:221–228, 2000.

[107] F. G. Lawler, O. Schramm, and W. Werner. Conformal restriction: the chordal case. *Journal of the American Mathematical Society*, 16(4):917–955, 2003.

[108] F. G. Lawler, O. Schramm, and W. Werner. Conformal invariance of planar loop-erased random walks and uniform spanning trees. *The Annals of Probability*, 32(1):939–995, 2004.

[109] *Spin Glasses and Random Fields*, edited by A. P. Young (World Scientific, Singapore, 1998).

[110] P. W. Anderson and C. M. Pond. Anomalous Dimensionalities in the Spin-Glass Problem. *Physical Review Letters*, 40:903–906, 1978.

[111] A. A. Middleton. Improved extremal optimization for the Ising spin glass. *Physical Review E*, 69:055701, 2004.

[112] *New Optimization Algorithms in Physics*, edited by A. K. Hartmann and H. Rieger, ISBN: 978-3-527-40406-3 (Wiley-VCH, Weinheim, 2004).

[113] Creighton K. Thomas and A. Alan Middleton. Matching Kasteleyn Cities for Spin Glass Ground States. *Physical Review B*, 76:220406, 2007.

[114] P. W. Kasteleyn. Dimer Statistics and Phase Transitions. *Journal of Mathematical Physics*, 4:287, 1963.

[115] Vladimir Kolmogorov. Blossom V : a new implementation of a minimum cost perfect matching algorithm. *Mathematical Programming Computation*, 1:43–67, 2009.

[116] Spin-glass server. http://www.informatik.uni-koeln.de/spinglass/.

[117] M. Weigel. Genetic embedded matching approach to ground states in continuous-spin systems. *Phys. Rev. E*, 76:066706, 2007.

[118] F. Liers, M. Jünger, G. Reinelt, and G. Rinaldi. *Computing Exact Ground States of Hard Ising Spin Glass Problems by Branch-and-cut*. Wiley VCH, Weinheim, 2004.

[119] J. P. Bouchaud, F. Krzakala, and O. C. Martin. Energy exponents and corrections to scaling in Ising spin glasses. *Phys. Rev. B*, 68(22):224404, 2003.

[120] I. A. Campbell, A. K. Hartmann, and H. G. Katzgraber. Energy size effects of two-dimensional Ising spin glasses. *Phys. Rev. B*, 70:054429, 2004.

[121] M. Weigel and M. J. P. Gingras. Zero-temperature phase of the XY spin glass in two dimensions: Genetic embedded matching heuristic. *Phys. Rev. B*, 77:104437, 2008.

[122] V. Privman. *Finite-Size Scaling Theory*. World Scientific, Singapore, 1990.

[123] Jan Wehr and Michael Aizenman. Fluctuations of extensive functions of quenched random couplings. *J. Stat. Phys.*, 60(3):287–306, 1990.

[124] A. C. Carter, A. J. Bray, and M. A. Moore. Aspect-ratio scaling and the stiffness exponent θ for Ising spin glasses. *Phys. Rev. Lett.*, 88:077201, 2002.

[125] J. R. Banavar and M. Cieplak. Nature of ordering in spin glasses. *Phys. Rev. Lett.*, 48:832, 1982.

[126] J. M. Kosterlitz and N. Akino. Numerical study of spin and chiral order in a two-dimensional XY spin glass. *Phys. Rev. Lett.*, 82:4094, 1999.

[127] M. Weigel and M. J. P. Gingras. Ground states and defect energies of the two-dimensional XY spin glass from a Quasi-Exact algorithm. *Phys. Rev. Lett.*, 96:097206, 2006.

[128] G. K. Savvidy and N. G. Ter-Arutyunyan-Savvidy. On the Monte Carlo Simulation of Physical Systems. *J. Comp. Phys.*, 97:566–572, 1991.

[129] K. G. Savvidy. The MIXMAX random number generator. *Comput. Phys. Commun.*, 196:161–165, 2015.

[130] Pierre L'Ecuyer and Richard Simard. TestU01: A C library for empirical testing of random number generators. *ACM Trans. Math. Softw.*, 33(4):22, 2007.

[131] Makoto Matsumoto and Takuji Nishimura. Mersenne twister: A 623-dimensionally equidistributed uniform pseudo-random number generator. *ACM Trans. Model. Comput. Simul.*, 8(1):3–30, 1998.

[132] A. Peter Young. *Everything you wanted to know about Data Analysis and Fitting but were afraid to ask*. SpringerBriefs in Physics. Springer, Berlin, 2015.

[133] W. L. McMillan. Domain-wall renormalization-group study of the two-dimensional random Ising model. *Phys. Rev. B*, 29:4026, 1984.

[134] A. J. Bray and M. A. Moore. Lower critical dimension of Ising spin glasses: a numerical study. *J. Phys. C*, 17:L463, 1984.

[135] A. J. Bray and M. A. Moore. Chaotic nature of the spin-glass phase. *Phys. Rev. Lett.*, 58(1):57–60, 1987.

[136] Heiko Rieger, Ludger Santen, Ulrich Blasum, Martin Diehl, Michael Jünger, and Giovanni Rinaldi. The critical exponents of the two-dimensional Ising spin glass revisited: exact ground-state calculations and Monte Carlo simulations. *J. Phys. A*, 29:3939, 1996.

[137] Alan A. Middleton. Energetics and geometry of excitations in random systems. *Phys. Rev. B*, 63:060202, 2001.

[138] M. Weigel and D. A. Johnston. Frustration effects in antiferromagnets on planar random graphs. *Phys. Rev. B*, 76:054408, 2007.

[139] A. K. Hartmann, A. J. Bray, A. C. Carter, M. A. Moore, and A. P. Young. Stiffness exponent of two-dimensional Ising spin glasses for nonperiodic boundary conditions using aspect-ratio scaling. *Phys. Rev. B*, 66:224401, 2002.

[140] M. Henkel. *Conformal Invariance and Critical Phenomena*. Springer, Berlin/Heidelberg/New York, 1999.

[141] S. Brandt. *Data Analysis: Statistical and Computational Methods for Scientists and Engineers*. Springer, Berlin, 3rd edition, 1998.

[142] M. Weigel and W. Janke. Error estimation and reduction with cross correlations. *Phys. Rev. E*, 81:066701, 2010.

[143] Victor Dotsenko, Yurij Holovatch, Maxym Dudka, and Martin Weigel. Self-averaging in the random two-dimensional Ising ferromagnet. *Phys. Rev. E*, 95:032118, 2017.

[144] T. Aspelmeier and M. A. Moore. Free Energy Fluctuations in Ising Spin Glasses. *Phys. Rev. Lett.*, 90:177201, 2003.

[145] Mohammed-Sadegh Vaezi, Zohar Nussinov, Gerardo Ortiz, and Martin Weigel. The binomial spin glass. Preprint arXiv:1712.08602.

[146] M. Weigel and W. Janke. Cross correlations in scaling analyses of phase transitions. *Phys. Rev. Lett.*, 102:100601, 2009.

[147] D. J. Perez-Morelo, A. J. Ramirez-Pastor, and F. Romá. Ground-state energy and entropy of the two-dimensional Edwards–Anderson spin-glass model with different bond distributions. *Physica A*, 391:937–947, 2012.

[148] J. E. Avron, G. Roepstorff, and L. S. Schulman. Ground state degeneracy and ferromagnetism in a spin glass. *J. Stat. Phys.*, 26(1):25–36, 1981.

[149] M. Cieplak and J. R. Banavar. Scaling of stiffness in Ising spin glasses. *J. Phys. A*, 23(19):4385, 1990.

[150] S. Risau-Gusman and F. Romá. Fractal dimension of domain walls in the Edwards-Anderson spin glass model. *Phys. Rev. B*, 77:134435, 2008.

[151] Hamid Khoshbakht and Martin Weigel. Uniform sampling of spin-glass ground states. in preparation.

[152] J. Hoshen and R. Kopelman. Percolation and cluster distribution. I. Cluster multiple labeling technique and critical concentration algorithm. *Phys. Rev. B*, 14:3438–3445, 1976.

[153] D. E. Knuth. *The Art Of Computer Programming*, Vol 1. Third Edition., Boston: Addison-Wesley, (1997).

[154] T. H. Cormen, C. E. Leiserson, R. L. Rivest, and C. Stein. *Introduction to Algorithms*, Third Edition, MIT Press and McGraw-Hill, (2009). ISBN 0-262-03293-7.

[155] Nicholas Metropolis, Arianna W. Rosenbluth, Marshall N. Rosenbluth, Augusta H. Teller, and Edward Teller. Equation of state calculations by fast computing machines. *The Journal of Chemical Physics*, 21(6):1087–1092, 1953.

[156] Koji Hukushima and Koji Nemoto. Exchange Monte Carlo Method and Application to Spin Glass Simulations. *Journal of the Physical Society of Japan*, 65(6):1604–1608, 1996.

[157] J. Houdayer. A cluster Monte Carlo algorithm for 2-dimensional spin glasses. *Eur. Phys. J. B*, 22:479, 2001.

[158] Ronald Fisch. Aspect-ratio scaling of domain wall entropy for the 2d $\pm j$ Ising spin glass. *J. Stat. Phys.*, 130:561–569, 2008.

[159] C. Amoruso, E. Marinari, O. C. Martin, and A. Pagnani. Scalings of Domain Wall Energies in Two Dimensional Ising Spin Glasses. *Phys. Rev. Lett.*, 91(8):087201, 2003.

[160] J. D. Stevenson and M. Weigel. Domain walls and Schramm-Loewner evolution in the random-field Ising model. *EPL (Europhysics Letters)*, 95(4):40001, 2011.

[161] D. Chelkak, H. Duminil-Copin, C. Hongler, A. Kemppainen and S. Smirnov. Convergence of Ising interfaces to Schramms SLE curves. *Comptes Rendus Mathematique*, 352(2):157 – 161, 2014.

[162] T. Kennedy. A Fast Algorithm for Simulating the Chordal Schramm–Loewner Evolution. *Journal of Statistical Physics*, 128(5):1125–1137, 2007.

[163] T. Kennedy. Computing the Loewner Driving Process of Random Curves in the Half Plane. *Journal of Statistical Physics*, 131(5):803–819, 2008.

[164] R. L. Wasserstein and N. A. Lazar. The asa's statement on p-values: Context, process, and purpose. *The American Statistician*, 70(2):129–133, 2016.